UC San Diego

UC San Diego Electronic Theses and Dissertations

Title

Leveraging Prior Knowledge for Performance Improvement in Control, Estimation, and Identification

Permalink

https://escholarship.org/uc/item/1b43j359

Author

Moroto, Robert Hiroshi

Publication Date

2017

Peer reviewed|Thesis/dissertation

UNIVERSITY OF CALIFORNIA, SAN DIEGO

Leveraging Prior Knowledge for Performance Improvement in Control, Estimation, and Identification

A dissertation submitted in partial satisfaction of the
requirements for the degree
Doctor of Philosophy

in

Engineering Sciences (Mechanical Engineering)

by

Robert Hiroshi Moroto

Committee in charge:

Professor Robert R. Bitmead, Chair
Professor Jorge Cortés
Professor Maurício de Oliveira
Professor Melvin Leok
Professor Jiawang Nie

2017

The dissertation of Robert Hiroshi Moroto is approved, and it is acceptable in quality and form for publication on microfilm:

Chair

University of California, San Diego

2017

DEDICATION

To Big G, Joy, my family, Kemp, and the fluffy ones.

EPIGRAPH

Use what you know. If you know something useful, then why not use it?

—Professor Robert R. Bitmead

TABLE OF CONTENTS

LIST OF FIGURES

LIST OF TABLES

ACKNOWLEDGEMENTS

I could not have completed this degree without the generously supportive mentoring, guidance, and support of my advisor Professor Robert Bitmead and my friend and colleague Chad Holcomb. I am profoundly grateful for the wisdom, life lessons, and advice they have consistently and frequently offered me over the years, and for the many opportunities have provided for me with the help of their tireless advocacy on my behalf. I am forever grateful.

I extend a profound thank you to Solar Turbines for their generous financial support for my research, for the invaluable summer internship opportunities, and for allowing me to be fortunate enough to begin my career prior to finishing school. I am also extremely grateful to my colleagues at Solar for their support and accommodation through out my time in school, especially Saliha LaCoursiere, Roy Dickenson, Vivek Khanna, G.B. Singh, John Bowen, Robert Mendoza, Jason Ritchie, and Cody Allen.

I am deeply indebted to my family for their patience, guidance, wisdom, and support over these many years. In particular, I thank my grandmother for the countless ways she diligently supported my education throughout my life and without whom I would not be writing this dissertation; to my parents and sister for always being behind me 100% and for all the life lessons that shaped who I am; to Joy for her steadfast commitment, sage advice, constant inspiration, amusing wit, and fantastic cooking; and to Kemp for his unwavering friendship, moral support, fascinating mind, and unique perspective on life.

Thank you to my fellow graduate students for your friendship, guidance, insightful conversations, and commiseration, especially Eduardo Ramirez, Daniele Cavaglieri, Andres Cortes, David Mateos, Ashish Cherukuri, Ben Huang, Minh Ha, Amit Pandey, Martin Sehr, and all the rest.

I would also like to thank the other members of my committee, Maurcio de Oliveira, Jorge Corts, Jiawang Nie, and Melvin Leok for their participation and guidance.

Publications: The following published works are referenced in the dissertation:

Chapter 2: Robert H. Moroto, Robert R. Bitmead, and Bram Sleegers, "The Information Structure of Feedforward/Preview Control Using Forecast Data," *The 19th World Congress of the International Federation of Automatic Control*, Aug. 2014.

Chapter 3: Robert H. Moroto, Robert R. Bitmead, and Chad M. Holcomb, "Improving Disturbance Compensation in Gas Turbines by Incorporating Event-Triggered Logic Signals From Switchgear," to appear in *Proceedings of the ASME Turbo Expo 2017. Turbine Technical Conference & Exposition*, Charlotte, NC, USA, 2017.

2011	B.S. in Mechanical Engineering, University of California San Diego
2013	M.S. in Engineering Sciences (Mechanical Engineering), University of California San Diego
2017	Ph.D. in Engineering Sciences (Mechanical Engineering), University of California, San Diego

PUBLICATIONS

Robert H. Moroto, Robert R. Bitmead, and Bram Sleegers, "The Information Structure of Feedforward/Preview Control Using Forecast Data," *The 19th World Congress of the International Federation of Automatic Control*, Aug. 2014.

Robert H. Moroto, Robert R. Bitmead, and Chad M. Holcomb, "Improving Disturbance Compensation in Gas Turbines by Incorporating Event-Triggered Logic Signals From Switchgear," to appear in *Proceedings of the ASME Turbo Expo 2017. Turbine Technical Conference & Exposition*, Charlotte, NC, USA, 2017.

ABSTRACT OF THE DISSERTATION

Leveraging Prior Knowledge for Performance Improvement in Control, Estimation, and Identification

by

Robert Hiroshi Moroto

Doctor of Philosophy in Engineering Sciences (Mechanical Engineering)

University of California San Diego, 2017

Professor Robert R. Bitmead, Chair

In many practical engineering applications, a significant portion of the available information is excluded from the design process due to a lack of obvious mechanisms for its incorporation. In this dissertation, several methods are presented for leveraging such underutilized prior knowledge in application-oriented settings. Three cases, motivated by real-world examples, are considered, addressing controller, estimator, and identification design respectively. In each case, a methodology is presented capturing the key features of the prior knowledge in a characterization which can be readily incorporated into standard solution.

Firstly, a flexible modeling framework is presented for characterizing time-advanced forecast data associated with an exogenous disturbance. The model is incorporated into a disturbance-attenuating feedforward controller which can be synthesized with standard $\mathcal{H}_2$ or $\mathcal{H}_\infty$ methods. The closed-loop performance calculation provides a comparative metric to juxtapose multiple designs and address economic questions, such as sensor placement. A practical example is provided for a wind turbine and lidar sensor with

tunable focus range.

Secondly, a modeling framework is presented for characterizing logic-valued measurements that provide timely indication of an associated disturbance event. An estimator is constructed using the fast logic-valued measurement, and known disturbance statistics, to rapidly adjust the disturbance estimate, resulting in improved performance. The framework is applied to a gas turbine (GT) system with transient load disturbance associated with a fast electrical breaker switching measurement. The method is generalized to incorporate multiple disturbance load and breaker pairs.

Finally, a high-fidelity GT (HFGT) model is used to construct a linear GT engine model for control design. The HFGT model generates closed-loop transient simulation data for system identification and the structure of its internal subsystems is leveraged to reduce the complexity of the identification process by excluding unnecessary subsystems. The partition of subsystems is enabled by access to signals in the high-fidelity model which are otherwise unavailable during physical engine testing. The resulting linear engine model can be modularly reconfigured with different fuel subsystem and rotor subsystem models. The linear GT model is validated in closed-loop transient simulations.

Chapter 1

Introduction

Prior knowledge is any knowledge of a system of interest that contains valuable information which, if exploited, would potentially improve the performance of the resulting design for the problem at hand.

It is often the case that valuable information is available during design, but is ignored due to a failure to determine an obvious method for incorporating it into the problem. The nature of the ignored prior knowledge, and its relationship to the problem at hand, can vary significantly between applications. However, by characterizing the prior knowledge with a representation that can be combined with the model of the system of interest, the resulting augmented model can be used in the application of standard techniques of control, estimation, and identification.

In many practical engineering applications, such as industrial settings, the core technology of the system of interest does not significantly change over time, and a sufficient controller or estimator is implemented for an extended duration based on the system knowledge which was available at the time of initial deployment. However, the ubiquitous growth of sensor instrumentation and simulation capabilities has vastly increased the amount of prior knowledge available.

The diversity of prior knowledge has also rapidly increased and can take many forms, such as new sensor technology which can measure previously inaccessible signals; inexpensive sensors which can be massively and flexibly deployed; high-fidelity simulations which can generate data in a rapid and inexpensive manner; advances engineering knowledge and first principles models specific to the domain of application; and a host

of other sources of knowledge. The expanding pool of available prior knowledge often contains actionable information that can potentially improve the performance, and thus the economic benefit, of closed-loop systems. However, due to the rapid advancement and adoption of the technologies which enabled the expansion, available prior knowledge often remains underutilized.

Applied research in control, estimation, and identification has traditionally focused on adapting the existing theoretical design techniques to specific engineering examples, which can result in ad hoc solutions for incorporating prior knowledge. The diversity of specific prior knowledge and the general nature of the techniques of control, estimation and system identification, leaves a void in the middle ground of the applicability of design methods and a demand exists for methods which bridge the gap of generality. Thus, there is a need for to develop approaches for incorporating prior knowledge into control, estimation, and system identification problems which are specific enough to leverage prior knowledge of a certain type, but general enough to be applied to multiple scenarios.

1.1 Contributions

This work is a first step in the development of methods for improving system performance via the systematic inclusion of available prior knowledge into control design, estimator design, and system identification design processes. Each chapter addresses a different type of available prior information.

Chapter 2 addresses prior knowledge in the form of forecast data, i.e. time-advanced disturbance information. A methodology is proposed for constructing a model which captures the essential features of forecast data. The model can be flexibly adapted to a variety of forecast data types and its user-specified parameters maintain intuitive informational significance by design. The forecast model is formulated for incorporation into a feedforward control design problem, for disturbance rejection, in a straightforward manner. Practical economic questions can be answered by using the calculated closed-loop performance (which is calculated offline, i.e. prior to implementation) as a comparative metric among different design configurations. For example, the potential

benefits derived from different upstream forecast sensor placement locations can be considered. Juxtaposition of design with sensors of different quality can also be compared and the potential closed-loop performance benefits can be weighed against the added cost of the higher quality sensor. A wind turbine and lidar sensor system are used as an illustrative example.

Chapter 3 addresses prior information in the form of an event-triggered logic signal acting as a rapid indicator associated with a step change in the exogenous disturbance signal. Statistical information about the step change in the disturbance signal is known as well. However, timely direct measurements of the disturbance signal are not available. The problem is applied to a gas turbine used in power generation in a microgrid. The switching signal from an instrumented electrical breaker is used to indicate the occurrence of a step load disturbance which can not be measured in a timely manner. A modeling methodology is proposed for characterizing the described setup and a state estimator is constructed which can accommodate the logic signal and statistical disturbance data to rapidly respond to abrupt changes in the disturbance signal, providing more up to date load estimates than if the prior information was not considered. The estimator is also generalized to the case of multiple logic-valued signals and associated disturbances. A numerical example demonstrates the benefits of the approach.

Chapter 4 addresses prior information in the form of a high-fidelity gas turbine model which generates data for system identification and whose internal subsystem structure can be exploited in the construction of a linear time-invariant gas turbine model for control design. The constructed model is highly modular and the identified subsystem can be interchangeably combined with different fuel subsystem and rotor subsystem models for control design. The flexibility of the model allows controller to be designed across the many product configurations that are inherent to industrial gas turbines due to diverse customer needs.

The proposed methods, although distinct, are unified in the conceptual strategy of recognizing key features of the prior knowledge and characterizing those features in such a way that they may be easily incorporated into an augmented model which is compatible with standard techniques of control design, estimator design, and system identification respectively.

Chapter 2

Feedforward With Forecast Data

2.1   Introduction

Disturbance rejection control can be augmented with measurements or predictions of future disturbance values yet to arrive at the plant. In some cases, such as in chemical processing, these upstream measurements can be exact. However, frequently forecast data and/or predictions are used and these display the property that distant future values are less reliable predictions of the disturbance than are more short-term predictions. For example, in building energy management, weather predictions can provide data for use by a feedforward controller to improve closed-loop performance, but predictions about weather far ahead in the future tend to be less accurate than predictions about impending weather.

The central contribution of this paper is to provide a systematic approach to the inclusion of this property of forecast data, but reducing to earlier approaches with perfect forecasts, and the straightforward evaluation of subsequent control performance. This permits the methodical assessment of the performance benefits of improved forecast data quality or of sensor placement and design.

2.1.1   Feedforward control

Feedforward (or preview) control is a subject of substantial practical interest because it brings improved performance to feedback control. It has two core variants: using

time-advanced reference signal information to improve tracking performance, and using forecast disturbance signals to aid in disturbance rejection. The formulations are strongly related, see [2]. Our development will concentrate on feedforward of forecast data for disturbance rejection alone.

A technically thorough and historically detailed survey of preview control was very recently published by [3]. Feedforward/preview control has been widely applied in areas such as vehicle suspension, as seen in [4], [5], [6], [7], and [8] and for the control of wind turbines with wind velocity preview information, as seen in [9], [10], [11], and [12], for example. The techniques developed in this paper are general without a specific process in mind, although motivated by the wind turbine lidar problem. The formative recent works which guide our analysis include [13], [2], [14], [15], and [16]. Our contribution is to accommodate the nature of forecast data into the feedforward formulation in a utile fashion. It is well understood that the information bearing quality of forecasts usually diminishes with horizon, [17].

The standard approach to feedforward design is to precede the disturbance signal in the system model by a tapped-delay-line of length equal to the preview horizon fed by the future disturbance values. Access to the input or to the state of this tapped-delay-line then provides the feedforward information. This is illustrated for horizon N in Figure 2.1.

The spectral or correlation properties of the disturbance are captured by the disturbance-generating model driven by white noise $w_{d,k}$ to yield advanced disturbance measurement, d_{k+N}, which then enters the delay line. The feedforward controller uses measurements from both the N-step-ahead disturbance forecast $y_{f,k} = d_{k+N}$ and the plant output y_k to form a control signal u_k intended to mitigate the effect of the disturbance on y_k. This feedforward control design paradigm using exact preview measurements of the disturbance is posed and explored for the $\mathscr{H}_2$ control problem in [13] and for the $\mathscr{H}_\infty$ control problem in [18]. The potential performance improvement for preview control in the $\mathscr{H}_\infty$ case was explored in [19]. The entire state of the delay-line, $\{d_k, d_{k+1}, \ldots, d_{k+N-1}\}$, is simply constructed from d_{N+k} and appears in the controller as part of the state feedback.

For the reference tracking case, [20] appears to have been the first to introduce the
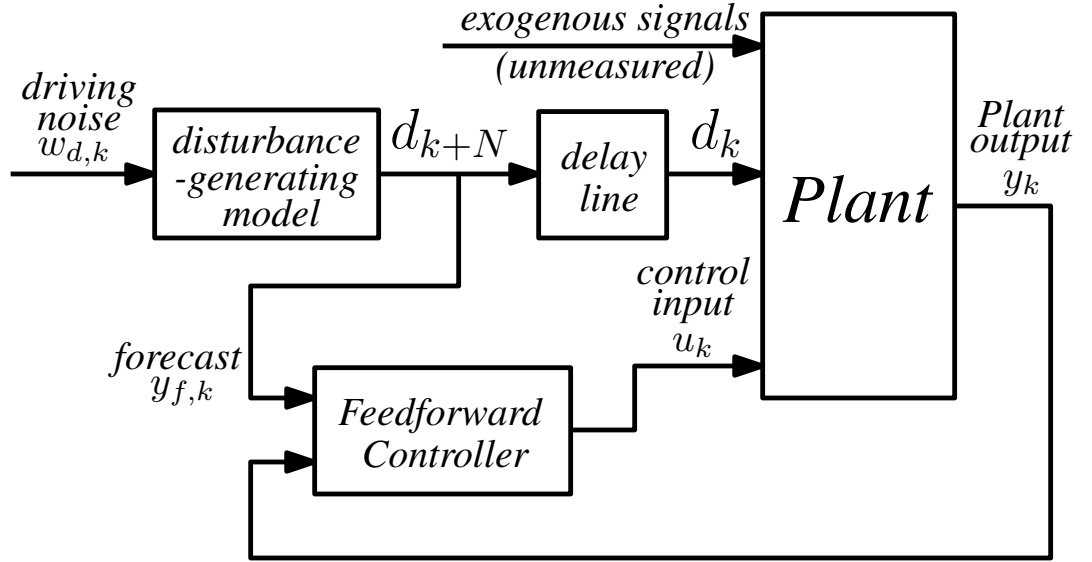
Figure 2.1: Feedforward system model with exact previewed disturbance data. Forecast $y_{f,k}$ captures future values of disturbance d_k via the measurement $y_{f,k} = d_{k+N}$.

delay-line model, although in [21] it is presented as inclusive of white measurement noise adding to the forecast data. The forecast data signal is no longer just the exact entering disturbance, d_{k+N}, but a noisy variant of the entire delay-line state. This is depicted in Figure 2.2. In this approach, the feedforward data is an inexact representation of the disturbance because of the presence of the noise signal $v_{f,k}$. Related methods are applied by [6], who take a noisy d_{N+k} as input rather than the entire delay-line state. They then apply these techniques to a vehicle suspension system. The full delay-line state with additive noise was also explored by [22] as an approach to capturing the degradation of forecast data information content regarding the future disturbance.

The individual elements of the measurement noise are assumed to be zero-mean, independent, and white, each with a respective covariance, $V_f^{(i)}$. Selection of these positive definite measurement noise covariances ,$V_f^{(1)} \leq \cdots \leq V_f^{(N)}$, introduces a mechanism for accommodating the diminishing data quality seen with increasingly time-advanced forecast data. The optimal disturbance rejection performance can still be calculated via the closed-loop cost, which, much like exact preview control, is monotonically non-increasing and tends to a limiting value as N grows to infinity. However, compared to the exact case, inexact previewed disturbance information will typically yield higher
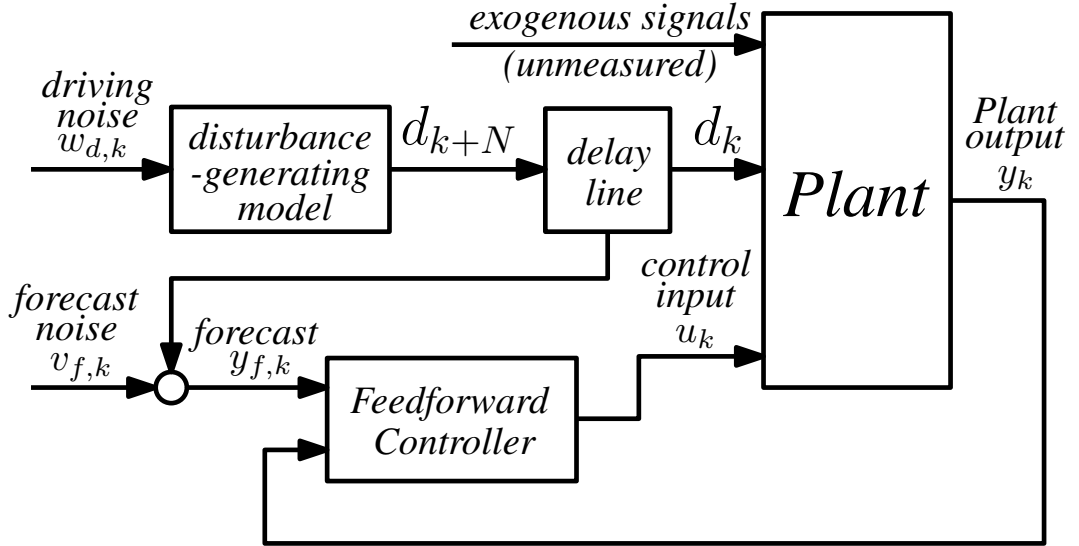
Figure 2.2: Feedforward control problem with inexact previewed disturbance data. Forecast $y_{f,k}$ measures disturbance data $\{d_k, d_{k+1}, \ldots, d_{k+N-1}\}$ affected by additive measurement noise $v_{f,k}$.

cost values for a given forecast horizon N, including the limiting cost value as the forecast horizon extends to infinity.

In this paper, the delay-line of feedforward control is replaced by a forecast signal model, shown in Figure 2.3, driven by a sequence, $\left\{\mathfrak{d}_k^{(1)}, \ldots, \mathfrak{d}_k^{(N)}\right\}$, of N mutually independent signals of spectra identical to the actual disturbance d_k. The parameters $\left\{\alpha^{(1)}, \ldots, \alpha^{(N-1)}\right\}$ determine the loss of coherence between feedforward measurements $\{d_k^{(1)}, \ldots, d_k^{(N)}\}$ and the eventual disturbance d_k. The construction of the forecast signal model ensures that the forecast data elements, $d_k^{(i)}$, are each correlated with the actual disturbance d, but are of successively diminishing correlation with increasing prediction time (i).

The framework we develop subsumes the exact feedforward signal approach with the selection of $\alpha^{(j)} = 1$, for all j, but is capable of capturing a wider range of data quality factors. The parametrization of this forecast signal model is simple and meshes with the standard linear optimal control design tools such as `h2syn` and `hinfsyn` from MATLAB. With a complete set of forecast measurements along the horizon, our solution displays the same qualitative closed-loop cost behavior as seen in the exact case as N tends to infinity, but the performance is reduced because of the data imperfection.
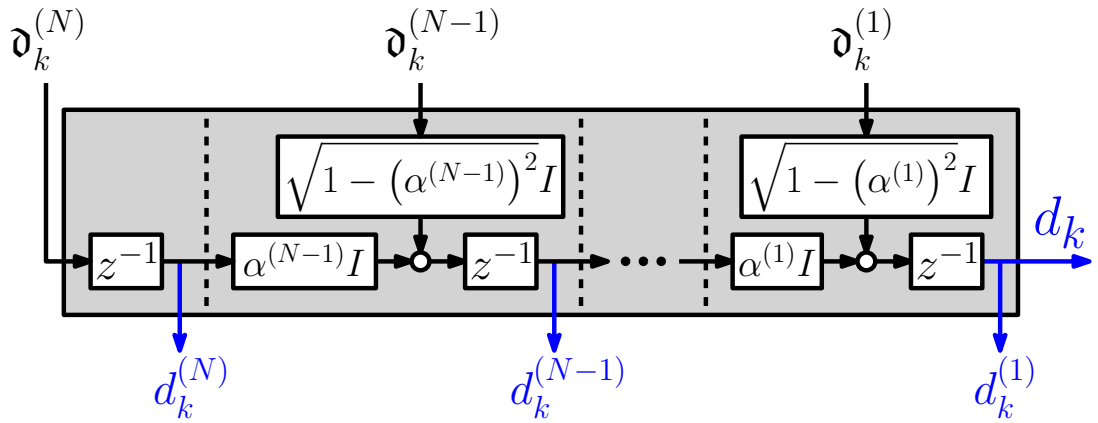
Figure 2.3: Forecast signal model, where $0 \le \alpha^{(j)} \le 1$ for $j = 1, \ldots, N-1$. Disturbance d_k affects the system to be controlled.

Further, our analysis permits the consideration of sensor placement, which is not well-posed in the exact context.

2.1.2 Organization

The remainder of this work is organized as follows. In Section 2.2, we motivate our control design method with an illustrative example of a lidar-based wind velocity-field measurement system attached to a wind turbine, and we pose a set of design questions, that are addressed later in the paper, highlighting the utility of our approach. In Section 2.3, we introduce the framework for modeling forecast data that is the primary focus of this paper which we use to pose a corresponding control problem based on a generalized plant structure. Section 2.5 is devoted to answering the design questions posed in Section 2.2 through the use of a simple numerical example. We discuss some potential applications and areas of future exploration in Section 2.6.

2.2 Motivating example and design questions

The hallmark property of forecast data, exemplified nowhere better than in meteorological forecasts, is that reliability diminishes with forecast horizon. From a statistical perspective, the future and present signals might possess identical spectra but the decoherence of the eventual signal and its upstream or propagated measurement reduces

the information value associated with forecast data. For illustrative purposes, we consider a lidar forecast signal in wind turbine mechanical load management.

Figure 2.4 depicts a wind turbine equipped with a lidar-based wind velocity-field measurement, which can be focused at a number of distances ahead of the turbine to provide wind gust information for feedforward control of blade and tower loading. The disturbance arriving at the turbine is d_k, as in the formulation above, and the wind velocity forecasts, $d_k^{(i)}$, are associated both with lead time and physical position ahead of the turbine. Turbulence and flow variation lead to the transformation of the velocity-field before its eventual arrival at the turbine. This, in turn, leads to the de-coherence of forecast data as developed in the signal model above.
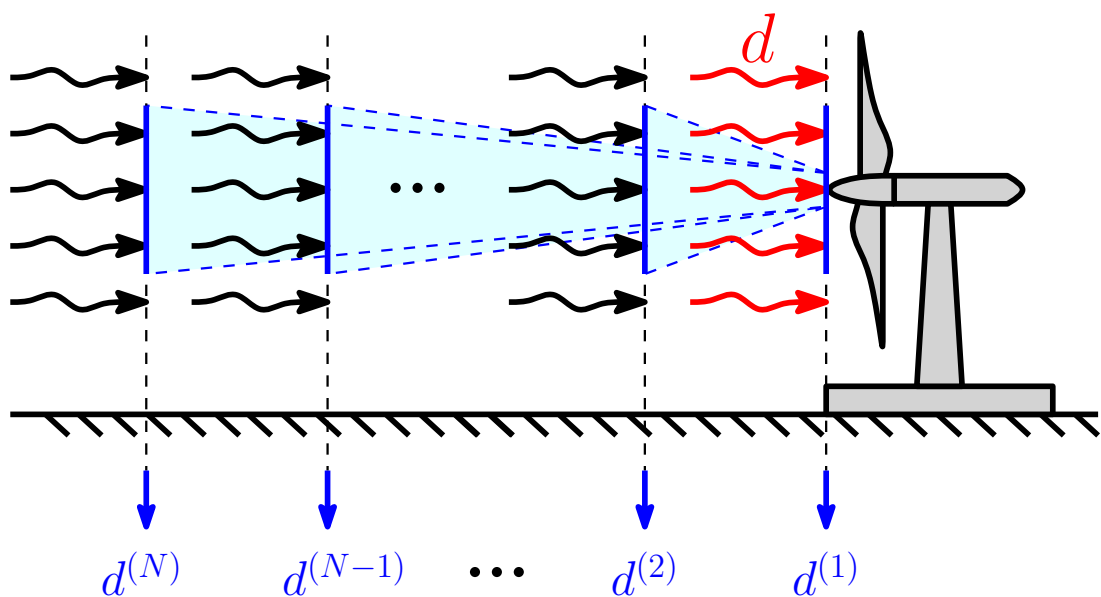
Figure 2.4: Wind turbine schematic with impinging blade load signal, d, and lidar-based upstream feedforward/forecast data, $\{d^{(i)} : i = 1, \dots, N\}$, at a number of positions.

2.2.1 Design questions

To fix ideas, we pose the following two questions.

(Q1) Given forecast measurements, $\{d^{(i)} : i = 1, \dots, N\}$, along the whole horizon, how is the coherence of the forecast data reflected in the achieved closed-loop performance?

(Q2) Given a fixed number of feedforward sensors to place, we ask the following:

    (a) At which positions should the sensors be placed to achieve the best closed-loop performance?

    (b) If a feedforward sensor with a higher quality and cost were available, would the corresponding improvement in performance provide sufficient economic benefit to justify purchasing, installing and maintaining that sensor? Further, where should this sensor now be placed?

2.3 Forecast modeling

For clarity, the approach is developed in the $\mathscr{H}_2$ framework with commentary provided in the conclusion, and elsewhere where appropriate, concerning the allied $\mathscr{H}_\infty$ variant. This parallels the approach of [13] for $\mathscr{H}_2$ and [18] for $\mathscr{H}_\infty$.

2.3.1 Plant model

Plant P is described by state-variable realization

$$x_{k+1} = Ax_k + Bu_k + W^{\frac{1}{2}}w_k,$$
$$y_k = Cx_k + d_k + V^{\frac{1}{2}}v_k.$$

Here: x_k is the plant state, u_k is the control signal, y_k is the measured output signal, d_k is an additive output disturbance for which forecast data is available, and signals w_k and v_k are additional white unit variance exogenous signals representing non-fed-forward process and measurement white noise signals, scaled by nonnegative definite matrix $W^{\frac{1}{2}}$ and positive definite matrix $V^{\frac{1}{2}}$.

2.3.2 Disturbance-generating model

Disturbance signal $\{d_k\}$ has known spectrum and is modeled as the output of a stable linear system $G_d(z)$,

$$d_k = G_d(z)w_{d,k},$$

driven by white unit variance noise signal $\{w_{d,k}\}$. This is realized in the state variable system

$$x_{d,k+1} = A_d x_{d,k} + W_d^{\frac{1}{2}} w_{d,k},$$

$$d_k = C_d x_{d,k},$$

where $W_d^{\frac{1}{2}}$ is a nonnegative definite matrix .

2.3.3 Forecast signal model

We now introduce a forecast signal model that captures the feature of forecast data that the correlation decreases between a measured upstream disturbance $d_k^{(i)}$ and its corresponding eventual disturbance d_{k+i-1} as the lead time, i, between the two signals increases. Each forecast signal model has the following identical state realization.

$$x_{d,k+1}^{(i)} = A_d x_{d,k}^{(i)} + W_d^{\frac{1}{2}} w_{d,k}^{(i)}, \tag{2.1}$$

$$d_k^{(i)} = \begin{cases} \beta^{(i)} C_d x_{d,k-1}^{(i)} + \alpha^{(i)} d_{k-1}^{(i+1)}, & \text{if } i = 1, \ldots, N-1, \\ C_d x_{d,k-1}^{(i)}, & \text{if } i = N, \end{cases} \tag{2.2}$$

where, for convenience, we define the parameters

$$\beta^{(j)} = \sqrt{1 - \left(\alpha^{(j)}\right)^2}, \tag{2.3}$$

for $j = 1, \ldots, N-1$. The forecast signal model given in (2.1-2.2) corresponds to the model illustrated in Figure 2.3 expanded to include the disturbance-generating models G_d and depicted in Figure 2.5.

The forecast signal model G_D and forecast measurement signal $y_{f,k}$ have the aggregated state-variable realization.

$$x_{D,k+1} = A_D x_{D,k} + B_D w_{D,k},$$

$$d_k = C_D x_{D,k},$$

$$y_{f,k} = C_f x_{D,k} + V_f^{\frac{1}{2}} v_{f,k},$$
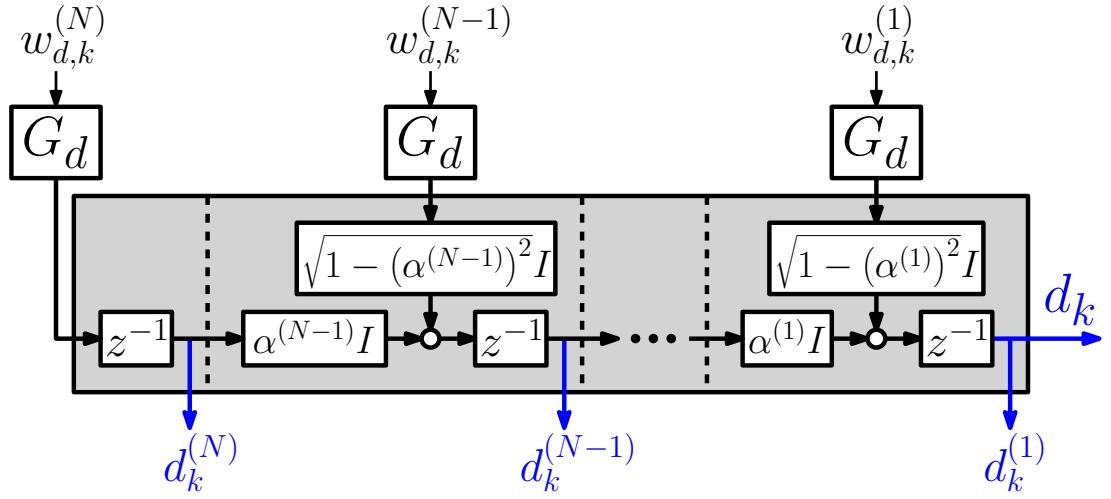
Figure 2.5: Expanded version of forecast signal model seen in Figure 2.3 including disturbance-generating models G_d, where $0 \leq \alpha^{(j)} \leq 1$.

or

$$
y_{f,k} = \begin{bmatrix} d_k^{(1)} \\ \hline d_k^{(2)} \\ \hline \vdots \\ \hline d_k^{(N-1)} \\ \hline d_k^{(N)} \end{bmatrix} + \begin{bmatrix} V_f^{(1)\frac{1}{2}} v_{f,k}^{(1)} \\ \hline V_f^{(2)\frac{1}{2}} v_{f,k}^{(2)} \\ \hline \vdots \\ \hline V_f^{(N-1)\frac{1}{2}} v_{f,k}^{(N-1)} \\ \hline V_f^{(N)\frac{1}{2}} v_{f,k}^{(N)} \end{bmatrix},
$$

with $V_f^{(1)} = V_f^{(2)} = \cdots = V_f^{(N)} > 0$, and where

$$
x_{D,k} = \begin{bmatrix} d_k^{(1)} \\ x_{d,k}^{(1)} \\ \hline d_k^{(2)} \\ x_{d,k}^{(2)} \\ \hline \vdots \\ \hline d_k^{(N-1)} \\ x_{d,k}^{(N-1)} \\ \hline d_k^{(N)} \\ x_{d,k}^{(N)} \end{bmatrix}, \quad w_{D,k} = \begin{bmatrix} w_{d,k}^{(1)} \\ \hline w_{d,k}^{(2)} \\ \hline \vdots \\ \hline w_{d,k}^{(N-1)} \\ \hline w_{d,k}^{(N)} \end{bmatrix},
$$

$$A_D = \left[\begin{array}{cc|cc|c|cc|cc}
0 & \alpha^{(1)}C_d & \beta^{(1)}I & 0 & \cdots & 0 & 0 & 0 & 0 \\
0 & A_d & 0 & 0 & \cdots & 0 & 0 & 0 & 0 \\
\hline
0 & 0 & 0 & \alpha^{(2)}C_d & \cdots & 0 & 0 & 0 & 0 \\
0 & 0 & 0 & A_d & \cdots & 0 & 0 & 0 & 0 \\
\hline
\vdots & \vdots & \vdots & \vdots & \ddots & \vdots & \vdots & \vdots & \vdots \\
\hline
0 & 0 & 0 & 0 & \cdots & 0 & \alpha^{(N-1)}C_d & \beta^{(N-1)}I & 0 \\
0 & 0 & 0 & 0 & \cdots & 0 & A_d & 0 & 0 \\
\hline
0 & 0 & 0 & 0 & \cdots & 0 & 0 & 0 & C_d \\
0 & 0 & 0 & 0 & \cdots & 0 & 0 & 0 & A_d
\end{array}\right],$$

with $\beta^{(j)}$ defined as in (2.3),

$$B_D = \left[\begin{array}{c|c|c|c|c}
0 & 0 & \cdots & 0 & 0 \\
W_d^{\frac{1}{2}} & 0 & \cdots & 0 & 0 \\
\hline
0 & 0 & \cdots & 0 & 0 \\
0 & W_d^{\frac{1}{2}} & \cdots & 0 & 0 \\
\hline
\vdots & \vdots & \ddots & \vdots & \vdots \\
\hline
0 & 0 & \cdots & 0 & 0 \\
0 & 0 & \cdots & W_d^{\frac{1}{2}} & 0 \\
\hline
0 & 0 & \cdots & 0 & 0 \\
0 & 0 & \cdots & 0 & W_d^{\frac{1}{2}}
\end{array}\right],$$

$$C_D = \left[\begin{array}{cc|cc|cc|cc|cc}
I & 0 & 0 & 0 & \cdots & \cdots & 0 & 0 & 0 & 0
\end{array}\right],$$

$$C_f = \left[\begin{array}{cc|cc|c|cc|cc}
I & 0 & 0 & 0 & \cdots & 0 & 0 & 0 & 0 \\
\hline
0 & 0 & I & 0 & \cdots & 0 & 0 & 0 & 0 \\
\hline
\vdots & \vdots & \vdots & \vdots & \ddots & \vdots & \vdots & \vdots & \vdots \\
\hline
0 & 0 & 0 & 0 & \cdots & I & 0 & 0 & 0 \\
\hline
0 & 0 & 0 & 0 & \cdots & 0 & 0 & I & 0
\end{array}\right],\tag{2.4}$$

and where the signals $\{w_{d,k}^{(i)}\}$ and signals $\{v_{f,k}^{(i)}\}$ are unit-variance and white. The signal $v_{f,k}$, which is scaled by positive definite matrix V_f, is included for the feasibility of controllers designed according to this framework.

The forecast signal model posed above provides a flexible framework for capturing the behavior forecast data quality in numerous scenarios. The selection of where to place upstream disturbance sensors, or where to measure forecast information along the horizon, is captured by selection of the corresponding partitioned block rows of the forecast measurement matrix C_f in (2.4). Each forecast component, $d^{(i)}$, has identical stable spectral factor, G_d, but becomes decreasingly correlated, with the actual disturbance d with increasing lead time i. The rate of decorrelation can be selected by the designer in a systematic way using the parameters $\alpha^{(j)}$ as seen in the following theorem.

Theorem 1 *Let the $\{w_{d,k}^{(i)}\}$ (with $i = 1, \ldots, N$) be independent, zero-mean, unit-variance, white noise signals. Denote the lag-τ cross-correlation between forecast signals $d^{(p)}$ and $d^{(q)}$ by*

$$R_{(p,q)}(\tau) = E\left\{ d_k^{(p)} d_{k-\tau}^{(q)}{}^T \right\},$$

then

$$R_{(p,p)}(\tau) = R_{(q,q)}(\tau), \tag{2.5}$$

for all p, q and τ. Further,

$$R_{(m,m+n)}(\tau) = \prod_{l=m}^{m+n-1} \left[\alpha^{(l)} \right] R_{(m,m)}(\tau - n). \tag{2.6}$$

Proof:
By construction, the forecast signal model yields the following formula for $d^{(m)}$ in terms of $d^{(m+n)}$:

$$d_k^{(m)} = \prod_{l=m}^{m+n-1} \left[\alpha^{(l)} \right] d_{k-n}^{(m+n)} + \beta^{(m)} G_d(z) w_{d,k-1}^{(m)}$$
$$+ \sum_{i=m+1}^{m+n-1} \left[\left(\prod_{j=m}^{i} \left[\alpha^{(j)} \right] \right) \beta^{(i)} G_d(z) w_{d,k-i+1}^{(i)} \right], \tag{2.7}$$

with parameters $\beta^{(p)}$ defined as in (2.3). Applying (2.7) to the correlation function

$R_{(m,m+n)}(\tau)$, and recalling the independence of the signals $\{w_{d,k}^{(i)}\}$,

$$R_{(m,m+n)}(\tau) = \mathrm{E}\left\{ d_k^{(m)} d_{k-\tau}^{(m+n)^T} \right\},$$

$$= \mathrm{E}\left\{ \left(\prod_{l=m}^{m+n-1} \left[\alpha^{(l)}\right] d_{k-n}^{(m+n)} + \beta^{(m)} G_d(z) w_{d,k-1}^{(m)} \right.\right.$$

$$\left.\left. + \sum_{i=m+1}^{m+n-1} \left[\prod_{j=m}^{i} \left[\alpha^{(j)}\right] \beta^{(i)} G_d(z) w_{d,k-i+1}^{(i)} \right] \right) d_{k-\tau}^{(m+n)^T} \right\},$$

$$= \prod_{l=m}^{m+n-1} \left[\alpha^{(l)}\right] \mathrm{E}\left\{ d_{k-n}^{(m+n)} d_{k-\tau}^{(m+n)^T} \right\}.$$

Since the signal $d^{(m+n)}$ is stationary and all $d^{(i)}$ signals have the same auto-correlation functions, i.e. $R_{(m,m)}(\tau) = R_{(m+n,m+n)}(\tau)$, then $R_{(m,m+n)}(\tau)$ can be written as

$$R_{(m,m+n)}(\tau) = \prod_{l=m}^{m+n-1} \left[\alpha^{(l)}\right] \mathrm{E}\left\{ d_{k-n}^{(m+n)} d_{k-\tau}^{(m+n)^T} \right\},$$

$$= \prod_{l=m}^{m+n-1} \left[\alpha^{(l)}\right] \mathrm{E}\left\{ d_k^{(m+n)} d_{k-\tau+n}^{(m+n)^T} \right\},$$

$$= \prod_{l=m}^{m+n-1} \left[\alpha^{(l)}\right] R_{(m+n,m+n)}(\tau - n),$$

$$= \prod_{l=m}^{m+n-1} \left[\alpha^{(l)}\right] R_{(m,m)}(\tau - n).$$

$\square$

As a direct corollary, the role of the $\alpha^{(j)}$ parameters in capturing the rate of decorrelation between an arbitrary i-step ahead disturbance forecast $d^{(i)}$ and the actual disturbance d can be directly calculated.

Corollary 1 *Define the lag-τ auto-correlation function of disturbance d as $R_{dd}(\tau) = E\left\{ d_k d_k^T \right\}$. The cross-correlation between disturbance signal d and $(i-1)$-ahead forecast signal $d^{(i)}$ satisfies*

$$E\left\{ d_k d_{k-\tau}^{(i)} \right\} = \prod_{l=1}^{i-1} \left[\alpha^{(l)}\right] R_{dd}(\tau + 1 - i). \tag{2.8}$$

Note that the selection $\alpha^{(j)} = 1$ for every j yields the characterization of exact disturbance forecast data.

The effect of the $\alpha^{(j)}$ parameters on the forecast data quality is visualized in the simple numerical example plotted in Figure 2.6, where we select a forecast horizon of $N = 3$ and the decorrelation parameters are selected as $\alpha^{(1)} = \alpha^{(2)} = \alpha^{(3)} = 0.96$, which modulate the scaled reduction between the cross-correlation functions with increasing look-ahead time.
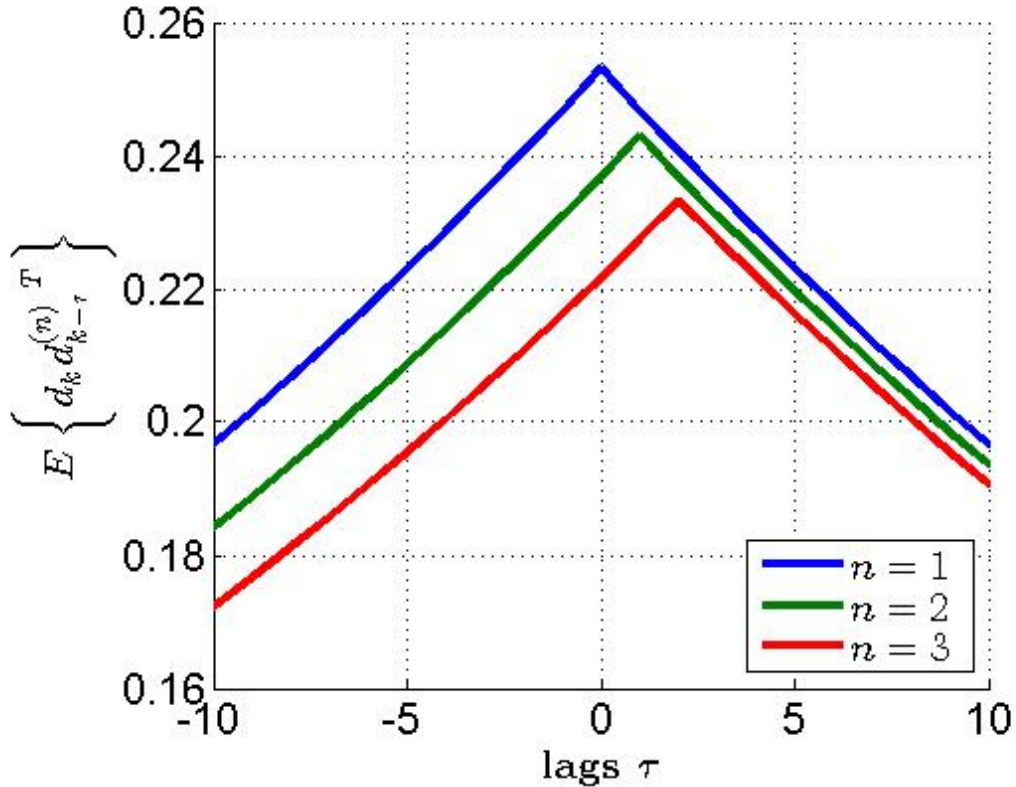
Figure 2.6: Cross-correlation functions between d and $d^{(1)}$, d and $d^{(2)}$, and d and $d^{(3)}$ with $\alpha^{(j)} = 0.96$.

2.4 Feedforward controller design

Associated with the forecast signal model and in order to derive the corresponding feedback/feedforward optimal controller, we pose an optimal control problem. The con-

trol objective is to design *controller* $\mathcal{K}$ to reject disturbance d_k, where $\mathcal{K}$ receives two measurements:

1. feedback measurement y_k from the plant and

2. forecast measurement $y_{f,k}$, which contains present and upstream information about disturbance d_k.

The driving signal and performance output signal of the optimal control problem are

$$\xi_k = \begin{bmatrix} w_k \\ w_{D,k} \\ v_k \\ v_{f,k} \end{bmatrix}, \quad z_k = \begin{bmatrix} Q^{\frac{1}{2}} y_k \\ R^{\frac{1}{2}} u_k \end{bmatrix}, \tag{2.9}$$

where $Q \geq 0$ and $R > 0$ are matrix performance weights. This is illustrated in Figure 2.7. The optimal control problem can be posed as LQG (or $\mathcal{H}_2$) using the MATLAB
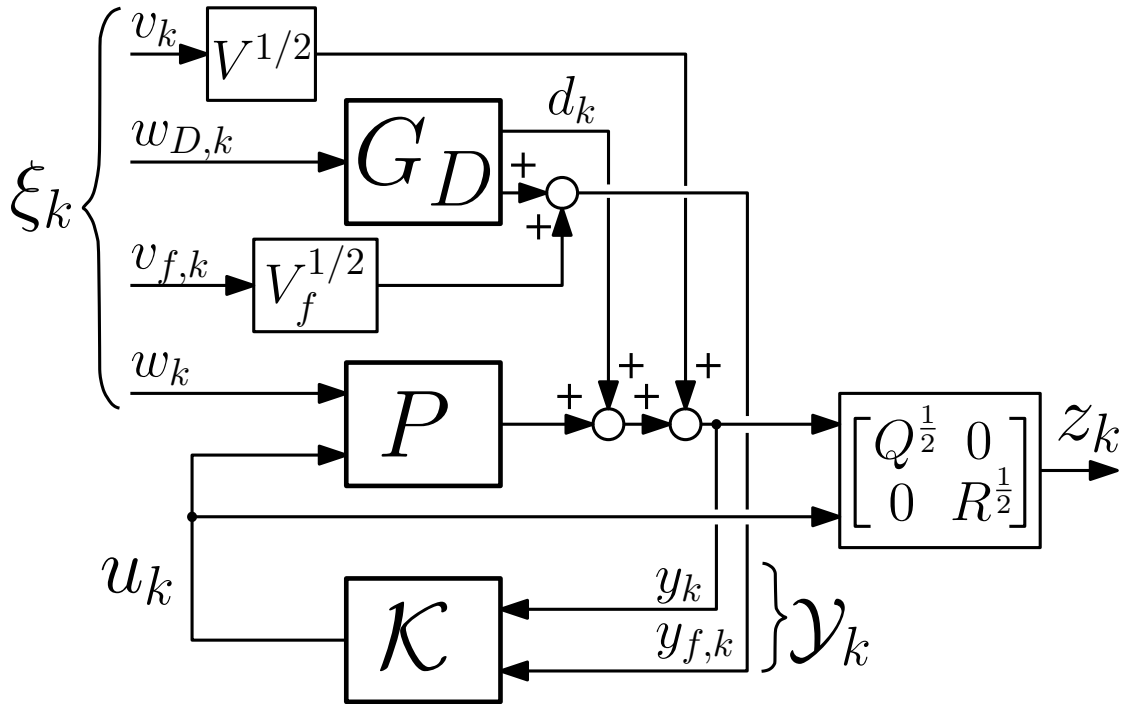
Figure 2.7: Feedforward control problem under consideration.

function h2syn or as an $\mathcal{H}_\infty$ problem using hinfsyn.

The linear system from (ξ_k, y_k) to (z_k, u_k) is as follows.

$$\left[\begin{array}{c} \mathcal{X}_{k+1} \\ \hline z_k \\ \hline \mathcal{Y}_k \end{array}\right] = \left[\begin{array}{c|cc} \mathcal{A} & \mathcal{B}_1 & \mathcal{B}_2 \\ \hline \mathcal{C}_1 & \mathcal{D}_{11} & \mathcal{D}_{12} \\ \hline \mathcal{C}_2 & \mathcal{D}_{21} & 0 \end{array}\right] \left[\begin{array}{c} \mathcal{X}_k \\ \hline \xi_k \\ \hline u_k \end{array}\right],$$

where

$$\mathcal{X}_k = \begin{bmatrix} x_k \\ x_{D,k} \end{bmatrix}, \ \mathcal{Y}_k = \begin{bmatrix} y_k \\ y_{f,k} \end{bmatrix},$$

$$\mathcal{A} = \begin{bmatrix} A & 0 \\ 0 & A_D \end{bmatrix},$$

$$\left[\begin{array}{c|c} \mathcal{B}_1 & \mathcal{B}_2 \end{array}\right] = \left[\begin{array}{cccc|c} W^{\frac{1}{2}} & 0 & 0 & 0 & B \\ 0 & B_D & 0 & 0 & 0 \end{array}\right],$$

$$\left[\begin{array}{c} \mathcal{C}_1 \\ \hline \mathcal{C}_2 \end{array}\right] = \left[\begin{array}{cc} Q^{\frac{1}{2}}C & Q^{\frac{1}{2}}C_D \\ 0 & 0 \\ \hline C & C_D \\ 0 & C_f \end{array}\right],$$

$$\left[\begin{array}{c|c} \mathcal{D}_{11} & \mathcal{D}_{12} \\ \hline \mathcal{D}_{21} & 0 \end{array}\right] = \left[\begin{array}{cccc|c} 0 & 0 & Q^{\frac{1}{2}}V^{\frac{1}{2}} & 0 & 0 \\ 0 & 0 & 0 & 0 & R^{\frac{1}{2}} \\ \hline 0 & 0 & V^{\frac{1}{2}} & 0 & 0 \\ 0 & 0 & 0 & V_f^{\frac{1}{2}} & 0 \end{array}\right].$$

We pose the following control problem

$$J = \min_{\mathcal{K}} \|H_{z\xi}\|_{2 \ or \ \infty}, \tag{2.10}$$

where $H_{z\xi}$ is the transfer function from ξ to z, and only causal controllers $\mathcal{K}$ are admissible.

When an $\mathcal{H}_2$ control law is implemented, all exogenous signals are assumed to be independent white noise with distribution $\xi \sim \mathcal{N}(0, I)$, and signal covariances are captured by the matrices $\{W, B_D, V, V_f\}$. When an $\mathcal{H}_\infty$ control law is used, all exogenous signals are deterministic unit-energy L_2 signals, and the scaling of the exogenous signals is captured by the matrices $\{W, B_D, V, V_f\}$.

Both $\mathcal{H}_2$ and $\mathcal{H}_\infty$ control laws yield scalar performance criteria, J, in the form (2.10), allowing for explicit assessment of the benefits of adding or improving feedforward data.

2.5 Addressing the design questions with an example

In order to address the design questions and demonstrate the features of the proposed design framework, we pose an illustrative numerical example with assigned values given in Table 2.1. For simplicity we solve only for $\mathcal{H}_2$ controllers.

Table 2.1: Illustrative numerical example for control problem in Figure 2.7.

Model/Variable	Assigned Values	
Plant P	$A = 0.99$ $\qquad B = 1$ $C = 0.02$	
Disturbance-generating system G_d	$A_d = 0.975$ $\qquad W_d^{\frac{1}{2}} = \sqrt{5}$ $C_d = 0.05$	
Performance weights	$Q = 5000$ $\qquad R = 10$	
Sample time	$T_s = 0.1$ s	
Scaling matrices $(i = 1, \dots, N)$	$W = 0.3$ $\qquad V = 0.003$ $V_f^{(i)} = 1 \times 10^{-6}$	
Cases of α values $(j = 1, \dots, N-1)$	1. *small* α	$\alpha^{(j)} = 0.85$
	2. *moderate* α	$\alpha^{(j)} = 0.96$
	3. *large* α	$\alpha^{(j)} = 0.999$

2.5.1   Evaluating and comparing performance of control designs

We can now address design question (Q1) by solving the numerical example in the case where the forecast measurement y_f contains the full horizon of upstream disturbance information along the forecast up to horizon length N, $\{d^{(1)}, \ldots, d^{(N)}\}$. Thus, matrix C_f contains all block rows as in (2.4). We solve this problem for the three sets of α values and for all horizons in the range $N = 1, \ldots, 10$. The resulting closed-loop $\mathcal{H}_2$ performance is shown in Figure 2.8.
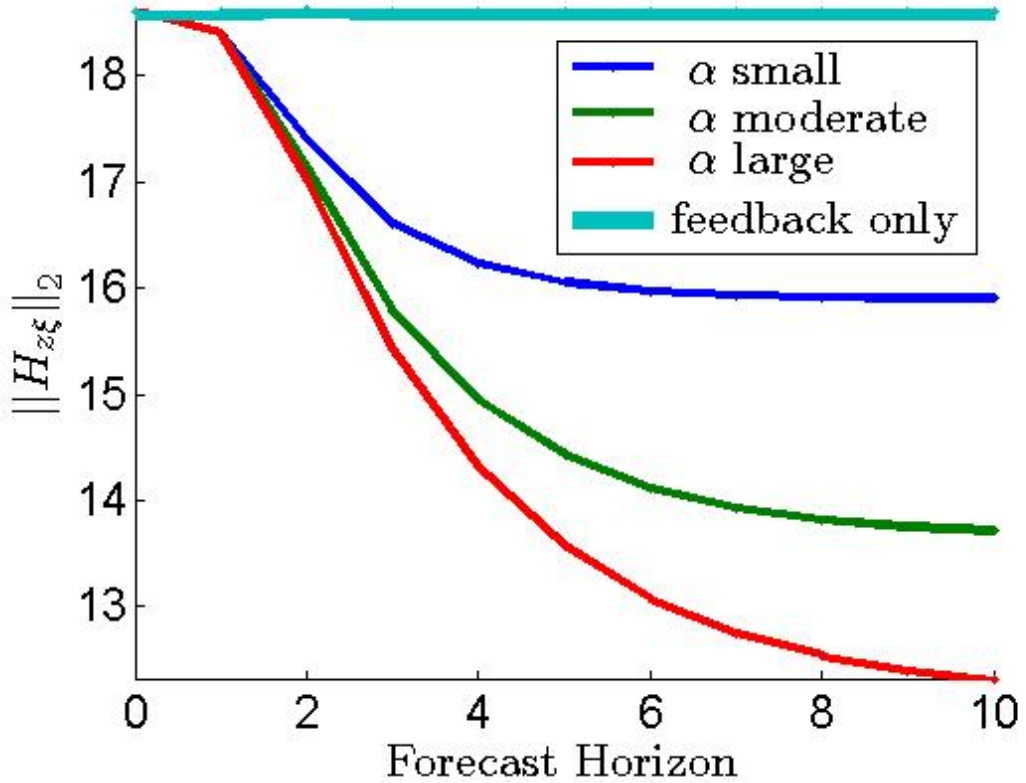
Figure 2.8: Closed-loop performance with fully populated forecasts y_f at different horizon lengths N solved for various α values.

Figure 2.8 demonstrates the reduction in feedforward benefit with decorrelation of the forecast data from the arriving disturbance. Beyond this, it also shows, with data available along the entire horizon: (i) the characteristic asymptote of the closed-loop performance as the horizon increases, and (ii) the knee in the performance curve beyond which returns are diminished. These latter items are aspects evident in the equivalent

plots from [13] with perfect forecasts.

2.5.2 Determining the placement of forecast sensors

We consider a forecast measurement corresponding to placing an upstream sensor at N time steps ahead of the plant, which is accommodated in the framework by selecting the measurement matrix C_f to be the $(N-1)th$ block row of the full C_f matrix given by (2.4). The corresponding closed-loop $\mathscr{H}_2$ performances for the working example solved at various sensor placement positions $N = 1, \ldots, 10$ is shown in Figure 2.9.
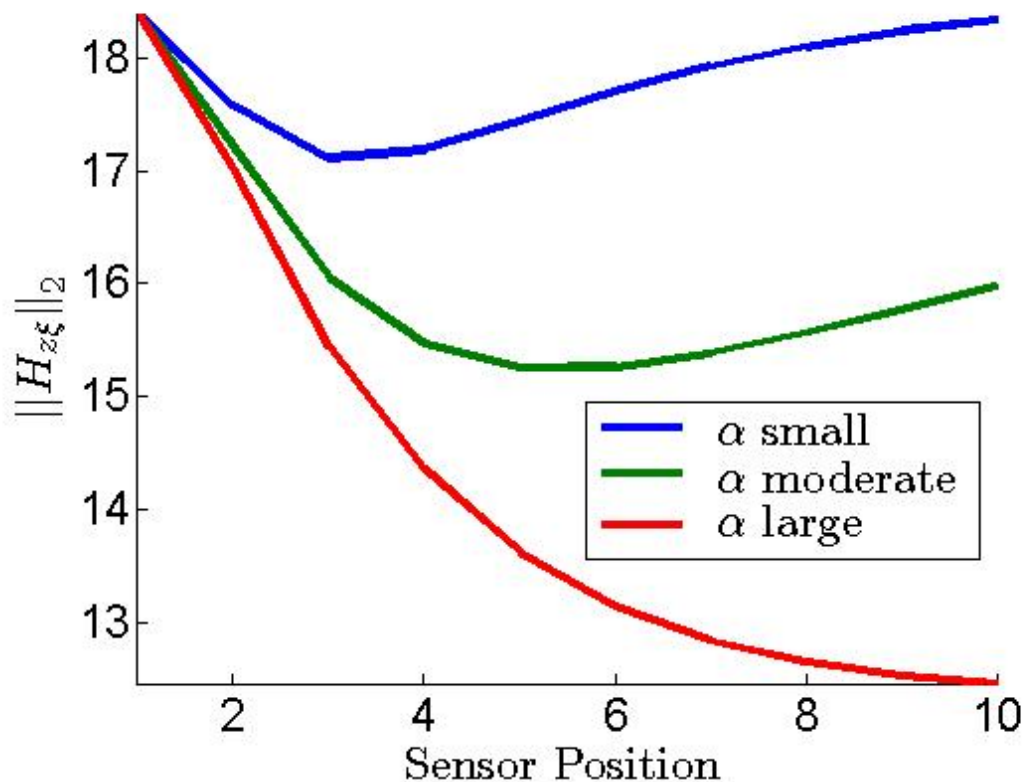
Figure 2.9: Closed-loop performance with a single sensor placed at various upstream positions N solved for small, moderate, and large values of α.

For the case where the α parameters are large, the disturbance propagating through the forecast signal model retains much of its coherence, resulting in improved performance with increasingly upstream sensor placement, with an optimal sensor position at $N = 10$. For the case where the α parameters are of moderate size, the value of in-

creasingly upstream disturbance information experiences diminishing performance improvements, resulting in an optimal sensor position at $N = 5$. Likewise, for small α values, the reduction in the coherence of disturbance information is even more extreme, and any sensor placed anywhere other than at the position of $N = 3$, will have reduced performance.

2.5.3 Selecting forecast sensors

The adoption of an improved sensor might become evident in two ways: increase in the values of $\alpha^{(j)}$ reflecting better coherence with the arriving disturbance, and decrease in the associated sensor noise variance V_f. Applying the former view, Figure 2.9 may now be reinterpreted as delivering performance of $||H_{z\xi}||_2 = 17.1088$ for a low quality sensor (small α value case) optimally placed at position $N = 3$ versus a performance of $||H_{z\xi}||_2 = 15.2549$ for a higher-quality sensor (moderate α value case) located at position $N = 5$. The analysis of the benefits of placement of multiple sensors can proceed via exhaustive testing of options.

2.6 Chapter Summary

This work presents a model to characterize disturbance forecast data for feedforward control design that builds upon the standard finite tapped-delay-line by using the (de)correlation between the disturbance forecast measurement and the eventual disturbance signal. A set of parameters, $\{\alpha^{(j)}\}$, is included in the model, by construction, to quantify the correlation between forecast and disturbance signals.

Further exploration could address applications and limitations of the proposed approach in a practical context. Although not demonstrated directly in this work, the proposed framework can easily be adapted to: produce $\mathscr{H}_\infty$-optimal controllers; incorporate disturbances affecting the plant through channels other than additive to the output; include reference tracking; and other extensions. The presented approach relies heavily on the knowledge of disturbance-generating model and associated forecast signal model. Therefore, the question of robustness of the control designs produced from this method should be considered in future work. Particularly in the case of uncertain models for the

plant, the disturbance-generating process, and the disturbance propagation model.

It is worth stressing that, practically speaking, the signal model of a stationary discrete-time stochastic process may be derived directly from its correlation properties. (See the discussion in [23], Section 9.2.) A Stochastic Realization Problem can be posed using the correlation to yield a finite-dimensional linear signal model, G_d. Further, where the plant and disturbance model are jointly fitted via least-squares system identification, again it is the second-order statistics or correlations which dictate the parametrized fit, [24]. Thus, the technique of managing forecast data through correlation properties would appear to fit this process well.

2.7 Acknowledgments

This chapter contains material adapted from Robert H. Moroto, Robert R. Bitmead, and Bram Sleegers, "The Information Structure of Feedforward/Preview Control Using Forecast Data," *The 19th World Congress of the International Federation of Automatic Control*, Aug. 2014.

Chapter 3

Improving Disturbance Compensation With Event-Triggered Logic Signals

3.1 Introduction

In this paper, we provide a framework for improving estimates of load demand for a gas turbine, used for power generation on a microgrid in island mode operation, by making use of both measured physical signals, as are usually applied for estimation and feedback control, and electrical breaker status data, an event-triggered logic signal providing nearly immediate indication of a change in load demand, i.e. real power demand, typically measured in megawatts. In power grids relying primarily on gas turbine (GT) power sources, such as island mode applications, the load demand mostly meanders slowly about nominal values except when nearly instantaneous shifts occur in the load value, such as those due to electrical breakers connecting or disconnecting equipment to or from the grid [25]. Frequency regulation in synchronous machine applications dictates a fixed rotational shaft speed and thus, the primary control objective is to maintain the shaft speed at the grid frequency through fuel regulation. Although sudden changes in load demand are eventually compensated by the feedback control system, reaction delays can result in sharp and possibly undesirable fluctuations in electrical frequency, potentially initiating unplanned shutdowns due to frequency-triggered fault protections. The control system attempts to minimize the effect of load on shaft speed error. Shaft

power on electric generators driven by GT's is inferred from the output power of the generator through voltage and current transformers. However, direct measurements of voltages and electrical currents can be very noisy or unreliable. Heavy filtering is often used to clean up these voltage and current measurements, and although the resulting load estimate is sufficient for regular operation, it can be too slow for the control system to use in real-time with a major load change. This heavy filtering introduces a delay which forces traditional feedback GT controllers to wait for changes in shaft speed to be detected before compensation can occur. If the controller were to have more immediate knowledge of sudden onloads and offloads, then shaft speed could be regulated in a more timely fashion, improving closed-loop regulation performance. Even though such quantitative load information is not readily available, logic signals monitoring the circuit breakers are already simply and rapidly acquired by the turbine control system without impinging significantly on the client's operation. Additionally, statistical information pertaining to the transient loads induced by changes in breaker status can be easily obtained from the historical data record. We derive a systematic approach to augmenting plant analog signals with breaker logic signals, and transient load statistics, to yield a faster load estimator. At this stage, we do not yet consider the associated control problem.

In order to improve load estimation, we propose a Kalman filtering signal estimation framework that not only uses the physical measurements traditionally fed back to the GT control system, but also incorporates the status of the electrical breakers that regulate the connection of separate pieces of equipment to a GT-powered grid , as well as the statistical properties of the transient loads associated with a change in breaker status. This approach, inspired by ideas from [26], provides a simple and systematic framework for incorporating logic signals, like the status of electrical breakers, into the well understood and often implemented linear Kalman filter design process, even though logic-valued signals do not conform to the linear genesis of Kalman filtering [27, 28]. The computational load associated with Kalman estimator is manageable for implementation in any modern GT control framework.

Although a GT is a complex piece of machinery, it has been shown in [29] that its behavior can be adequately described, for control purposes, by a parameter-dependent

family of LTI models which can be readily identified by applying a closed-loop system identification method, such as those discussed in [24] and [30]. Thus, LTI models are used here.

This work provides several primary contributions. The problem of exploiting the electrical breaker signals of driven equipment in a GT-powered microgrid for the purpose of enhancing the estimation performance of the GT load is, to the authors knowledge, itself novel. A thorough search of relevant literature yielded only one closely related work, [31], where the generator breaker of the GT, not the driven equipment breakers, was used to trigger an alternative GT control routine that prevents flameout during a loss of load condition.

Another contribution of this work is the development of a load model that captures the breaker signal switching behavior and is appropriate for Kalman filtering. The study of switched dynamical systems is a mature topic with many branches of specialization. A switched model that is closely related to this work is the discrete-time Markov jump linear system (MJLS), see [32], [33], and [34]. MJLS models assume that the switching signal evolves according to a Markov chain, and thus require knowledge of the transition probabilities of the switching signal, which can be difficult to determine in practice. Instead, the proposed approach uses knowledge of the mean and variance of the load transient, which are often obtainable from data records.

3.2 Nomenclature

GT	Gas turbine
LTI	Linear time-invariant
N_{GP}	Rotational Shaft Speed of Gas Producer
P_2	Pressure of GT compressor discharge
T_5	Temperature of 5th stage GT power turbine
θ	Breaker status signal
P	Identified closed-loop GT Plant model
l	total load deviation from nominal (disturbance)
y	measured output signal of P

u_s	supplementary control input signal of P
w	process noise signal of P
v	measurement noise signal of P
x	state of P
B	base load model
l_b	base load disturbance contribution of B
w_b	base load driving noise signal of B
x_b	state of B
D	load shift model
l_d	load shift disturbance contribution of D
ζ	switched load shift input signal of B
ξ	load shift driving noise signal prior to switching
x_d	state of D
$\mathcal{X}$	Augmented model state
$\mathcal{W}$	Augmented process noise signal
$\mathcal{K}_e$	Augmented model state estimator
K	Augmented model state estimator gain
Σ	Augmented model state estimator error covariance
$\hat{}$	Indication of an estimated variable
i.i.d.	Independent and identically distributed
$\gamma \sim \mathcal{N}(\bar{\gamma}, \Gamma)$	Normally distributed stochastic variable γ with mean $\bar{\gamma}$ and covariance matrix Γ
$\mathrm{E}\{\cdot\}$	Expected value
$M \geq 0$	Nonnegative definite matrix M
$M > 0$	Positive definite matrix M
$\mathrm{cov}(\cdot, \cdot)$	Covariance

3.3   Physical Setup

We consider a 5 MW dry low-emission GT power generation system acting as the sole power source for an electrical microgrid in island mode operation. Examples of which include backup power generation applications for hospitals and universities, as well as primary power generation for some remote locations with low reliability or no grid-quality electricity access. In this case, large abrupt changes in power production/-consumption can destabilize a local portion of a large electrical grid. By the same token, the adoption of highly variable renewable sources into a network can create integration and stability issues, which effects might be ameliorated by improved information availability and management. The power produced by the turbine is supplied to a collection of individual loads in the microgrid, including a high-power device $\mathcal{L}$ (e.g. a motor or compressor) whose connection to the microgrid is governed by an instrumented circuit breaker, which provides a switching signal measurement $\theta(k)$, defined at time k by

$$\theta(k) = \begin{cases} -1 & , \quad \text{if the breaker opens at time } k, \\ 0 & , \quad \text{if the breaker does not change at time } k, \\ 1 & , \quad \text{if the breaker closes at time } k. \end{cases} \tag{3.1}$$

In steady state operation, the controller regulating the GT system attempts to mitigate the effect of transient deviations of the total microgrid load with respect to some constant nominal load value. This total load deviation $l(k)$ acts as a disturbance impinging on the GT system and is regulated by the nominal controller. When the breaker associated with device $\mathcal{L}$ switches open or closed, the total microgrid load deviation $l(k)$ will shift instantaneously to a new but unknown value.

The primary goal of this work is to develop an approach to augmenting the GT feedback controller, based on local turbine signals, to incorporate the switching signal $\theta(k)$. This proceeds by constructing an online estimate of microgrid load deviation disturbance $l(k)$ which uses: the existing feedback measurements; the breaker switching signal $\theta(k)$; and knowledge of the load statistics associated with the device $\mathcal{L}$ breaker switching event. We proceed by formulating a set of models which make the problem under consideration amenable to standard Kalman filtering techniques in spite of the presence of the ternary-logic signal, $\theta(k)$. The resultant filter is time-varying, however.

The corresponding estimator for the controlled plant state and the load deviation disturbance $l(k)$ is then presented. A numerical example is constructed to demonstrate the proposed estimator, and we conclude by considering potential future research directions and applications for the considered modeling framework and associated estimator. In this work, we focus solely on the estimation problem. Design of a control law will be addressed in subsequent work.

3.4   Model Formulation
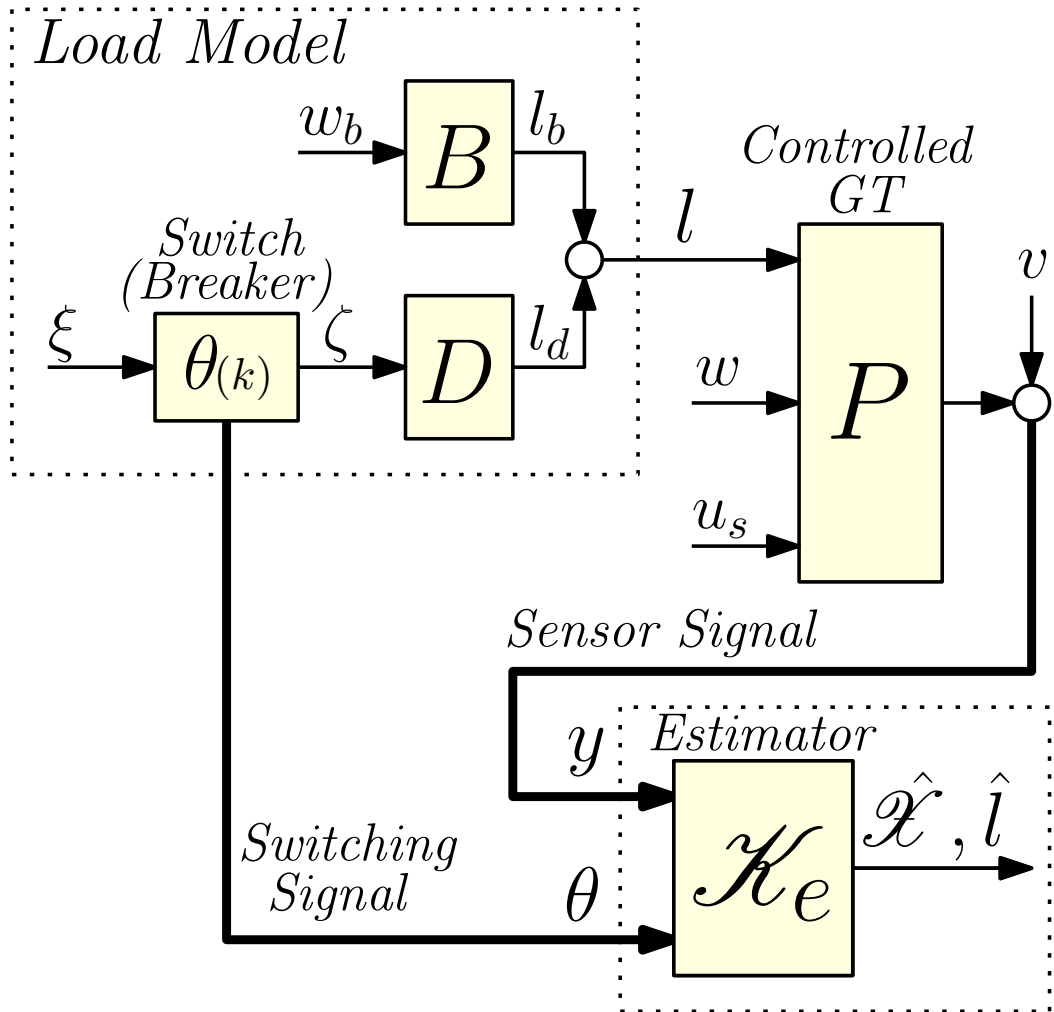
Figure 3.1: Model Framework Block Diagram

3.4.1 GT System Model P

We characterize the microgrid power generation GT under standard feedback control with the following state variable model, denoted by P:

$$x(k+1) = Ax(k) + Bu_s(k) + w(k) + B_l l(k), \qquad (3.2)$$

$$y(k) = Cx(k) + v(k), \qquad (3.3)$$

where (3.2-3.3) is a linearized model of the closed-loop controlled GT operating around nominal load and nominal state values. Such a model has, for example, been identified from high-fidelity simulation data in [29]. A high-level overview of GT modeling methods can be found in [30]. $x(k) \in \mathbb{R}^n$ denotes the state of P at time k. Control signal $u_s(k) \in \mathbb{R}^m$ is a supplemental control input which is unused in this analysis, because we focus on novel estimation aspects alone, but is included to accommodate the insertion of further control actions around the current subsumed controller exploiting the improved load estimates proposed here. $y(k) \in \mathbb{R}^p$ is the measured sensor data corresponding to the standard analog GT output quantities which also enter the existing attendant GT controller subsumed by model P. Process noise $w(k) \in \mathbb{R}^n$ and measurement noise $v(k) \in \mathbb{R}^p$ are stochastic noise signals defined for later use in constructing the Kalman state estimator.

3.4.2 Total Load Deviation Signal $l(k)$ Models

Load $l(k) \in \mathbb{R}$ is the total deviation of the GT load from the nominal value and is comprised of two parts: a slowly varying base load $l_b(k) \in \mathbb{R}$ characterizing the steady state behavior of the load variations, and a load shift $l_d(k) \in \mathbb{R}$ characterizing the instantaneous load jumps that occur during breaker switching. Loads $l_b(k)$ and $l_d(k)$ sum to yield the total deviation in the load from nominal, i.e. $l(k) = l_b(k) + l_d(k)$, where the meandering of the load is captured by $l_b(k)$ which, in turn, embodies the summed variations in unswitched and switched loads. The subsumed feedback controller in P is designed to achieve minimal steady state error induced by changes in the load $l(k)$. However, due to the feedback construction, the control bandwidth is limited by feedback delays and the dynamics of the closed loop system, which is not designed to make use

of the breaker signal $\theta(k)$. At switching times, the load shift l_d is modeled as taking a new random value with a known mean and variance reflecting statistical switched-load properties. The inclusion of the breaker signal $\theta(k)$ permits more rapid estimation of the change in load immediately following switching. The result is a time-varying estimator.

For the base load model, we define the state variable model B, given by

$$x_b(k+1) = A_b x_b(k) + B_b w_b(k), \tag{3.4}$$

$$l_b(k) = C_b x_b(k), \tag{3.5}$$

where $x_b(k) \in \mathbb{R}^{n_b}$ is the state and $w_b(k) \in \mathbb{R}^{m_b}$ is the driving noise signal, and $l_b(k)$ is the base load.

The load shift is modeled by the system D, which captures instantaneous changes indicated by $\theta(k)$, and is an offset to the load $l(k)$. D is given by

$$x_d(k+1) = x_d(k) + \zeta(k), \tag{3.6}$$

$$l_d(k) = x_d(k) + \zeta(k), \tag{3.7}$$

where $x_d(k) \in \mathbb{R}$ is the state, $l_d(k)$ is the switched load shift offset, and $\zeta(k)$ is defined by

$$\zeta(k) = \theta(k)\xi(k), \quad \text{with } \xi(k) \sim \mathcal{N}\left(\bar{\xi}, \Xi\right). \tag{3.8}$$

The parameters of the distribution of load change, mean $\bar{\xi}$ and covariance Ξ, quantify the statistical properties of the switched load, and are assumed to be known. Since the breaker signal $\theta(k)$ indicates transitions only, this yields the switched load as the sum of a sequence of random variables $\zeta(k)$.

$$l_d(k) = x_d(k) + \zeta(k) = \sum_{j=0}^{k-1} \zeta(j) + \zeta(k) = \sum_{j=0}^{k} \zeta(j).$$

Figure 3.2 depicts a diagram illustrating how the load model construction produces a total load signal which captures the switching behavior of a breaker-connected load. The steady-state behavior of load deviation signal $l(k)$ is captured by the contribution of base load l_b. In the diagram, the breaker connecting the load to the microgrid is initially open and the state x_d, of the switching load dynamics, is zero. At time $k = k_1$ the breaker

closes, the breaker instrumentation takes the value $\theta(k_1) = 1$, and the mean of $l(k)$ is increased by adding a random value sampled from the distribution $\mathcal{N}\left(\bar{\xi}, \Xi\right)$. At time $k = k_2$ the breaker re-opens, the breaker instrumentation takes the value $\theta(k_2) = -1$, and the mean of $l(k)$ is decreased by subtracting a random value sampled from the distribution $\mathcal{N}\left(\bar{\xi}, \Xi\right)$. At all non-switching times (i.e $k \neq k_1, k_2$) we have $\theta(k) = 0$.
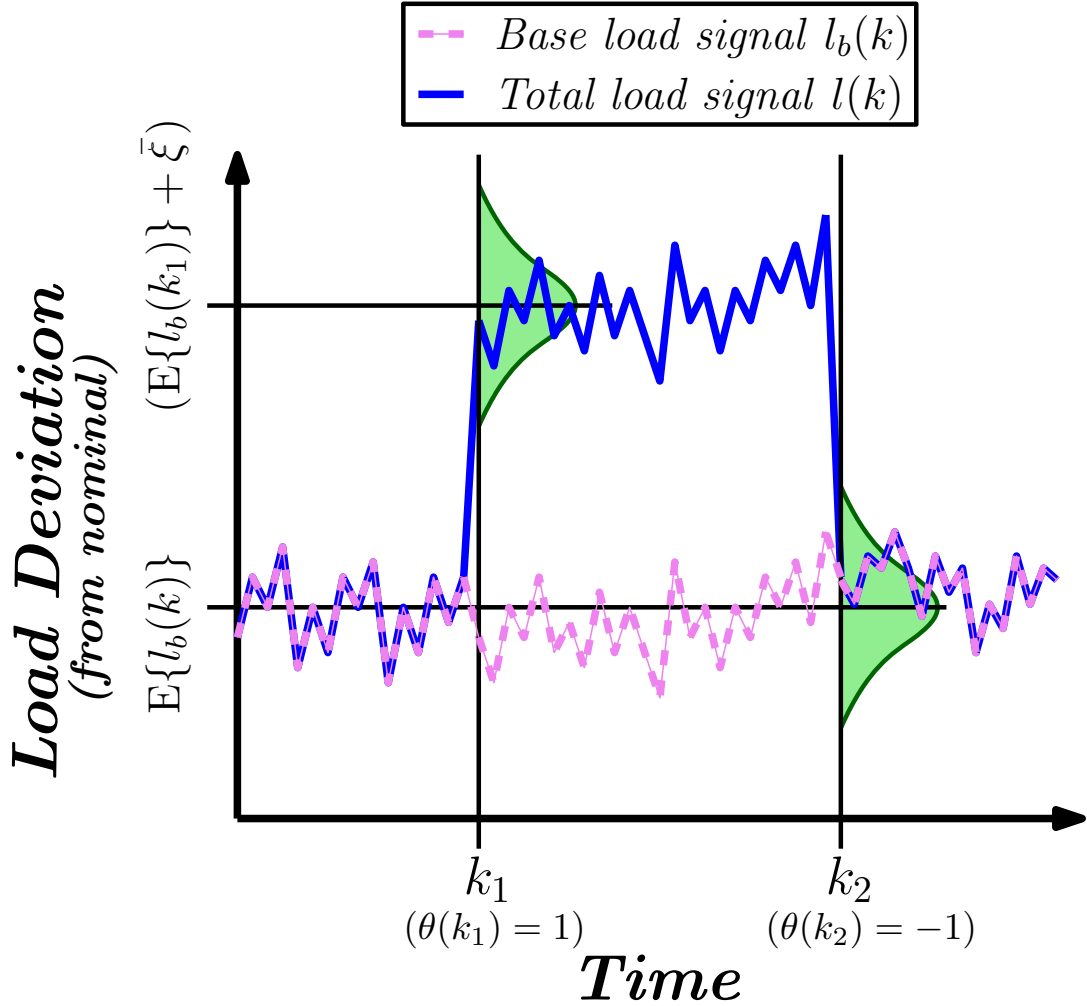
Figure 3.2: Diagram of load model operation with total load deviation $l(k)$ in solid blue, base load $l_b(k)$ in dashed violet, and probability density function of the load shift $l_d(k)$ in green. The breaker closes at time $k = k_1$ and opens at time $k = k_2$.

3.4.3 Augmented System Model

We amalgamate the state models P:(3.2-3.3), B:(3.4-3.5), and D:(3.6-3.7) into a single augmented model, the form of which will lend itself to the construction of a state estimator capable of leveraging the logic-valued breaker signal $\theta(k)$ in addition to the standard GT output measurement $y(k)$.

The augmented model has: state variable realization

$$
\mathcal{X}(k+1) = \mathcal{A}\mathcal{X}(k) + \mathcal{B}_u u_s(k) + \mathcal{B}_w \mathcal{W}(k)
$$
$$
+ \mathcal{G}\bar{\zeta}(k), \tag{3.9}
$$
$$
y(k) = \mathcal{C}\mathcal{X}(k) + v(k), \tag{3.10}
$$

with augmented signals

$$
\mathcal{X}(k) = \begin{bmatrix} x(k) \\ x_b(k) \\ x_d(k) \end{bmatrix}, \quad \mathcal{W}(k) = \begin{bmatrix} w(k) \\ w_b(k) \\ \check{\zeta}(k) \end{bmatrix}; \tag{3.11}
$$

augmented system matrices

$$
\mathcal{A} = \begin{bmatrix} A & B_l C_b & B_l \\ 0 & A_b & 0 \\ 0 & 0 & 1 \end{bmatrix}, \; \mathcal{B}_u = \begin{bmatrix} B \\ 0 \\ 0 \end{bmatrix}, \; \mathcal{B}_w = \begin{bmatrix} I & 0 & B_l \\ 0 & B_b & 0 \\ 0 & 0 & 1 \end{bmatrix},
$$
$$
\mathcal{G} = \begin{bmatrix} B_l \\ 0 \\ 1 \end{bmatrix}, \; \mathcal{C} = \begin{bmatrix} C & 0 & 0 \end{bmatrix}, \; \mathcal{Q}(k) = \text{var}(\mathcal{W}(k)); \tag{3.12}
$$

and switched-load offset and variation signals

$$
\bar{\zeta}(k) = \theta(k)\bar{\xi}, \quad \check{\zeta}(k) = \theta(k)\left(\xi(k) - \bar{\xi}\right). \tag{3.13}
$$

The total load deviation $l(k)$ can be expressed in terms of the augmented model variables as

$$
l(k) = \mathcal{C}_l \mathcal{X}(k) + \mathcal{D}_l \mathcal{W}(k) + \bar{\zeta}(k), \tag{3.14}
$$

where we define matrices $\mathcal{C}_l$ and $\mathcal{D}_l$ by

$$\mathcal{C}_l = \begin{bmatrix} 0 & C_b & 1 \end{bmatrix}, \quad \mathcal{D}_l = \begin{bmatrix} 0 & 0 & 1 \end{bmatrix}. \tag{3.15}$$

The signals defined by (3.13) imply $\zeta(k) = \bar{\zeta}(k) + \check{\zeta}(k)$, a decomposition which ensures augmented process noise $\mathcal{W}(k)$ is zero mean, and allows for knowledge of the switched-load mean value or offset $\bar{\zeta}(k)$ to be incorporated into an estimator in a similar fashion to known input signal $u_s(k)$. Signal $\check{\zeta}(k)$ then represents the variation of ζ around $\bar{\zeta}(k)$. Since, by construction (the controlled GT is modeled in P), $\mathcal{A}$ is stable. Accordingly: the matrix pair $(\mathcal{A}, \mathcal{C})$ is detectable; the pair $\left(\mathcal{A}, \mathcal{Q}(k)^{\frac{1}{2}}\right)$ will be (time-varying) stabilizable; and $V = \text{var}(v(k)) > 0$. The Kalman filtering problem is well-posed and the filter itself will be stable.

It is worth remarking that (3.9-3.10) yield a time-invariant system model driven by signals, $\bar{\zeta}(k)$ and $\check{\zeta}(k)$, which have time-varying statistical properties capturing the breaker logic signal $\theta(k)$. In the resultant Kalman filtering formulation, the known mean value, $\bar{\zeta}(k)$, enters in place of an exogenous control signal and the zero-mean Gaussian signal, $\check{\zeta}(k)$, augments the process noise variance. This Kalman filter is therefore time-varying, reflecting the presence of $\theta(k)$, even though the underlying system is linear time-invariant. Relation (3.14)) permits the calculation of a load estimate from the state estimate.

3.5 State Estimator

We collect the standard signal assumptions needed for the Kalman filter statement in the sequel.

Signal Assumptions *Noise signals w, w_b, ξ, and v are independent and identically distributed (i.i.d.), zero mean, normally distributed white noise signals which are mutually independent. The initial value of the augmented state estimate takes the value $\hat{\mathcal{X}}(0|-1) = \mathcal{X}_0^*$, a random variable, which is distributed, along with the noise signals,*

as follows:

$$
\begin{bmatrix} \mathcal{X}_0^* \\ w(k) \\ w_b(k) \\ \xi(k) \\ v(k) \end{bmatrix} \sim \mathcal{N} \left(\begin{bmatrix} \bar{\mathcal{X}}_0^* \\ 0 \\ 0 \\ \bar{\xi} \\ 0 \end{bmatrix}, \begin{bmatrix} \Sigma_0^* & 0 & 0 & 0 & 0 \\ 0 & W & 0 & 0 & 0 \\ 0 & 0 & W_b & 0 & 0 \\ 0 & 0 & 0 & \Xi & 0 \\ 0 & 0 & 0 & 0 & V \end{bmatrix} \right),
\tag{3.16}
$$

for all $k \geq 0$, with nonnegative definite covariances $W \geq 0$, $W_b \geq 0$, $\Xi \geq 0$, $\Sigma_0^* \geq 0$, and positive covariance $V > 0$.

State Estimator Solution

Given: the linear time-invariant system equations (3.9-3.10); auxiliary input signal $u_s(k)$; GT measured output signal $y(k)$; θ-dependent input signal $\bar{\zeta}(k)$; θ-dependent process noise covariance $\mathcal{Q}(k)$; time-invariant measurement noise covariance V; initial state estimate $\hat{\mathcal{X}}(0|-1) = \mathcal{X}_0^*$; and initial estimator error covariance $\Sigma(0|-1) = \Sigma_0^*$; the Kalman filter is immediate.

$$
K(k) = \Sigma(k|k-1)\mathcal{C}^T \left[\mathcal{C}\Sigma(k|k-1)\mathcal{C}^T + V \right]^{-1},
\tag{3.17}
$$

$$
\hat{\mathcal{X}}(k|k) = \hat{\mathcal{X}}(k|k-1) + K(k) \left[y(k) - \mathcal{C}\hat{\mathcal{X}}(k|k-1) \right],
\tag{3.18}
$$

$$
\Sigma(k|k) = \left[I - K(k)\mathcal{C} \right] \Sigma(k|k-1),
\tag{3.19}
$$

$$
\hat{\mathcal{X}}(k+1|k) = \mathcal{A}\hat{\mathcal{X}}(k|k) + \mathcal{B}_u u_s(k) + \mathcal{G}\bar{\zeta}(k),
\tag{3.20}
$$

$$
\Sigma(k+1|k) = \mathcal{A}\Sigma(k|k)\mathcal{A}^T + \mathcal{B}_w \mathcal{Q}(k)\mathcal{B}_w^T.
\tag{3.21}
$$

From (3.14) for $l(k)$, the associated load estimate follows.

$$
\hat{l}(k|k) = \mathcal{C}_l \hat{\mathcal{X}}(k|k) + \bar{\zeta}(k).
\tag{3.22}
$$

3.6   Numerical Example

We demonstrate the features of the proposed modeling and estimation framework via a numerical simulation using a linear identified model at this stage. We assign values to the models and signal realizations to calculate the time-varying Kalman filter with

access to measurements $y(k)$ and $\theta(k)$. We also construct a time-invariant Kalman filter with noise covariance design parameters selected to over-bound the distribution of the actual noise signals, as might be implemented if one only measures $y(k)$ without $\theta(k)$. The achieved estimator performance of the two state estimators is compared with respect to the quality of the estimated total load signal $l(k)$ and GT output signal $y(k)$.

Identified GT Model P

This numerical example is based on the closed-loop behavior of a Solar Turbines 5 megawatt GT operating under feedback control around 90% nominal load. The data is generated by a high-fidelity nonlinear GT simulation with its associated controller, while the Kalman estimator is derived from the identified linear model from [29]. This identified closed-loop system is a sixth-order state-space model with a delay of one sample, at sample period $T_s = 0.25s$, with a model structure given by that of (3.2-3.3). The normalized input and output signals of P are the following (nondimensionalized) physical quantities:

$$u_s(k) = \begin{bmatrix} u_f(k) & u_v(k) \end{bmatrix}^T, \tag{3.23}$$

$$y(k) = \begin{bmatrix} N_{GP}(k) & T_5(k) & P_2(k) \end{bmatrix}^T, \tag{3.24}$$

where u_f is the fuel control input signal, u_v is the guidevane control input signal, N_{GP} is GT gas producer rotational speed measurement signal, T_5 is the 5$^{\text{th}}$ stage GT temperature measurement signal; and P_2 is the GT compressor outlet pressure. For this simulation, the supplementary control signal has zero value, i.e. $u_s(k) = 0$, for all $k \geq 0$. The process noise $w(k)$ and measurement noise $v(k)$ are simulated with signal realizations possessing covariance matrices $W = (0.005)^2 I$ and $V = (0.10)^2 I$ respectively. The state of P is initialized at the value $x(0) = 0$.

Total Load Signal $l(k)$ and Model

The load is switched about its nominal value and the associated breaker logic signal is used in the state and load estimator developed above. As used in the development, the switched load consists of two parts: a constant offset to the baseload plus continued

variation of the baseload about this new value. The estimator equipped with the switching logic signal is compared to and contrasted with an alternative load estimator, which uses solely the plant measurements and which is tuned to balance transient response versus static accuracy. The numerical evaluation is in normalized units. If the estimator proposed in this work were to be applied to the design of a supplementary control signal $u_s(k)$, $l(k)$ would act as a disturbance on P. Figure 3.3 depicts step changes upwards and downwards in total load deviation (about nominal) in the simulation. Note that this signal represents a realistic load disturbance and is not generated via the disturbance model in the Kalman filter. In practice, this would represent the switching-in followed by the switching-out of part of the load. Signal $\theta(k)$ indicates the transition times: $\theta(30) = +1$ (at time $7.5s$), $\theta(90) = -1$ (at time $22.5s$), else $\theta(k) = 0$. The total duration of the simulation is $30s$.

The following variable assignments were used to generate the realization of base load $l_b(k)$: $A_b = \begin{bmatrix} 0.995 & 0 \\ 0 & 0.992 \end{bmatrix}$, $B_b = (0.1538)I$, $C_b = \begin{bmatrix} 0.9 & 0.1 \end{bmatrix}$, $W_b = (0.20)^2 I$, and $x_b(0) = 0$. The realization of the load offset signal was defined by

$$l_d(k) = \begin{cases} 1 & , \quad \text{for } 30 \leq k < 90, \\ 0 & , \quad \text{for } k \text{ otherwise.} \end{cases}$$

Breaker-Informed and Breaker-Uninformed Estimators

We consider two distinct load estimators. The *breaker-uninformed estimator* is derived using models P and B and measurement $y(k)$. The augmented PB-model is linear, time-invariant and is driven by process noises W and W_b, with the value chosen for W_b reflective of the total variation in the real load $l(k)$. This value of W_b will therefore be larger than that chosen for the breaker-informed case below, due to the absence of model D in the breaker-uninformed estimator. The effect of this choice of W_b will be discussed with the numerical results. This estimator is time-invariant. The time-invariant breaker-uninformed estimator was assigned design parameters $A_b = 0.99$, $B_b = 1$, $C_b = 1$, $W = (0.15)^2 I$, $V = (0.35)^2 I$, and $W_b = (0.04)^2$. The initial state estimate was initialized by $\hat{\mathcal{X}}(0|-1) = 0$. The time-invariant Kalman error covariance and gain, for the
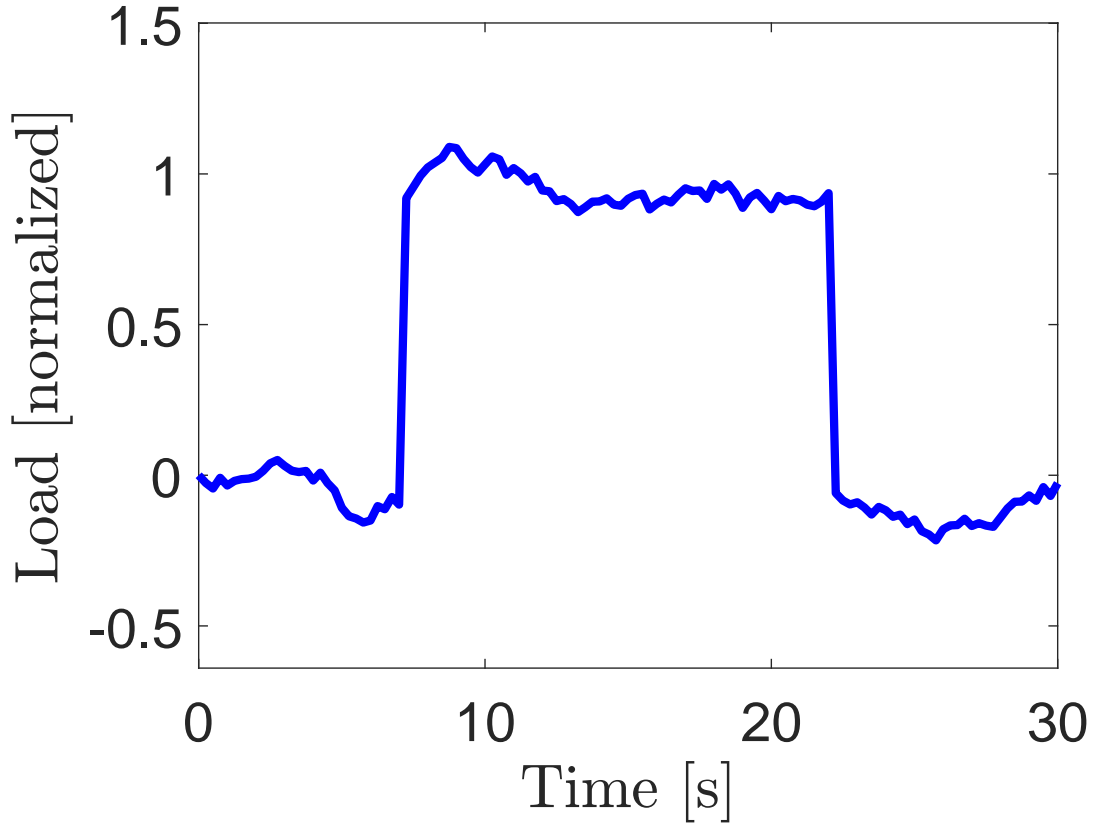
Figure 3.3: Total load deviation from nominal, $l(k)$.

PB system were calculated accordingly.

The *breaker-informed estimator* uses models P, B, and D and measurements $y(k)$ and $\theta(k)$. The PBD model is time-varying through the covariance $\mathcal{Q}(k)$, comprised of the matrix with block diagonal elements W, W_b and $(\theta(k))^2 \, \Xi$. and has a known exogenous input signal, $\bar{\zeta}(k)$. Because of the explicit presence of this latter covariance term, the value of W_b is diminished relative to the breaker-uninformed case. The resultant estimator is time-varying driven by the $\theta(k)$ signal. The time-varying breaker-informed estimator was assigned design parameters $A_b = 0.99$, $B_b = 1$, $C_b = 1$, $W = (0.15)^2 I$, $V = (0.65)^2 I$, $W_b = (0.09)^2$, $\bar{\xi} = 1.10$, and $\Xi = (0.65)^2$. The initial state estimate was initialized by $\hat{\mathcal{X}}(0|-1) = 0$ and the initial error covariance was selected as the solution to the discrete-algebraic Riccati equation fo the augmented PBD system in (3.9-3.10).

Comparative Estimator Performance

In comparing estimators there are two central aspects: the capacity of the estimator to track variations in the target signal, and the ability of the estimator to smooth out noise and so provide an accurate estimate when the signal is roughly stationary. Needless to say, these aspects are in tension. The variance of an estimate is large if it exhibits poor noise rejection. But equally in Kalman filtering, the covariance value, $\Sigma(k|k-1)$, in (3.17-3.21) above affects the estimator gain, $K(k)$, with high covariance equated with fast learning [27]. We plot in Figures 3.4 and 3.5 both the load estimates and their one-standard-deviation values to indicate the functioning of the method, where the $\theta(k)$ signal is used to adjust the learning aspects dynamically in the time-varying filter via $\mathcal{Q}(k)$.

Figure 3.4 displays the performance of the time-varying breaker-informed estimator driven by $y(k)$ and $\theta(k)$. We note that this estimator exhibits fast transient response at the switching times together with small variance load estimates during quiescent periods of nominal behavior. Also evident from this figure is the increase in estimator covariance at the breaker switching times, which is associated with rapid but noisy estimation of the new mean load value. The estimation returns to normal-rate learning after the transient period.

Figure 3.5 displays the corresponding performance for the breaker-uninformed estimator using the same $y(k)$ data and model as previously specified. The points to note are the time-invariant covariance values corresponding to a fixed separation of the red lines in the plot from the green. The transient response is much slower than for the breaker-informed case and the selection of parameter W_b has been made to balance the estimate variance in quiescent periods versus transient tracking. This compromise is apparent in the larger steady-state variance versus the time-varying informed case.

Although we have numerically demonstrated the estimation of load $l(k)$, estimates of the GT system state are a natural byproduct of the estimation framework constructed here. Hence, estimates of GT process variables are also available. Figures 3.6-3.8 present the resulting comparative estimates of the GT process variables N_{GP}, T_5, and P_2. The GT process variables depicted in solid blue lines represent the simulated values computed by the plant without measurement noise, i.e. the product $Cx(k)$. The

Figure 3.4: Total load deviation from nominal $l(k)$ (solid blue), its estimate from the breaker-informed estimator (green squares), and the estimate $\pm$one (computed) standard deviation of estimation error (solid red).

breaker-informed estimates are depicted as green boxes and the breaker uninformed estimates as magenta dots, both of which are informed by the GT output measurement signal $y(k)$ which is subject to measurement noise signal $v(k)$. The breaker-informed estimation provides significant tracking performance benefits in comparison with the breaker-uninformed method. The more rapid acquisition of an accurate GT state estimates with the new estimator is evident and would lead to process control improvements when incorporated into the feedback control signal either in a joint design or through the supplemental control input $u_s(k)$. The root mean square (RMS) errors of the θ-dependent and θ-independent estimates of load l and GT output signals $\{N_{GP}, T_5, P_2\}$ are compared in Table 3.1.
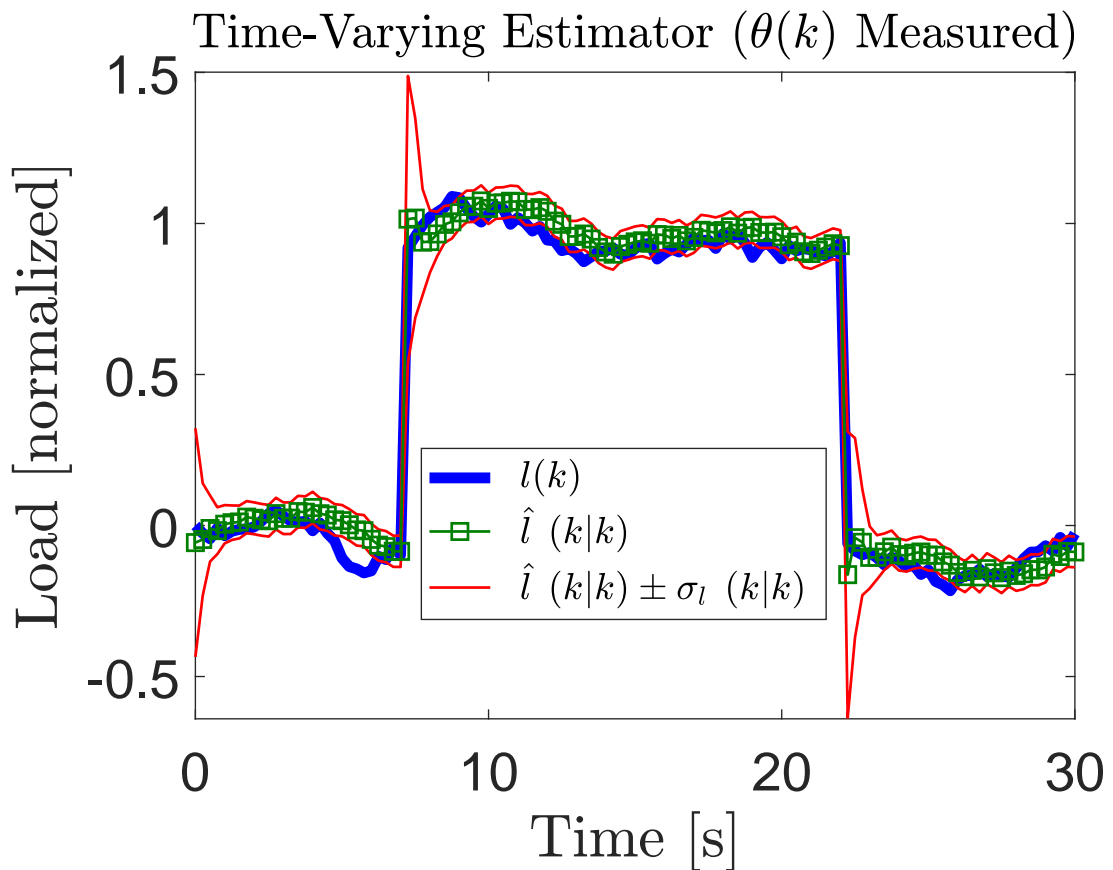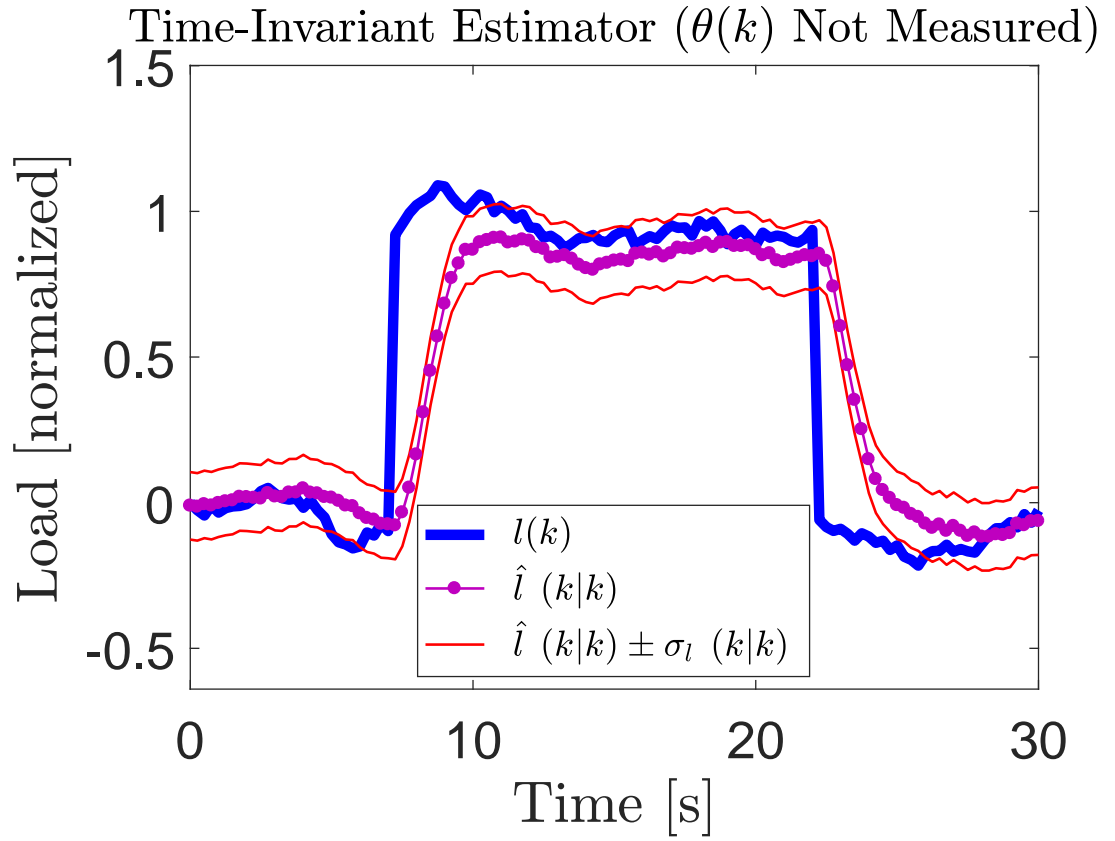
Figure 3.5: Total load variation from nominal, $l(k)$, (solid blue), its estimate from the breaker-uninformed estimator (magenta dots), and the estimate $\pm$one computed standard deviation of estimation error (solid red).

Table 3.1: Table of root mean square errors of θ-dependent and θ-independent estimates of load l and GT output signals $\{N_{GP}, T_5, P_2\}$.

Estimator Type	RMS Errors			
	l	N_{GP}	T_5	P_2
θ-dependent Error	0.0534	0.0448	0.0450	0.0258
θ-independent Error	0.2784	0.2701	0.2462	0.0918
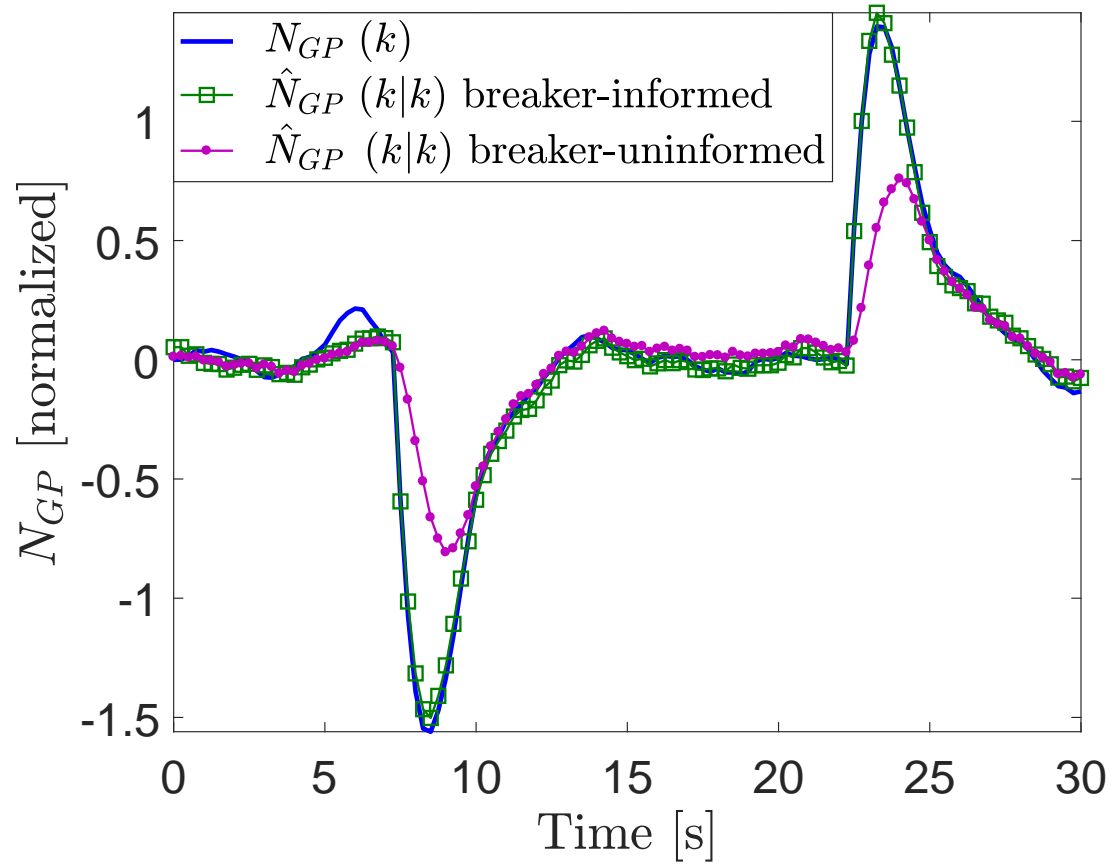
Figure 3.6: GT shaft speed, $N_{GP}(k)$, (solid blue), its breaker-informed estimate (green squares) and its breaker-uninformed estimate (magenta dots).
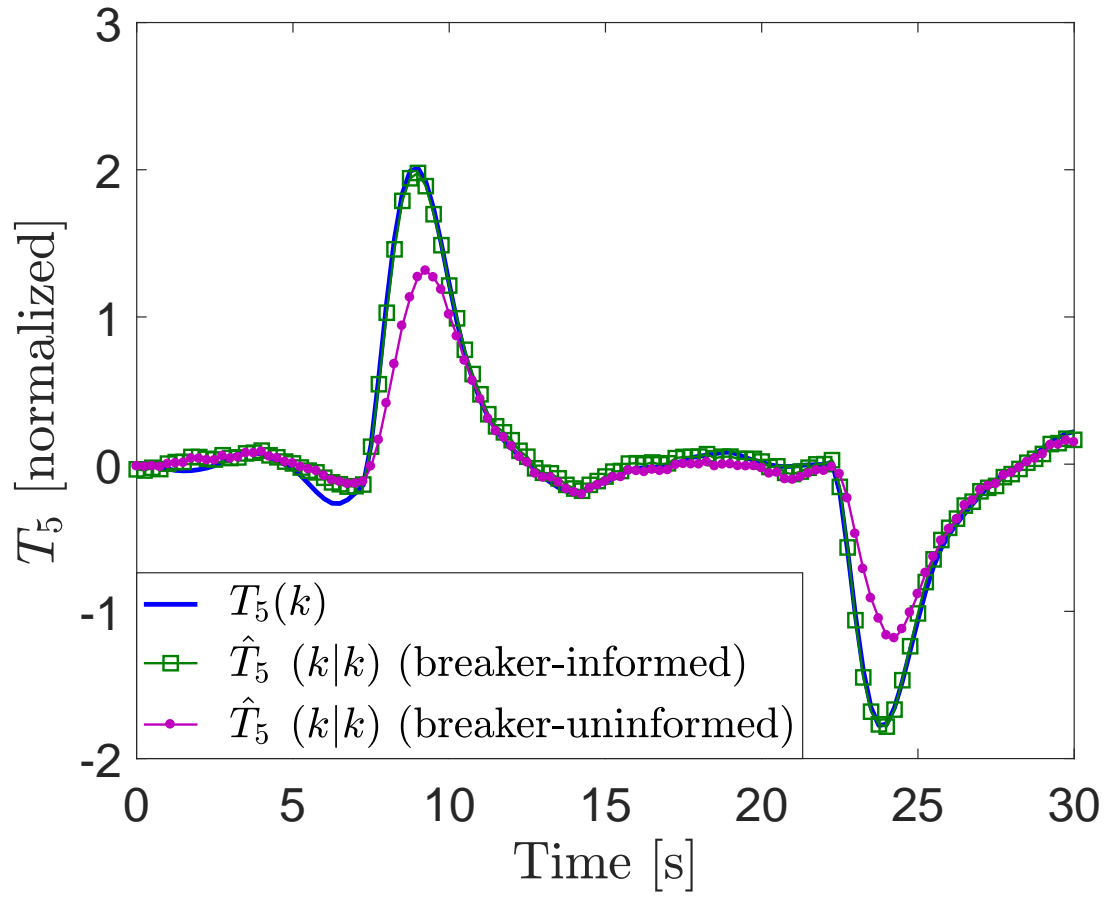
Figure 3.7: GT turbine 5$^{\text{th}}$ stage temperature, $T_5(k)$, (solid blue), its breaker-informed estimate (green squares) and its breaker-uninformed estimate (magenta dots).
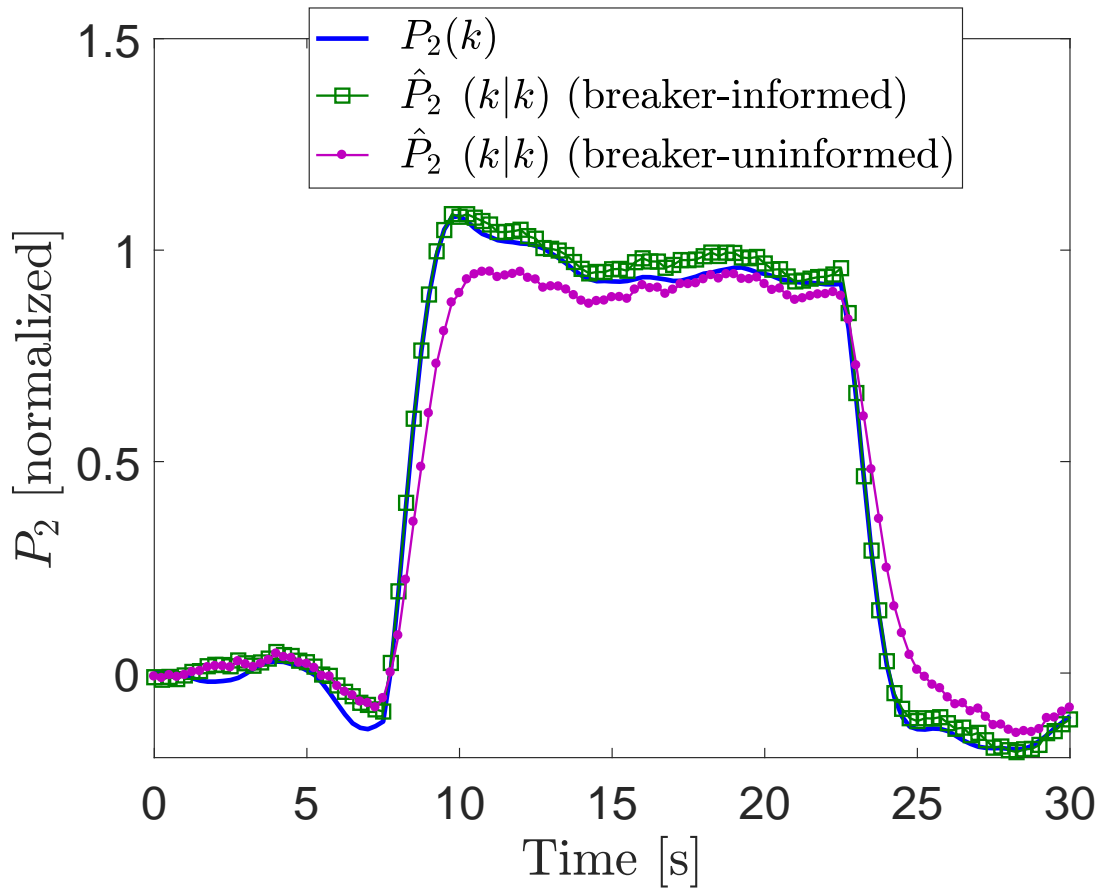
Figure 3.8: GT compressor discharge pressure, $P_2(k)$, (solid blue), its breaker-informed estimate (green squares) and its breaker-uninformed estimate (magenta dots).

3.7   Extension to Multiple Load Deviations

Thus far, we have constructed and demonstrated a modeling framework, which readily lends itself to the construction of a state estimator capable of incorporating a logic-valued breaker switching signal $\theta(k)$ and knowledge of the associated load switching statistics $\bar{\xi}$ and Ξ. We will now demonstrate how, with minimal modification, the proposed framework can be extended to incorporate N switching loads, each one connected to the microgrid via a separately instrumented breaker with breaker switching signals

$\theta^j(k), j = 1, 2, \ldots, N$. Relation (3.13) is augmented to become

$$\bar{\zeta}(k) = \sum_{j=1}^{N} \theta^j(k)\bar{\xi}^j, \quad \check{\zeta}(k) = \sum_{j=1}^{N} \theta^j(k) \left(\xi^j(k) - \bar{\xi}^j\right). \tag{3.25}$$

The bottom right variance term of $\mathcal{Q}(k)$ is altered to

$$\mathrm{var}\left(\check{\zeta}(k)\right) = \sum_{j=1}^{N} \left(\theta^j(k)\right)^2 \Xi^j, \tag{3.26}$$

where the set of data pairs $\left\{(\bar{\xi}^j, \Xi^j), j = 1, \ldots, N\right\}$ correspond to the statistics of the N individual switched loads.

3.8   Chapter Summary

We have developed a novel estimator for the incorporation of nonlinear, logic-based switching signals, together with switched load statistics into the load estimation of a GT power system. This admits greatly improved estimation performance, notably during transients following switching, at the expense of implementing a time-varying estimator. The estimator remains linear. Further, this formulation admits a very direct extension to more complicated classes of problems with multiple switching elements. The complexity of the estimator does not change, although the management of the signals is more complicated.

Future work will consider two aspects: disturbance rejection feedback control using this advanced estimator, and extension of the results to include scheduling for changes of the linearized models as ambient conditions and nominal loads vary. It is well understood that gas turbine engines in aeronautical applications are well modeled and controlled using linear methods scheduled for points in the flight envelope described by altitude, mach number and ambient temperature. In the power generation case, the envelope is more simply characterized.

3.9   Acknowledgments

This chapter is, in part, a reprint of "Improving Disturbance Compensation in Gas Turbines by Incorporating Event-Triggered Logic Signals From Switchgear," by Robert

H. Moroto, Robert R. Bitmead, and Chad M. Holcomb, to appear in the Proceedings of the *American Society of Mechanical Engineers (ASME) Turbo Expo 2017: Turbomachinery Technical Conference & Exposition*, to be held on June 26-30, 2017, Charlotte, North Carolina, United States of America.

Chapter 4

Gas Turbine Modeling for Control

4.1 Introduction

Advances in simulation software and engineering knowledge have driven development of gas turbine (GT) engine models which capture dynamic behavior with increasing levels of fidelity. When implemented in transient simulations, these high-fidelity models provide a flexible, rapid, and inexpensive platform for generating insightful engine data. However, such complex models are often undesirable for control design, where the simplest possible model which adequately characterizes the system dynamics is preferred, typically in the form of a linear model. GT models for control design are commonly obtained with model fitting techniques applied to data from closed-loop in situ engine experiments, which can be expensive, time-consuming, or impractical, and depends heavily upon the availability of an appropriate testing platform. However, in a recent work by [35], an open-loop GT engine model for control design was obtained using a high-fidelity GT engine model to generate the necessary data for model fitting, specifically by using system identification techniques.

System identification is an established method for obtaining GT models, such as in [36], [37], [38], and [39]. Typically, data is generated from in situ experiments on a physical test engine. Conducting in situ experiments on an engine in the field may not be feasible due to the potential revenue loss to the customer caused by a lack of availability. An alternative is to perform in situ engine experiments in a dedicated testing facility. In order to ensure safe operation of the engine these experiments are performed in closed-

loop with a controller. Traditional white noise excitation signals can degrade the health of components. Thus, alternative excitation signals, such as multisines, are commonly used to excite the engine in the appropriate frequency band and minimize the so-called crest factor [40]. Other consideration related to in situ testing include synchronization of data, sensor noise, unmeasurable signals, and component failures must be taken into consideration as well.

Although in situ experiments with a physical GT engine have numerous associated operational, time, cost, safety, and data management requirements, experiments using transient simulations of a high-fidelity model (of sufficient quality) can circumvent most of these issues. Transient simulations experiments with a high-fidelity GT engine model are inherently fast, cheap, and can be pushed to the limits of realistically safe operation, allowing a wider selection of excitation signals; recorded signal data does not have measurement noise and is automatically synchronized with the simulation clock; signals which are not available during in situ experiments may be available; the internal structure of the model may offer structural insights which can be incorporated into a linear model for control design; and reconfiguration of the experimental setup is simple.

Proposed Approach

In this work, an open-loop linear model of a 5 MW dry low emissions GT engine, for power generation applications, is constructed. A *high-fidelity gas turbine* (HFGT) model of the engine, in closed-loop configuration with a high-fidelity model of the existing controller, is available for use in transient simulations in Simulink. The high-fidelity model is used to generate data for closed-loop system identification, which circumvents the cost, time, and numerous requirements of in situ experiments and allows for flexible and varied experimental configurations, including closed-loop validation experiments used to verify the constructed engine model, which takes the form of a *linear time-invariant gas turbine* (LTI GT) model. Additionally, the internal subsystem structure of the HFGT model is leveraged to divide the constructed linear engine model into three major subsystems, and modeling decisions can be applied independently to each subsystem. The three engine subsystems are denoted as follows:

- the *Fuel Subsystem*, which is excluded from modeling due to the availability of

fuel flow during online engine operation;

- the *Rotor System*, for which a linear model is obtained via a steady state approximation of its high-fidelity dynamics; and

- the *Remainder Subsystem*, which includes all subsystem blocks other than the Fuel Subsystem, and which can be obtained by way of system identification on closed-loop data from the HFGT model.

The major engine subsystems are illustrated in Figure 4.6, and are discussed in detail in the body of this paper.

The LTI GT engine model is constructed by combining the identified Remainder Subsystem model with the linear Rotor Subsystem model. Since the constructed engine model uses fuel flow directly as an input signal, instead of valve commands, then any Fuel Subsystem can be used for control design in a modularly interchangeable fashion. Likewise, the linear model of the Rotor Subsystem preserves the physical significance of the model parameters from the high-fidelity Rotor Subsystem model, which allows the linear rotor model to characterize a wide range of rotors in control design.

The LTI GT model is validated in a closed-loop transient simulation while regulated by the high-fidelity model of the existing controller block. The output signals are compared to those generated by the HFGT model under comparable circumstances.

Organization of Remaining Text

The remainder of the text is organized as follows: Section 4.2 contains nomenclature used throughout the text and a table of relevant GT signals; Section 4.3 contains brief descriptions of closed-loop system identification and and common approaches; Section 4.4 contains an overview of GT operation and the HFGT engine model used to generate data for system identification; Section 4.5 details the approach used to leverage the internal subsystem structure of the HFGT model in the construction of the LTI GT model, and models for the Remainder Subsystem and the Rotor Subsystem are obtained; Section 4.6 discusses the closed-loop transient simulation experiment used to validate the constructed LTI GT engine model against the closed-loop response of the HFGT

model in a comparable transient simulation experiments; and Section 4.7 contains a summary of this work.

4.2 Nomenclature

GT   Gas turbine

HFGT   High-fidelity gas turbine (model for generating data)

LTI GT   Linear time-invariant gas turbine (model constructed in this work)

LTI   Linear time-invariant (system)

ID   Identification (i.e. system identification)

PLC   programmable logic controller

SDNG   San Diego natural gas

Wobbe   Wobbe index of the fuel

t continuous-time ($t \in \mathbb{R}, \text{ with } t \geq 0$)

k discrete-time index ($k \in \mathbb{N}, \text{ with } k \geq 0, \text{ and } t = t_s \cdot k$)

t_s sample period (of signal data recorded from transient simulations)

Table 4.1: Table of gas turbine variables and their physical significance.

GT Variable	Physical Significance
KW	Load (generator, $KW = \overline{KW} + dKW$)
$\overline{KW}$	Nominal operating load (generator)
KW_{rated}	Maximum rated load (generator)
NGP	Rotational shaft speed (in percent)
$T5$	Temperature at GT Stage 5 (power turbine blades)
$P2$	Pressure at GT Stage 2 (compressor outlet)
$P3$	Pressure at GT Stage 3 (combustion chamber)
$T3$	Temperature at GT Stage 3 (combustion chamber)
$PFMM$	Pressure in main fuel manifold
$PFMP$	Pressure in pilot fuel manifold
BVD	GT bleed valve command (fuel control signal)
WFI	GT fuel injector flow rate (fuel control signal)
GVC	GT guide vane command (air control signal)
MVC	GT main valve command (fuel control signal)
PVC	GT pilot valve command (fuel control signal)
PWR	Lossless net engine power ($HPT - HPC$)
HPT	power from power turbine blades (no rotor losses considered)
HPC	power consumed by compressor (no rotor losses considered)
dKW	load disturbance (perturbation from nominal)
$dWFI$	fuel flow excitation (for system identification)
$dGVC$	guide vane command excitation (for system identification)

4.3   Closed-loop System Identification

This section contains an overview of system identification techniques using data generated from closed-loop experiments. In general, system identification involves using input-output signal data to fit a model for a dynamic system of interest. Models can be identified with various intended uses, such as simulation, prediction, or control

design. Models for control design capture the dynamic behavior of the system in a frequency passband of interest, typically within plus or minus a decade of the crossover frequency. It is desired that models for control design are as simple as possible, for example in the sense of model order, to ensure the feasibility of controllers and estimators designed with that model.

In many practical engineering applications, implementation of open-loop experiments can be prohibitively costly. This is particularly germane to industrial systems, which are often intended for continuous operation, such as gas turbine engines used for power generation. A loss of availability for such systems can result in significant opportunity cost for the customer. The system of interest may also have dynamics or operating constraints (due to safety, component health, or other factors) which require closed-loop operation, even while conducting experiments in a dedicated testbed environment. Additionally, it has been shown by [41] that closed-loop system identification can yield superior models for control design than system identification using data generated from open-loop experiments. Hence, system identification experiments conducted in closed-loop can be used to ensure availability and can produce superior models.

In a general system identification setup, we consider the discrete-time linear time-invariant system

$$y(k) = G(z)u(k) + v(k),$$

where G denotes the input-output process dynamics, u is the input signal, y is the measured output signal, and v is an additive exogenous noise signal defined by $v(k) = H(z)e(k)$, where H is a linear filter and e is zero mean independent white noise. The data $\begin{bmatrix} y^T & u^T \end{bmatrix}^T$, used to fit models for G and H, must be obtained by experiments on the process. If input u and exogenous noise e are uncorrelated, then the data is said be *open-loop identification data* and was generated by an *open-loop identification experiment*, and standard open-loop identification methods can be applied. If input u and exogenous noise e are correlated, then the data is said be *closed-loop identification data* and was generated by a *closed-loop identification experiment*, allowing closed-loop identification methods must be used.

Block diagrams illustrating both types of system configurations are shown in Figure 4.1, where the closed-loop system is regulated by a controller C and measured ex-

ogenous reference signal r. The controller C acts like a constraint which limits the behavior of the signal it produces. During a closed-loop identification experiment, the signal r functions not only as a reference signal, but can be used to inject excitation into the system. Careful design of r is required to produce informative experimental data.
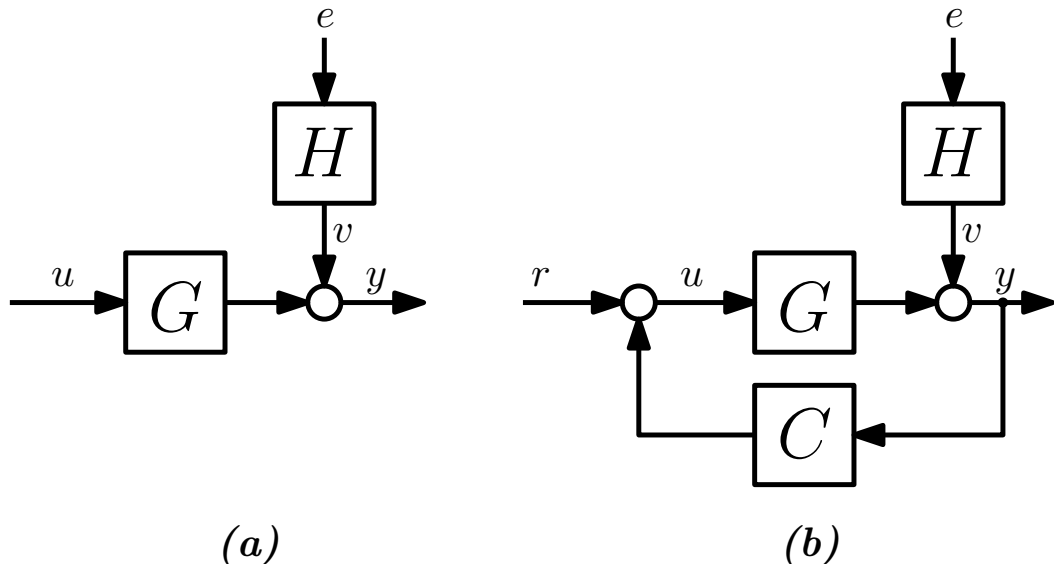

Figure 4.1: Identification experimental setup for process G and noise shaping filter H with data generated in either open-loop (a) or closed-loop with a controller C and reference signal r (b).

Closed-loop identification experiments are often necessary in practical applications where conducting offline open-loop experiments are unsafe, such as when the process is open-loop unstable; impractical, such as when the possibility of damaging components is increased in open-loop operation; or expensive. In particular, the high-fidelity gas turbine model leveraged in this work must be operated in closed-loop due to the bounded nature of the lookup tables within the model, where open-loop operation has a tendency to drive the system 'off the map', i.e. beyond the range of the lookup tables.

Several common closed-loop identification methods, and their advantages and disadvantages, are briefly described in the remainder of Section 4.3.

4.3.1 Direct Approach

The *direct approach* to closed-loop system identification is the application of open-loop system identification methods directly to closed-loop identification data. The advantages of this method include the fact that knowledge of the regulator or the character of the feedback is not required, a wide variety of open-loop identification algorithms can be used, and unstable open-loop systems can be handled provided the closed-loop system is stable and the predictor is stable, which can be guaranteed with some technical conditions (c.f. [42]). However, due to the well-known trade-off between bias error and variance in model fitting, a good model for the noise filter H is required for the direct approach to be successful. For more information, see [24].

4.3.2 Indirect Approach

In the *indirect approach* to closed-loop system identification, the closed-loop system model is identified from measured signals y and r, and the open-loop process model is obtained from knowledge of the (usually linear) controller. An advantage comes from a special case of this approach called the dual Youla parameterization method, which allows you to find all open-loop process models stabilized by the controller C, as explained in [43]. A disadvantage of this approach is that the controller C must be known, and any nonlinearities in the controller significantly complicate the approach.

4.3.3 Two-Stage and Projection Approach

The two-stage approach of closed-loop system identification involves, as the name suggests, two stages. In the first stage, a model G_{ur} from the measured exogenous signal r to the controlled input signal u is identified, given by

$$u(k) = \hat{G}_{ur}(z)r(k) + \hat{H}_{ur}e'(k),$$

where $e'(k)$ zero-mean independent white noise. A 'noise-free' version of the input signal is then generated by $\hat{u}(k) = \hat{G}_{ur}(z)r(k)$. In the second stage, a model is identified from the data $z = \begin{bmatrix} \hat{u}^T & y^T \end{bmatrix}^T$. This method was introduced in [44] for obtaining transfer functions with prediction error techniques. A variant of this approach, introduced by

[45], uses a non-causal FIR model to fit the first stage model from r to u obtained using least squares, which can be done with a sufficient quantity of FIR parameters so that any correlation between r and u can be ignored, and the difference $u - \hat{u}$ is be uncorrelated with sequence r. An advantage of this variant is that the asymptotic convergence results hold regardless of the true relationship between r and u, even if this relationship nonlinear, or if the controller K is nonlinear.

4.4   Gas Turbine Operation and High-Fidelity Models

This section provides an overview of basic gas turbine operating principles and introduces the high-fidelity gas turbine (HFGT) Simulink model, knowledge of which is leveraged to construct linear gas turbine models suitable for control design.

4.4.1   Gas Turbines for Power Generation Overview

A gas turbine (GT) engine is comprised of several basic components, a multi-stage axial compressor, which compresses ambient air to a suitable pressure; a combustion chamber, where fuel and the high pressure air from the compressor outlet are mixed and combusted; and a multi-stage axial power turbine, which receives the energy from the expanding byproducts of combustion. A fraction of the energy transmitted to the power turbine blades sustains the rotational motion of the compressor shaft, while the majority of the remaining energy is converted into mechanical work for use by the driven equipment output. A simplified diagram of gas turbine operation is illustrated in the diagram in Figure 4.2.
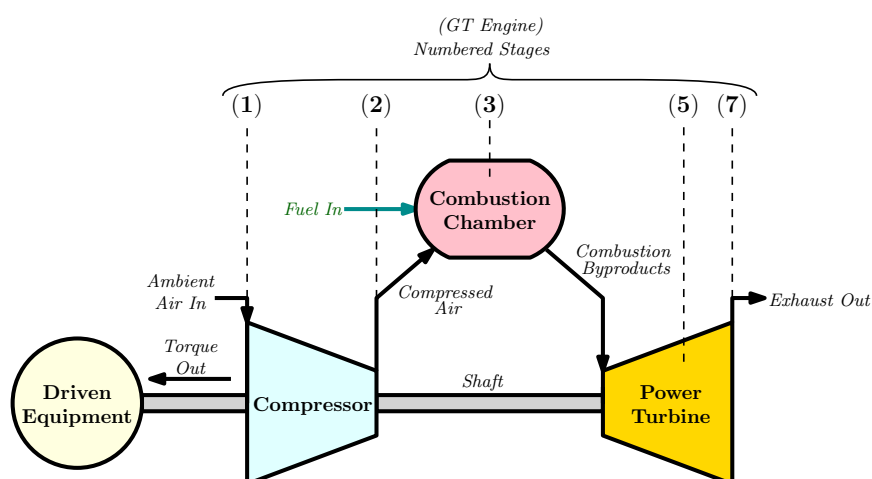
Figure 4.2: Simplified diagram of gas turbine operation.

Operating conditions vary throughout the engine. It is a common convention to label the principal stages of the engine with a number, which is used to identify the location the values of physical quantities, such as pressures and temperatures, at that position in the engine. The principal stages of engine operation are traditionally labeled as in shown Figure 4.2, where each numbered stage is associated with the following engine component stations:

Stage (1) corresponds to the compressor inlet, where ambient air enters the compressor;

Stage (2) corresponds to the compressor outlet, where compressed air exits the compressor;

Stage (3) corresponds to the combustion chamber, where fuel is injected, mixed with the compressed air of Stage 2, and combusted;

Stage (5) corresponds to the power turbine blades, where the high-velocity byproducts of combustion transfer energy to the power turbine blades to generate mechanical output work and sustain the rotation of the engine shaft; and

Stage (7) corresponds to the exhaust section, where the waste fumes are ejected from the engine.

In this work, we consider a single-shaft dry low emission $5\ MW$ Solar Turbines Taurus$^{\text{TM}}$ 60 (T60) GT engine used for power generation. The engine is coupled with a three-phase electrical generator which supplies power at a desired frequency and voltage. A diagram of the engine and generator is shown in Figure 4.3.
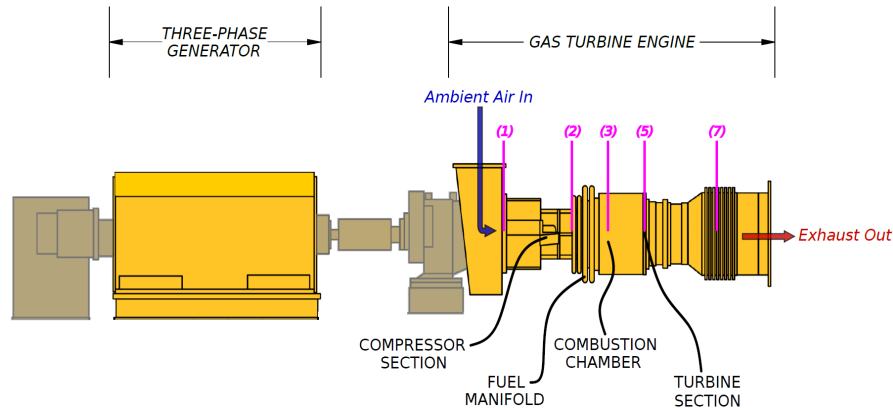

Figure 4.3: Solar Turbines Taurus$^{\text{TM}}$ 60 gas turbine engine coupled with a three-phase electrical generator. Illustration adapted from [1]. GT engine stages are numbered in magenta.

A detailed block diagram of the engine, generator, controller, and all relevant signals, is illustrated in Figure 4.4. The physical of significance of the relevant signals is given in Table 4.1. In this work, the controller which regulates the engine operation is termed the *Existing Controller*, which produces control signals MVC, the main valve command signal; PVC, the pilot valve command signal; GVC the command signal for the variable inlet guide vanes; and BVD, the bleed valve command signal. Signals MVC and PVC modulate the fuel flow rate WFI into the combustion chamber through the fuel injectors. Air flow is primarily regulated by GVC and to a lesser extent by BVD. For this particular engine model, the effect of BVD is neglected and its existing schedule is not considered in potential control designs from models constructed here. The most significant regulated output signals are NGP and $T5$, which must track their respective reference signals to ensure performance and safety requirements of operation. However, transients in the load KW act as a disturbance signal that causes NGP and $T5$ to deviate from their reference values, and the controller must reject the effect of changes in KW. More information about gas turbine operation can be found in [46], [47].
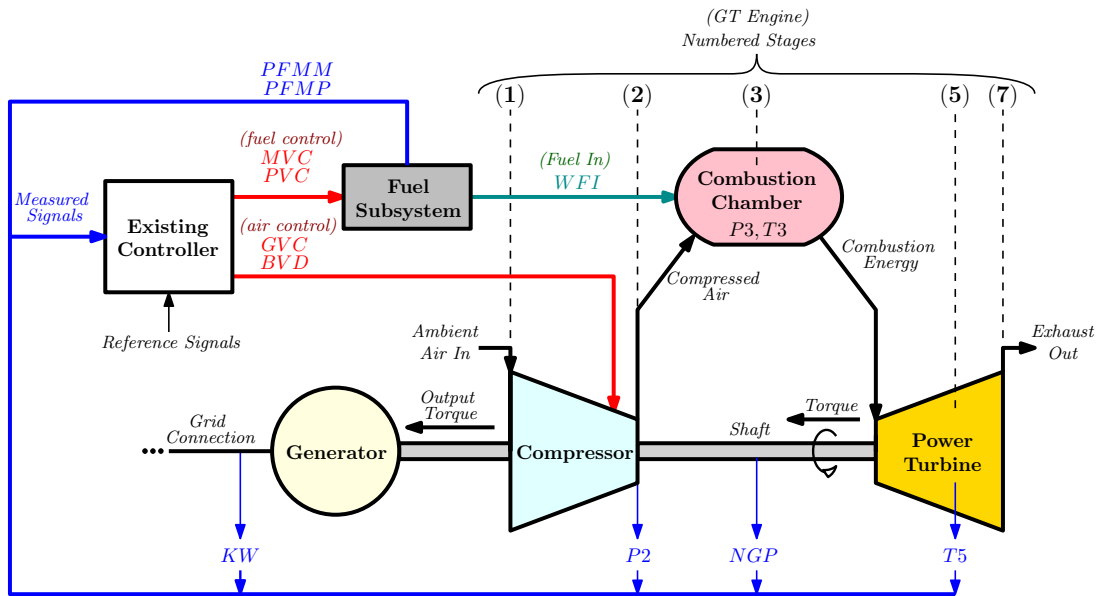
Figure 4.4: Detailed block diagram of GT engine, Existing Controller, and generator in closed-loop configuration.

4.4.2 High-Fidelity Gas Turbine Model

The high-fidelity model used to generate transient simulation data in this work was implemented in Simulink and its block diagram is shown in Figure 4.5. High-fidelity representations of the Taurus™ 60 engine and the Existing Controller were placed in a closed-loop configuration. In this work, the model of the engine is termed the *high-fidelity gas turbine* (HFGT) model. The HFGT model is comprised of internal, interconnected, modular subsystem blocks which represent the components and signals depicted in Figure 4.4. The HFGT model was validated against transient data from in situ experiments on a physical engine which were conducted in a highly instrumented dedicated test facility.
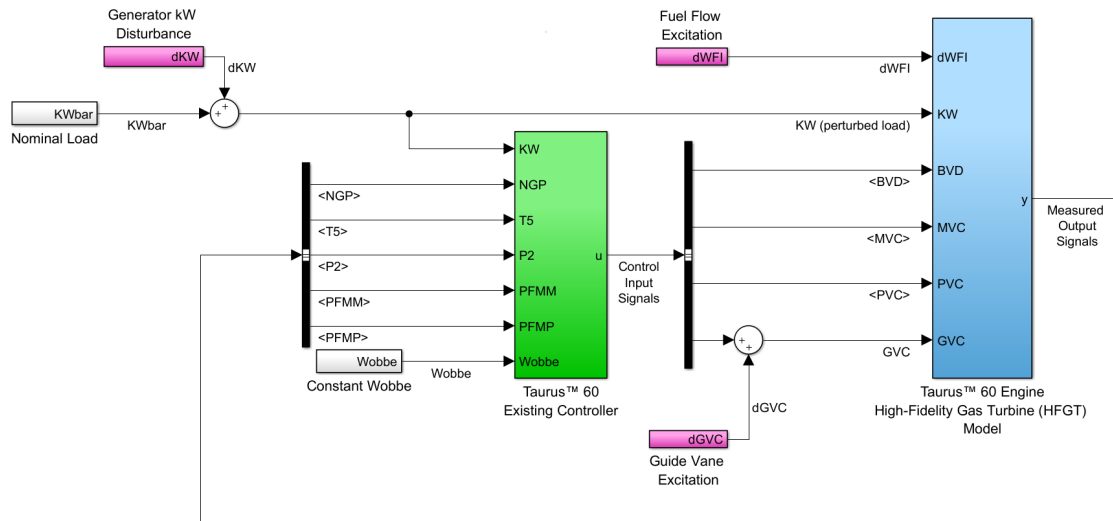
Figure 4.5: Simulink block diagram of the high-fidelity gas turbine (HFGT) model of the Taurus™ 60 (T60) engine in closed-loop configuration with the Existing Controller block.

Signal KW is an exogenous disturbance signal which is the sum of a nominal operating load $\overline{KW}$ and an additive perturbation load dKW. The signals $dWFI$ and $dGVC$ are exogenous excitation signals that were used for system identification. Fuel properties (such as Wobbe index, specific gravity, fuel temperature, etc.) are assumed to have fixed values associated with San Diego natural gas (SDNG). The generator is excluded from the modeling process.

The Existing Controller block generates signals $\{BVD, MVC, PVC, GVC\}$. Although the goal is to obtain an open-loop engine model suitable for control design, the Existing Controller block is needed for transient simulations due to the limits of the look-up tables which are used within the HFGT model. Open-loop simulations with only the engine will cause the system to operate on the map boundaries which can potentially crash the simulation. Thus, closed-loop operation is required for generating useful data. Additionally, a newly designed controller should not affect the steady state operation of the engine, only the transient performance. Hence, the Existing Controller block is a desirable regulator for closed-loop experiments.

The internal subsystem blocks within the HFGT model can be grouped into three relevant major pieces, a grouping that provided key insight into the method used to construct a model suitable for control design. Namely, we consider the *Fuel Subsystem*,

which contains a high-fidelity model of the valve and fuel injector dynamics; the *Rotor Subsystem*, which contains a high-fidelity model of the rotor dynamics and which calculates NGP; and the rest of the subsystems are grouped into a single block called the *Remainder Subsystem*. A block diagram illustrating the internal subsystem structure of the HFGT model is illustrated in Figure 4.6.
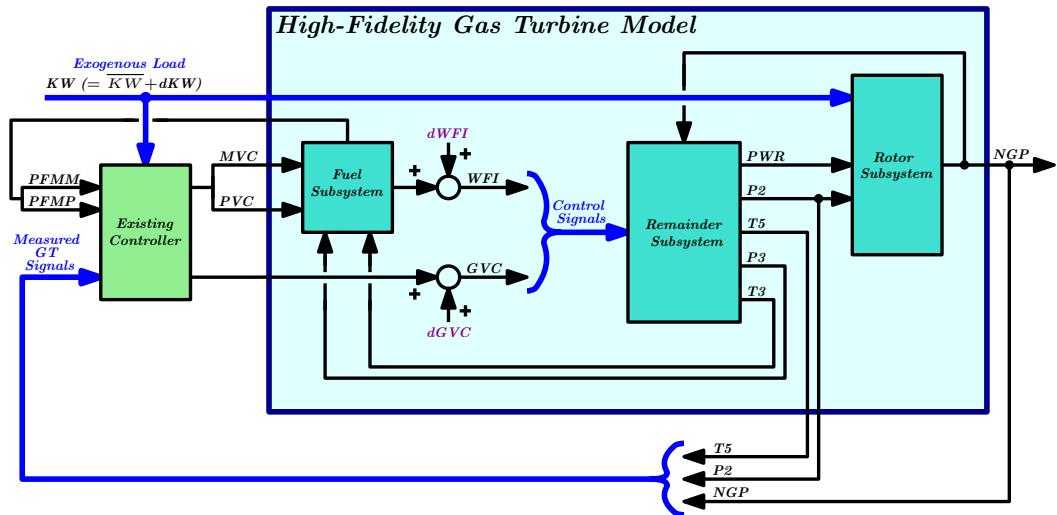

Figure 4.6: Structural subsystem partition of the HFGT model in closed-loop configuration with the existing controller block.

4.5   Obtaining a GT Model for Control Design

In this section, a control-design-oriented model is constructed for a single-shaft, dry low emissions Taurus[TM] 60 gas turbine engine coupled with a three-phase electrical generator, as described in Section 4.4.1. The high-fidelity HFGT engine model and Existing Controller model introduced in Section 4.4.2 are available for use in closed-loop transient simulations implemented using Simulink.

The constructed model consists of a single linear time-invariant state-space realization for the GT engine, the *LTI GT model*. The LTI GT model is valid near a nominal operating point characterized by a fixed nominal load value $KW = \overline{KW}$. However, in practice, the approach can be repeated at different nominal load values to yield a family of LTI GT models which are amenable to control design and collectively characterize

the engine dynamics over a practical range of KW values.

The remainder of Section 4.5 describes the modeling decisions used to construct the LTI GT model. Discussion of how the internal subsystem structure of the HFGT model was leveraged in the construction of the LTI GT model is discussed in Section 4.5.1. The system identification design decision used to obtain a linear model of the Remainder Subsystem is discussed in Section 4.5.2. Discussion of how a linear model of the Rotor Subsystem was obtained from a steady state approximation of the high-fidelity dynamics of that subsystem in given in Section 4.5.3. The formulation of the LTI GT model as an augmented model which combines the identified linear model of the Remainder Subsystem and the approximated linear model of the Rotor Subsystem is detailed in Section 4.5.4. Following Section 4.5, a validation of the LTI GT engine model in closed-loop transient simulations is demonstrated in Section 4.6.

4.5.1 Exploiting Internal Structure of the HFGT Model

The internal structure of the LTI GT engine model was selected to mirror that of the HFGT engine model, as shown in Figure 4.6. A block diagram of the selected internal subsystem structure of the LTI GT model is illustrated in Figure 4.7, with the exception of the Fuel Subsystem, which was excluded from the LTI GT model.
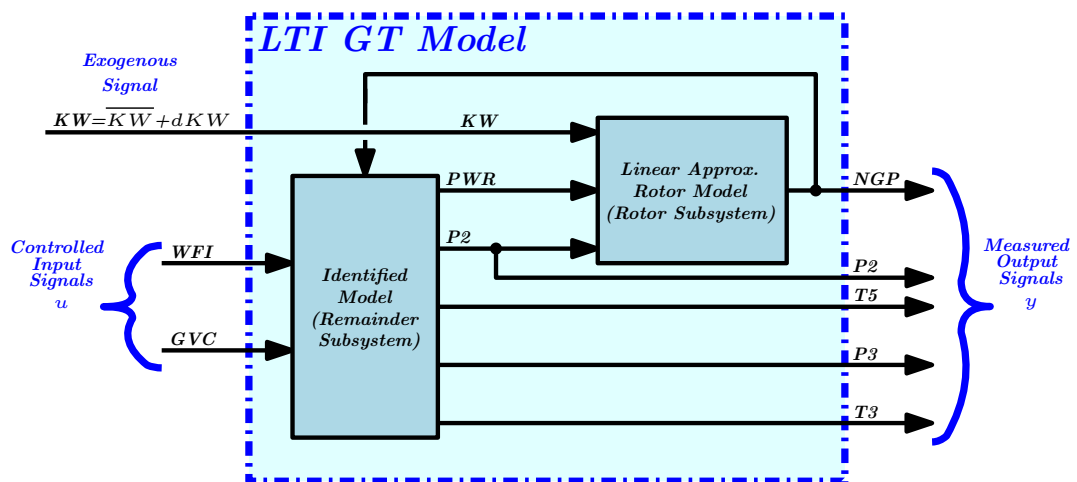

Figure 4.7: Block diagram of the selected internal structure of the LTI GT model.

The LTI GT model was constructed as an augmented model comprised of two interconnected linear time-invariant models, one model corresponding to the Remainder Subsystem and the other model corresponding to the Rotor Subsystem. The linear model of the Remainder Subsystem was obtained by the direct approach to closed-loop system identification and the linear model of the Rotor Subsystem was obtained by a linear approximation of the high-fidelity rotor dynamics.

The independent modeling of the Remainder Subsystem and Rotor Subsystem was enabled by the fact that the HFGT model provides access to signals which are unavailable during in situ experiments with a physical engine. Specifically the lossless net engine power PWR. 'Pulling out' the rotor dynamics from the identified portion of the model reduced the model order necessary to capture the identified dynamics.

Fuel flow rate through the injectors WFI was used as a controlled input signal for the LTI GT model instead of valve commands MVC and PVC, which not only reduced the number of controlled input signals, but also also excluded the Fuel Subsystem from the modeling process. The exclusion of the Fuel Subsystem ensures that the LTI GT model can be paired with any valve models during control design. Signal WFI is calculated in the PLC during online engine operation and all signals driving the Fuel Subsystem are known, including $P3$ and $T3$ which are measured outputs of the identified model for the Remainder Subsystem. Thus, the selection of WFI as a controlled input is appropriate due to its availability during real-time engine operation.

Since the LTI GT model was constructed so that the interconnections of its internal subsystem models mirrors the subsystem interconnections within the HFGT model, the LTI GT model can be validated in closed-loop transient experiments with the Existing Controller block and the Fuel Subsystem block.

4.5.2   Remainder Subsystem Model: Identification

A linear time-invariant model for the Remainder Subsystem was obtained from system identification using closed-loop transient simulation data. In this section, the system identification design points and results are presented. The nominal operating point of the identified model, around which the model is valid, was selected to be 75% of the total rated load of the GT. That is, $\overline{KW} = (0.75)KW_{rated}$, where KW_{rated} is the 100%

rated load for the Taurus$^{\text{TM}}$ 60 engine.

The transient simulation used to generate data for system identification, termed here as the *identification experiment*, was implemented in Simulink as shown in the block diagram in Figure 4.5, with the HFGT engine model in closed-loop with the Existing Controller block. The bounds of the lookup tables within the HFGT engine model necessitated the use of closed-loop transient simulations to generate experimental data for system identification. The simulation was solved with a variable-step solver.

The Wobbe index of the fuel was fixed to correspond with the composition of San Diego natural gas (SDNG), ambient conditions were chosen as an ISO standard day. The sample period was selected to be $t_s = 0.090$ s, which is three times faster than the *scan time* of the PLC used to control the physical engine, i.e. the duration of a single iteration of the software recursion. Due to the momentum of the gas turbine at operational speeds, the low frequency behavior of the system dynamics was of primary interest. The bandwidth of interest spanned a frequency range of approximately 0 Hz to 1-2 Hz, which was well within the Nyquist frequency of the sample period. Thus, the selected sample period effectively oversampled the system dynamics, reducing potential anti-aliasing and improving resolution.

Experiment Design

In the design of the closed-loop transient simulation used to generate data for identification of a linear model of the Remainder Subsystem, the HFGT model was affected by three exogenous signals, dKW, $dWFI$, and $dGVC$, which required careful design in order to yield sufficiently informative data. The Simulink blocks constructed to generate the exogenous signals are represented by the magenta colored blocks depicted in Figure 4.5.

The exogenous signals were injected into the closed-loop system as illustrated in Figure 4.6. Exogenous signal dKW functioned as a disturbance affecting the engine by additively perturbing the total load KW around the nominal load $\overline{KW}$, i.e. the total exogenous load signal KW was defined by

$$KW(t) = \overline{KW}(t) + dKW(t).$$

The signals $dWFI$ and $dGVC$ were injected as additive excitations to the controlled input signals generated by the Existing Controller block. The sum of each injected signal with its associated controller-generated counterpart formed the control signals which impinged upon the engine, fuel flow WFI and guide vane command GVC respectively.

Exogenous signals, dKW, $dWFI$, and $dGVC$ were selected as independent, identically distributed, zero-mean white noise signals over respective uniform distributions. Realizations of the exogenous signals were generated in Simulink using the built-in 'Uniform Random Number' block, which generates a uniformly distributed random signal value at a fixed 'sample time'. For the realization of disturbance signal dKW, a sample time of 5 s was selected, which is faster than the the fluctuations used during typical load acceptance tests of an engine. For the realizations of both $dWFI$ and $dGVC$, a sample time of 0.09 s was selected, which was equal to the sample period t_s, but filtering was applied to these signals during the transient experiments, prior to their impingement upon the engine.
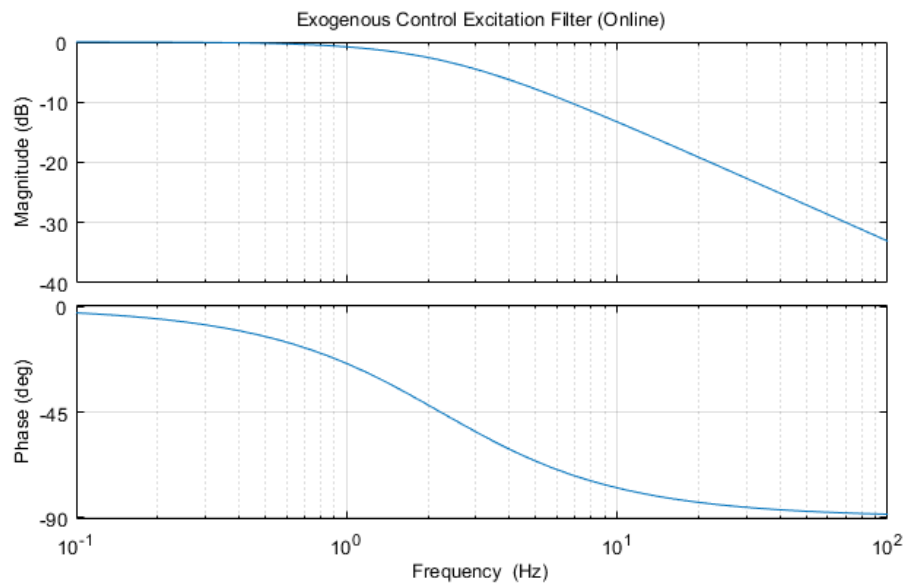

Figure 4.8: Bode plot of the 4$^{\text{th}}$-order Butterworth lowpass filter used in the identification experiment to shape the frequency content of excitation signals $dWFI$ and $dGVC$.

The control excitation signals, $dWFI$ and $dGVC$, were independently filtered with a 4$^{\text{th}}$-order Butterworth lowpass filter possessing a -3 dB frequency at 1.25 Hz. A Bode

plot of the excitation signal filter is given in Figure 4.8.

The normalized single-sided amplitude spectra of the exogenous signals. are plotted in Figure 4.10. The slower sample time of dKW focused the power of the disturbance at lower frequencies, which is realistic due to the intermittent nature of load switching in power generation applications. The filtering caused the power of excitation signals $dWFI$ and $dGVC$ to be focused in the 0-1 Hz frequency range, as desired. The exogenous signals were persistently exciting up to order 50, which insured a model could be identified for the gas turbine engine, which are typically of much lower order.
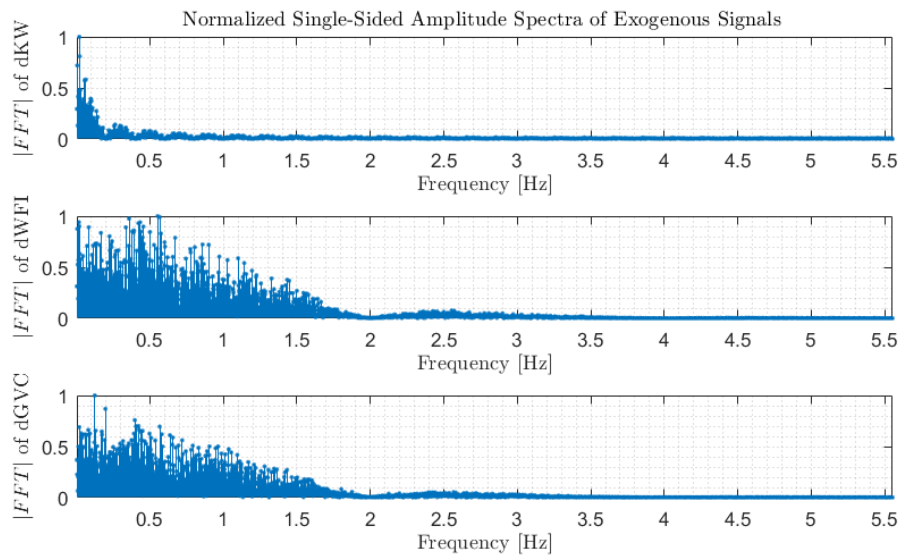
Figure 4.9: Normalized, single-sided amplitude spectra of exogenous signals used in the experiment to generate data for system identification.

The exogenous signals used in the identification experiment are plotted in the time domain in Figure 4.10, where dKW, $dWFI$, and $dGVC$ have been scaled to a percentage of KW_{rated}, $max\,|WFI|$, and $max\,|GVC|$ respectively.
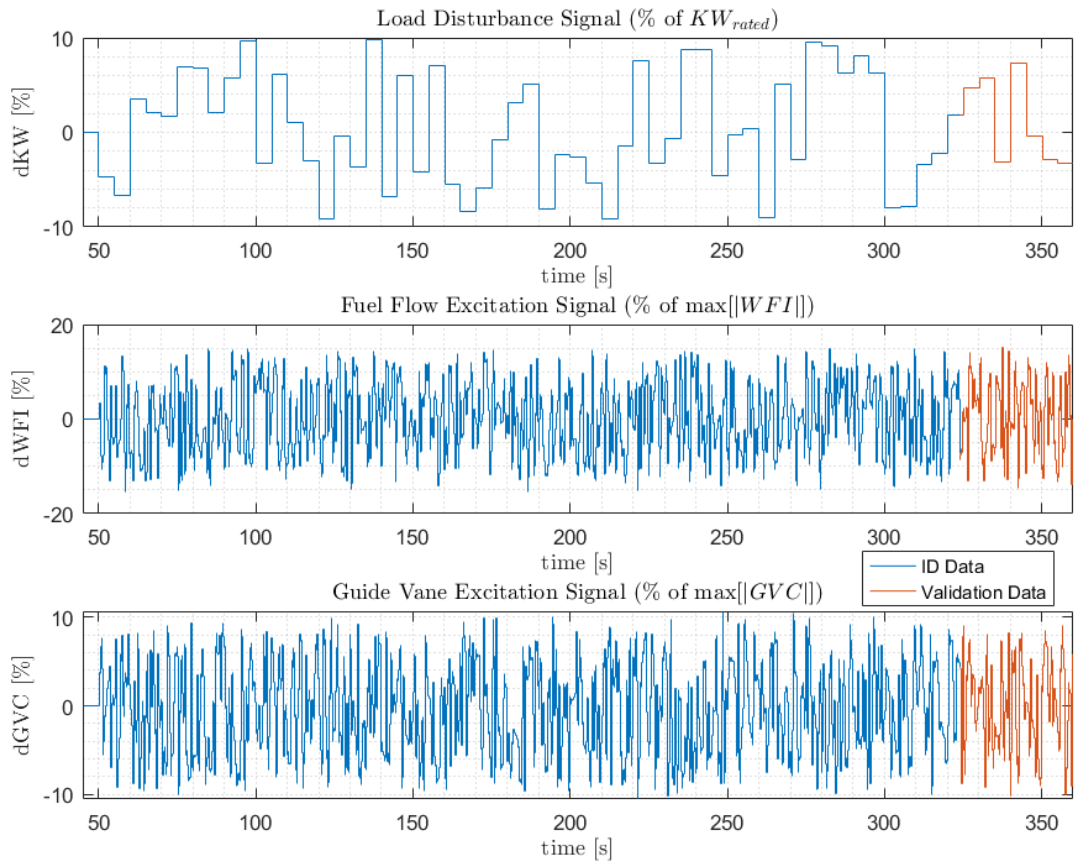
Figure 4.10: Exogenous signals applied to the high-fidelity engine model in experiments used for system identification of a linear model for the Remainder Subsystem.

The identification experiment had a total duration of 351.91 s and a total of 4000 data points were recorded for each signal. In order to provide sufficient time for the closed-loop high-fidelity system to nullify the effects of the initial conditions, the exogenous signals were set to zero values until time $t = 50$ s of the experiment, after which they behaved as previously described.

For each recorded signal, a subset of the data consisting of 3100 data points–with a time stamp values of $45\ s \leq t \leq 323.91\ s$–were used for identification of the linear model (colored blue in Figure 4.10), denoted here as the *identification data subset*, and the remaining 400 data points–with a time stamp values of $324\ s < t \leq 351.91\ s$–was used for open-loop validation of the identified model (colored red in Figure 4.10), denoted here as the *open-loop validation data subset*. The exogenous signals were given zero-order holds, with sample times equal to t_s, in order to satisfy typical system iden-

tification assumptions, and to synchronize the recorded data.

Identification Experiment Results

The normalized time domain plots of the measured output signals of the Remainder Subsystem are shown in Figures 4.11-4.15. For each signal, the subset of data used for identifying the linear model is colored blue and the subset of data used for open-loop validation of the model is colored red. The rotational shaft speed NGP, which is an input signal of the Remainder Subsystem, is plotted in Figure 4.16.
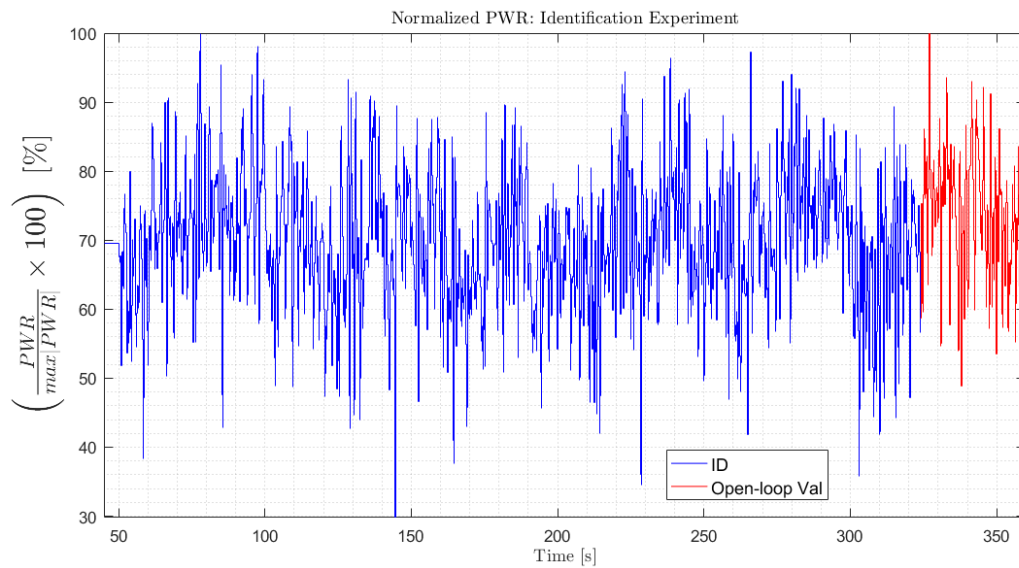

Figure 4.11: Normalized time-domain PWR signal generated by the HFGT model in the identification experiment.
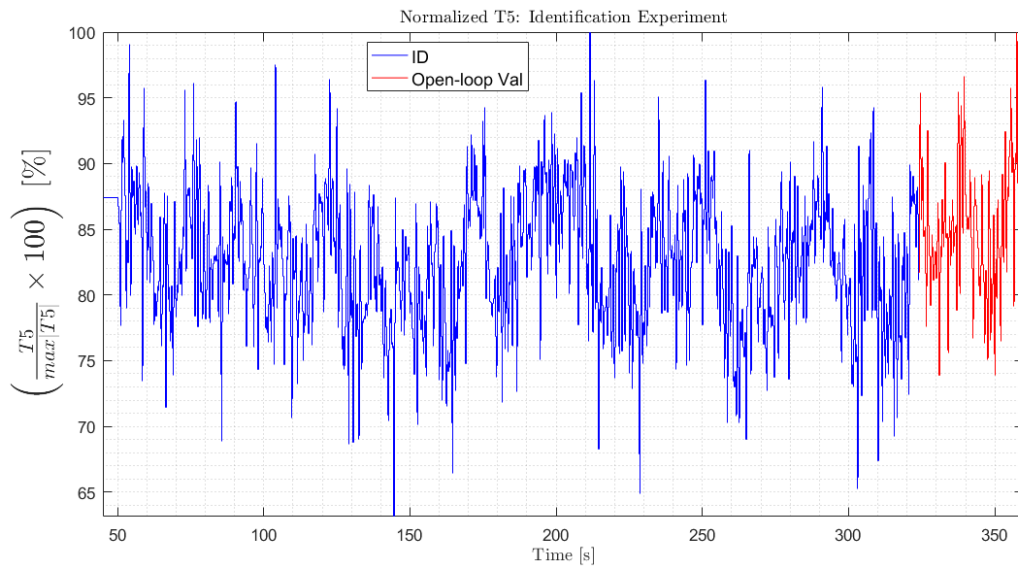
Figure 4.12: Normalized time-domain $T5$ signal generated by the HFGT model in the identification experiment.
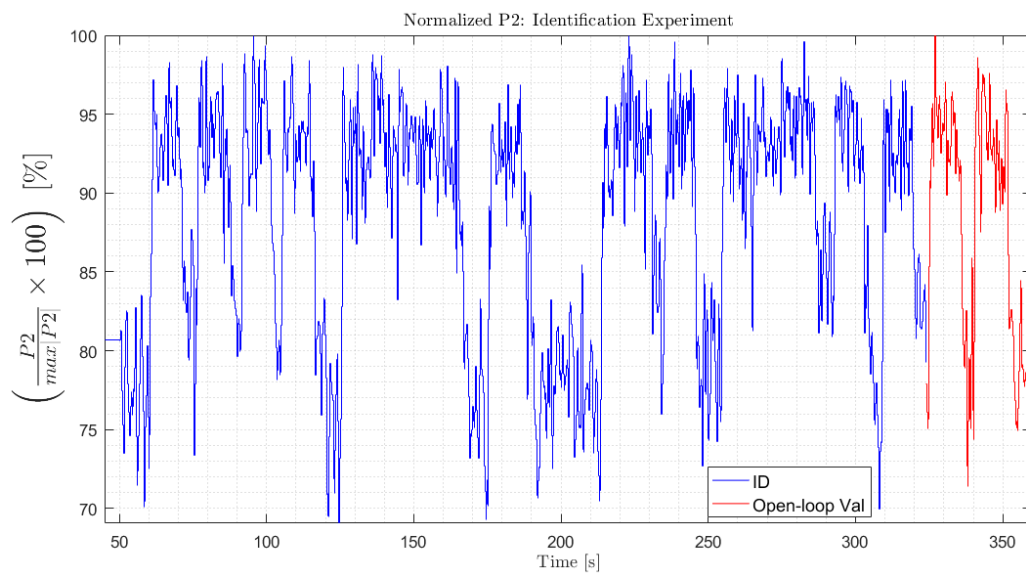

Figure 4.13: Normalized time-domain $P2$ signal generated by the HFGT model in the identification experiment.
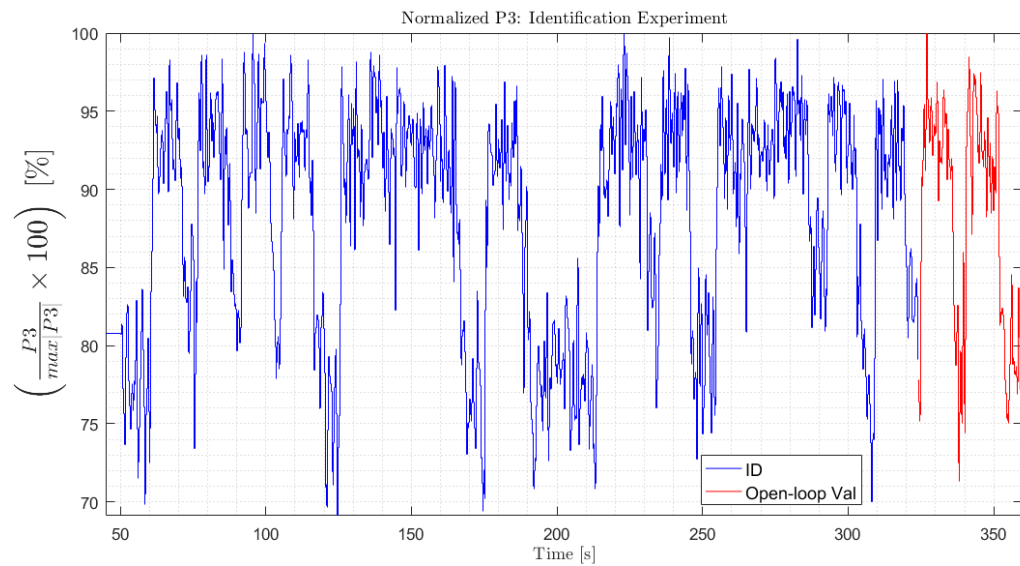
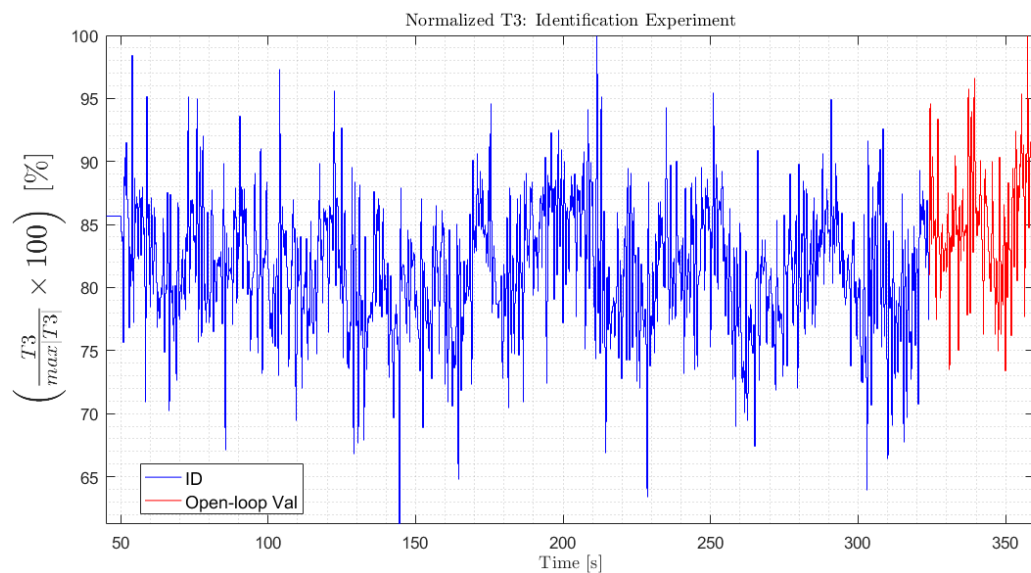Figure 4.14: Normalized time-domain $P3$ signal generated by the HFGT model in the identification experiment.

Figure 4.15: Normalized time-domain $T3$ signal generated by the HFGT model in the identification experiment.
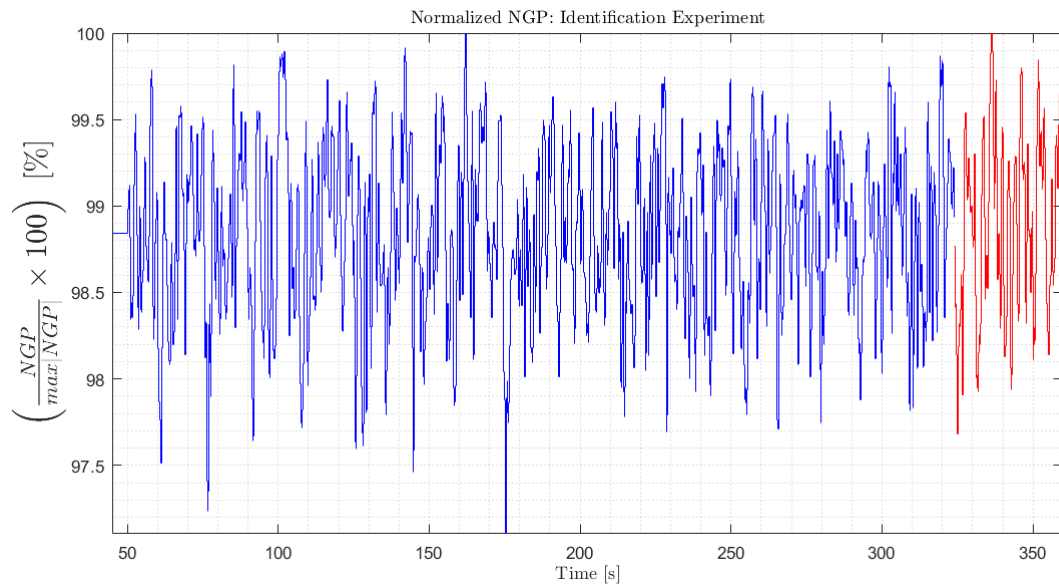
Figure 4.16: Normalized time-domain NGP signal generated by the HFGT model in the identification experiment.

The normalized single-sided amplitude spectra of the measured output signals of the Remainder Subsystem, and NGP, are plotted in Figure 4.17, which show that the engine dynamics were excited in the desired frequency band of $0-1$ Hz.
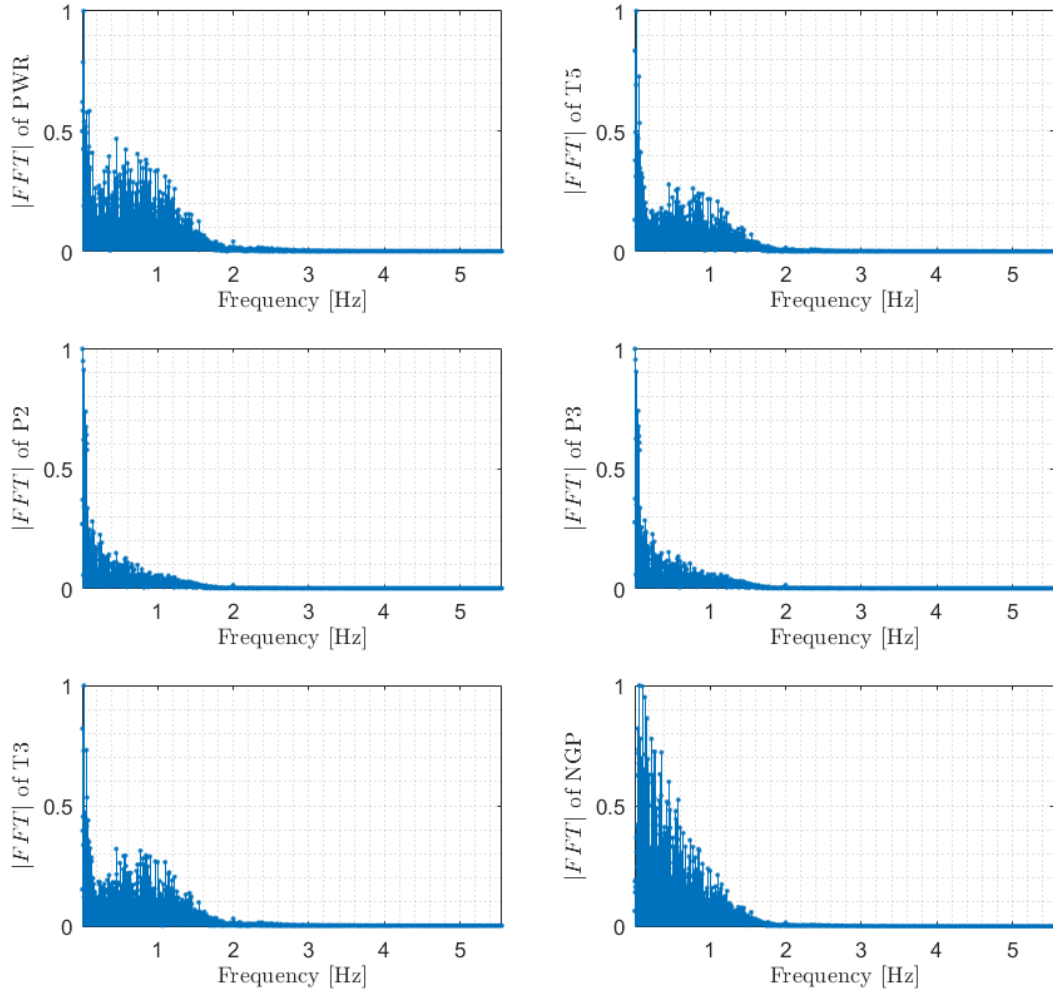
Figure 4.17: Normalized Single-Sided Amplitude Spectra of Measured Output Signals.

Data Pre-Processing

After the identification experiment was conducted, the data was pre-processed before being subjected to identification techniques. Each signal was transformed with a centering and scaling operation as demonstrated with signal $KW(k)$ in the following example:

$$\widetilde{KW}(k) = s_{KW}^{-1} \left(KW(k) - \overline{KW} \right), \tag{4.1}$$

where $k(= 0, 1, 2, \dots)$ is an arbitrary instant of discrete-time, $\widetilde{KW}(k)$ denotes the centered and scaled signal, $\overline{KW}$ is the centering parameter, and s_{KW} is the scaling parameter. The centering parameter and scaling parameter are constants calculated from the identification data subset and are defined by

$$\overline{KW} = \operatorname{mean}\left(KW(k)\right), \tag{4.2}$$

$$s_{KW} = \max \left| KW(k) - \overline{KW} \right| . \tag{4.3}$$

In the remainder of this work, the notation of the preceding example extends to all other signals, where the transformed signal is denoted by a check accent $(\smile)$, the centering parameter is denoted by an over line accent $(\overline{\cdot})$, and the scaling parameter is denoted by the variable 's' with a subscript corresponding to the signal name $\left(s_{(\cdot)}\right)$.

Since the dynamics of the Remainder Subsystem were excited at the desired bandwidth, as evidenced by Figure 4.17, pre-filtering of the data, prior to identification, was unnecessary.

System Identification Design Decisions

After the experimental signal data was pre-processed, a model for the Remainder Subsystem was identified. The input-output signals were chosen to reflect the structure of the Remainder Subsystem, as illustrated in Figure 4.7. Since the HFGT model did not have any noise, there was no need to identify a noise model, and the direct approach of closed-loop identification was applied.

The SSARX subspace identification technique was directly applied to the centered and scaled input-output data using the built-in MATLAB command 'n4sid.m', which was introduced by [48]. The SSARX algorithm was used because it is better suited to handle closed-loop data (see [49]). The built-in MATLAB command 'pem.m' was used to refine the parameters of the initial identified model, obtained with the SSARX technique, with respect to the identification data subset.

The order of the identified model of the Remainder Subsystem was selected by identifying and comparing a 3rd-order model, a 4th-order model, and a 5rd-order model. All three identified models were open-loop stable. The Hankel singular values of the three identified models are plotted in Figure 4.18. A significant difference between the 3rd and

4th ordered Hankel singular values was observed in all three identified models. Thus, the 3rd-order linear identified model of the Remainder Subsystem was selected.
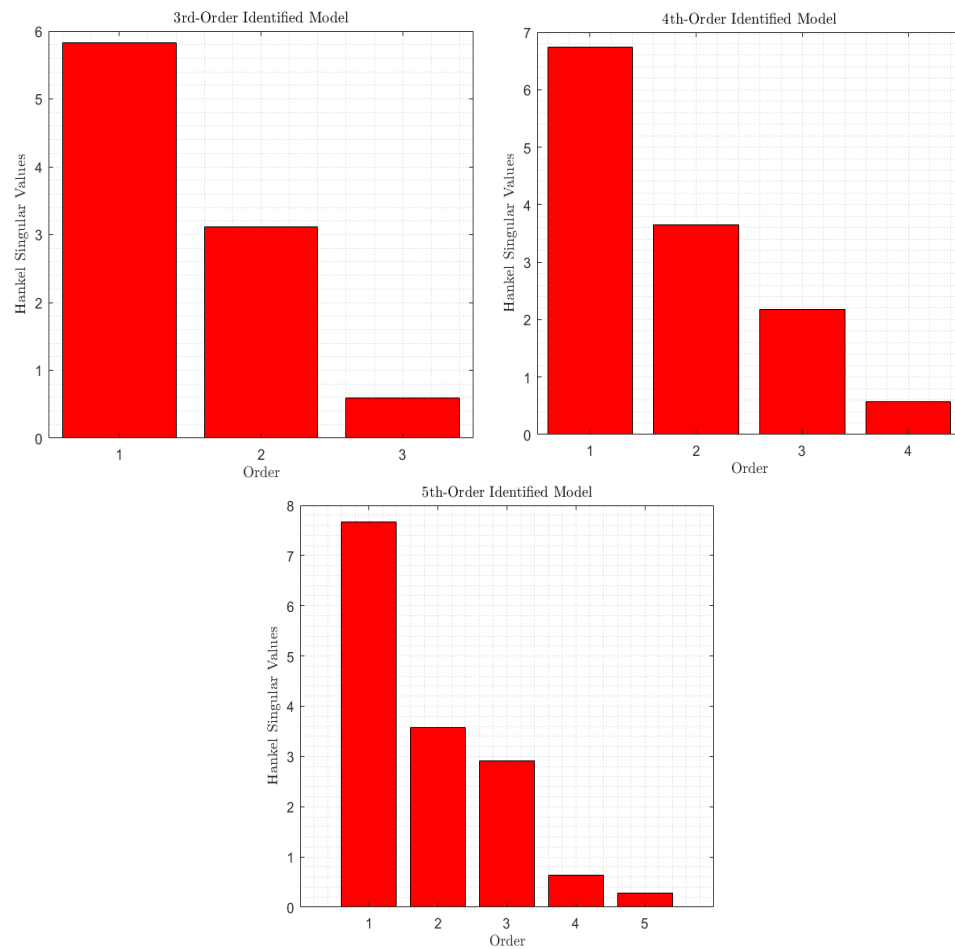

Figure 4.18: Hankel singular values of 3rd-order, 4th-order, and 5th-order identified models of the Remainder Subsystem.

Additionally, the 3rd-order model had no negative real poles, whereas the 4th-order and 5rd-order identified models both had a negative real pole. A negative real pole in the discrete-time complex frequency plane has no unique counterpart in the continuous-time complex frequency domain. Hence, the 3rd-order model could be consistently converted to a continuous-time model without increasing model order, unlike the 4th-order and 5rd-order models. The ability to convert the identified model to a continuous-time representation enabled the LTI GT model to be validated in closed-loop via transient simulation, which required a variable step solver.

Open-Loop Model Validation

The identified model of the Remainder Subsystem was validated in open-loop, the results of which are plotted in Figure 4.19. Experimental signal data belonging to the open-loop validation data subset ($324\ s < t \leq 351.91\ s$) was used in order to mitigate the risk of over-fitting. The identified model of the Remainder Subsystem generated output signals PWR, $T5$, $P2$, $P3$, and $T3$ from open-loop experimental data with input signals NGP, WFI, and GVC. In Figure 4.19, the model-generated signals are colored in gray. The corresponding open-loop experimental output signals of the HFGT model are colored blue. The model-predicted signals and experimental data were compared with the normalized root means square error (NRMSE) goodness of fit, expressed as a percentage in the plot legends.
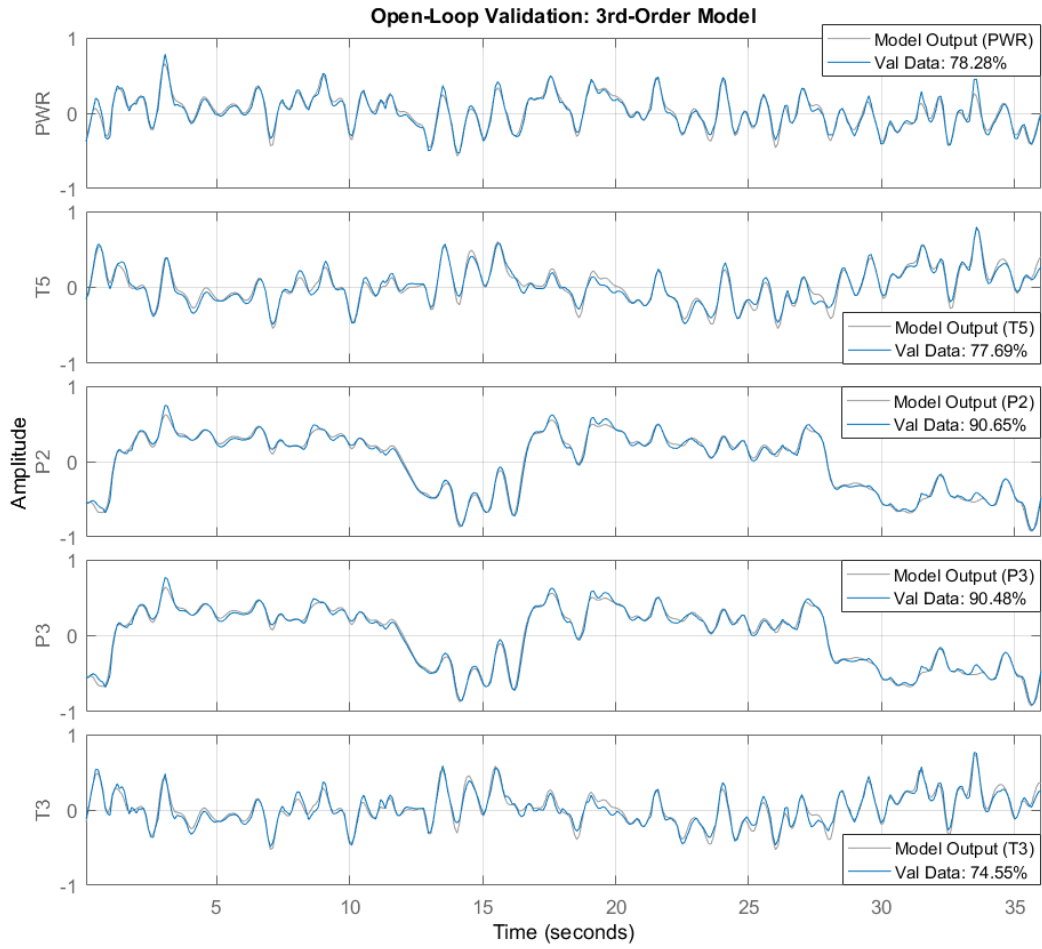
Figure 4.19: Open-loop validation of identified model of the Remainder Subsystem.

Posing the Identified Model of the Remainder Subsystem

We pose the identified model of the Remainder Subsystem with the discrete-time state-space realization

$$x(k + 1) = Ax(k) + B_u \breve{u}(k) + B_{NGP}\widetilde{NGP}(k), \tag{4.4}$$

$$\breve{y}(k) = Cx(k), \tag{4.5}$$

where the state of the identified model of the Remainder Subsystem is denoted by $x(k) \in \mathbb{R}^3$, the model output signal is denoted by $\breve{y} \in \mathbb{R}^5$, the controlled input signal is denoted by $\breve{u} \in \mathbb{R}^2$, and the identified model matrices are denoted by $\{A, B_u, B_{NGP}, C\}$.

Signals $\breve{u}$ and $\breve{y}$ are defined by

$$\breve{u}(k) = \begin{bmatrix} \widetilde{WFI}(k) \\ \widetilde{GVC}(k) \end{bmatrix}, \quad \breve{y}(k) = \begin{bmatrix} \widetilde{PWR}(k) \\ \widetilde{T5}(k) \\ \widetilde{P2}(k) \\ \widetilde{P3}(k) \\ \widetilde{T3}(k) \end{bmatrix}. \tag{4.6}$$

Note that the input and output signals of the identified model correspond to the scaled and centered (i.e. pre-processed) signals.

4.5.3 Rotor Subsystem Model: Linear Approximation

The high-fidelity model of the Rotor Subsystem takes the form of the continuous-time nonlinear dynamical system

$$\frac{d\,[NT(t)]}{dt} = \left(\frac{\alpha}{NT(t)}\right)\Bigg[PWR(t) - \mathbf{Sloss}\big(NT, P2\big)$$

$$... - \mathbf{GBloss}\Big(PWR, \mathbf{Sloss}\big(NT, P2\big)\Big)$$

$$... - \mathbf{GENloss}\Big(PWR, \mathbf{Sloss}\big(NT, P2\big), \mathbf{GBloss}\Big(PWR, \mathbf{Sloss}\big(NT, P2\big)\Big)\Big)$$

$$... - k_0 KW(t)\Bigg], \tag{4.7}$$

$$NGP(t) = c_5 NT(t), \tag{4.8}$$

where the state of the model is denoted by NT, which is proportional to the model output NGP, and the constant parameter α is proportional to the inertia of the rotor. The functions **Sloss**, **GBloss**, and **GENloss** are loss functions which serve a dissipative role and, together with the contribution of KW, act against the lossless net engine power PWR. Together, these signals balance the torque on the rotor.

The loss functions are static look-up maps which take analog engine signals as arguments, which themselves depend on time, but for the sake of notational simplicity the dependence of the loss functions on time t is not explicitly written.

The *radial loss function* $\mathbf{Sloss} : \mathbb{R} \times \mathbb{R} \to \mathbb{R}$ is defined by

$$\mathbf{Sloss}(NT, P2) = k_1 P2(t) - k_2 P_0 + \mathbf{f_{rad}}(NT), \tag{4.9}$$

with associated lookup table $\mathbf{f_{rad}} : \mathbb{R} \to \mathbb{R}$ and constant parameters P_0, k_1, and k_2. Additionally, the lookup table $\mathbf{f_{rad}}$ is dependent on internal constant parameters k_3 and k_4.

The *gearbox loss function* $\mathbf{GBloss} : \mathbb{R} \times \mathbb{R} \to \mathbb{R}$ is the defined by

$$\mathbf{GBloss}\big(PWR, \mathbf{Sloss}(NT, P2)\big) = \mathbf{f_{gb}}\Big(PWR(t) - \mathbf{Sloss}(NT, P2)\Big), \tag{4.10}$$

with associated lookup table $\mathbf{f_{gb}} : \mathbb{R} \to \mathbb{R}$.

The *generator loss function* $\mathbf{GENloss} : \mathbb{R} \times \mathbb{R} \times \mathbb{R} \to \mathbb{R}$ is defined by

$$\mathbf{GENloss}\Big(PWR, \mathbf{Sloss}(NT, P2), \mathbf{GBloss}\big(PWR, \mathbf{Sloss}(NT, P2)\big)\Big) =$$

$$...k_5 \mathbf{f_{gen}}\Big(PWR(t) - \mathbf{Sloss}(NT, P2)$$

$$... - \mathbf{GBloss}\big(PWR, \mathbf{Sloss}(NT, P2)\big)\Big), \tag{4.11}$$

with associated lookup table $\mathbf{f_{gen}} : \mathbb{R} \to \mathbb{R}$ and constant parameter k_5.

Linear Approximate Model Construction

A linear approximation of the high-fidelity Rotor Subsystem model was constructed based on the values of signals in the model at a steady-state operating point. In steady-state operation at the nominal load $KW = \overline{KW}$, and with no external excitations, i.e. $dWFI \equiv 0$ and $dGVC \equiv 0$ for all times t, we define steady state values

$$NT = \overline{NT}, \quad \mathbf{GBloss} = \overline{\mathbf{GBloss}}. \quad \mathbf{GENloss} = \overline{\mathbf{GENloss}}, \tag{4.12}$$

In order to obtain an LTI rotor model, the steady-state values of (4.12) were selectively substituted into the right-hand side of the nonlinear rotor dynamics of (4.7) as follows:

$$\frac{d\left[NT(t)\right]}{dt} = \left(\frac{\alpha}{\overline{NT}}\right) \left[PWR(t) - \mathbf{Sloss}\big(\overline{NT}, P2\big) - \overline{\mathbf{GBloss}} - \overline{\mathbf{GENloss}}\right]. \tag{4.13}$$

From the definition of **Sloss** in (4.9), the preceding substitution yields a *continuous-time linear approximate rotor model* given by

$$\frac{d\left[NT(t)\right]}{dt} = A_c^r NT(t) + B_c^r \begin{bmatrix} PWR(t) \\ P2(t) \\ KW(t) \end{bmatrix} + c_4, \tag{4.14}$$

$$NGP(t) = C_c^r NT(t), \tag{4.15}$$

where the system matrices are defined by

$$A_c^r = 0, \quad B_c^r = \begin{bmatrix} c_1 & c_2 & c_3 \end{bmatrix}, \quad C_c^r = c_5. \tag{4.16}$$

with the constant parameters

$$c_1 = \frac{\alpha}{\overline{NT}},$$

$$c_2 = -k_1 c_1,$$

$$c_3 = -k_0 c_1,$$

$$c_4 = c_1 \left(k_2 P_0 - \mathbf{f_{rad}}\left(\overline{NT}\right) - \overline{\mathbf{GBloss}} - \overline{\mathbf{GENloss}}\right).$$

For a sample period t_s, and denoting an instant of discrete-time by k, where $t = t_s k$, the corresponding *discrete-time linear approximate rotor model* is given by

$$NT(k+1) = A_d^r NT(k) + B_d^r \begin{bmatrix} PWR(k) \\ P2(k) \\ KW(k) \end{bmatrix} + c_4, \tag{4.17}$$

$$NGP(k) = C_d^r NT(k), \tag{4.18}$$

where the system matrices are defined by

$$A_d^r = 1, \quad B_d^r = \begin{bmatrix} b_1^r & b_2^r & b_3^r \end{bmatrix} = t_s B_c^r, \quad C_d^r = c_5. \tag{4.19}$$

Note that the linear approximate rotor model is a 1st-order system which is marginally stable.

This rotor model is defined with respect to the nominal load $\overline{KW}$ at which the steady state values used to simplify the high-fidelity dynamics are defined. A simulation experiment with the HFGT model was conducted with a constant $\overline{KW} = 0.75 \cdot KW_{rated}$,

and the steady state values were recorded. A model of the Rotor Subsystem can be just as easily obtained at any other operating point by conducting a similar experiment at the desired nominal load value and recording the appropriate steady state values in (4.12). Thus, in practice, construction of a family of linear approximate rotor models, defined with respect to $\overline{KW}$, can be readily acquired. Furthermore, it is worth noting that the necessary steady state values in (4.12) are not directly measurable during in situ experiments with a physical rotor, but were readily available in the HFGT model.

Moreover, the parameters $\{c_1, c_2, c_3, c_4, c_5\}$ contain the original parameters of the high-fidelity model of the Rotor Subsystem. Therefore, the constructed linear rotor model can be used to characterize a wide range of rotor models by adjusting these parameters to different values. This feature of the model gives it significant generality. If the Rotor Subsystem had not been separated from the Remainder Subsystem, then a single model characterizing both subsystems would be obtained by system identification, and the resulting identified model would only be able to accommodate the exact rotor used in the identification experiments.

4.5.4 Augmented LTI Gas Turbine Model for Control Design

The discrete-time LTI GT model is constructed by augmenting the identified model of the Remainder Subsystem, obtained in Section 4.5.2 (see (4.4)-(4.5)), with the linear approximate model of the Rotor Subsystem, obtained in Section 4.5.3 (see (4.17)-(4.19)). In order to ensure dimensional consistency, the identified model of the Remainder Subsystem was re-written with input-output signals in the same units as the raw signal data (without pre-processing), and to this end we define the constant quantities

$$S_u = \begin{bmatrix} s_{WFI} & 0 \\ 0 & s_{GVC} \end{bmatrix}, \quad \overline{u} = \begin{bmatrix} \overline{WFI} \\ \overline{GVC} \end{bmatrix}, \tag{4.20}$$

$$S_y = \begin{bmatrix} s_{PWR} & 0 & 0 & 0 & 0 \\ 0 & s_{T5} & 0 & 0 & 0 \\ 0 & 0 & s_{P2} & 0 & 0 \\ 0 & 0 & 0 & s_{P3} & 0 \\ 0 & 0 & 0 & 0 & s_{T3} \end{bmatrix}, \quad \overline{y} = \begin{bmatrix} \overline{PWR} \\ \overline{T5} \\ \overline{P2} \\ \overline{P3} \\ \overline{T3} \end{bmatrix}. \tag{4.21}$$

For convenience, we also define

$$b_{rot} = \begin{bmatrix} b_1^r & 0 & b_2^r & 0 & 0 \end{bmatrix}, \quad I_y = \begin{bmatrix} 0 & 1 & 0 & 0 & 0 \\ 0 & 0 & 1 & 0 & 0 \\ 0 & 0 & 0 & 1 & 0 \\ 0 & 0 & 0 & 0 & 1 \end{bmatrix}. \tag{4.22}$$

LTI GT Model: Augmented State-Space Realization

A discrete-time state-space realization of the LTI GT model is given by

$$x_a(k+1) = A_a x_a(k) + B_a u(k) + B_{KW} KW(k) + G_{in}, \tag{4.23}$$

$$y_a(k) = C_a x_a(k) + G_{out}, \tag{4.24}$$

where the augmented state is denoted by $x_a \in \mathbb{R}^4$, the augmented measured output signal is denoted by $y_a \in \mathbb{R}^5$, and where G_{in} and G_{out} are constant matrices, where

$$x_a(k) = \begin{bmatrix} x(k) \\ NT(k) \end{bmatrix}, \quad y_a(k) = \begin{bmatrix} NGP(k) \\ T5(k) \\ P2(k) \\ P3(k) \\ T3(k) \end{bmatrix}, \tag{4.25}$$

$$G_{in} = \begin{bmatrix} -B_u S_u^{-1} \overline{u} - B_{NGP} s_{NGP}^{-1} \overline{NGP} \\ b_{rot} \overline{y} + c_4 \end{bmatrix}, \quad G_{out} = \begin{bmatrix} 0 \\ I_y \overline{y}, \end{bmatrix}; \tag{4.26}$$

and where the LTI GT model matrices, denoted by A_a, B_a, B_{KW}, and C_a are defined by

$$A_a = \begin{bmatrix} A & B_{NGP} s_{NGP}^{-1} C_d^r \\ b_{rot} S_y C & A_d^r \end{bmatrix}, \quad B_a = \begin{bmatrix} B_u S_u^{-1} \\ 0 \end{bmatrix}, \tag{4.27}$$

$$B_{KW} = \begin{bmatrix} 0 \\ b_3^r \end{bmatrix}, \quad C_a = \begin{bmatrix} 0 & C_d^r \\ I_y S_y C & 0 \end{bmatrix}. \tag{4.28}$$

Note that signal PWR is not present within the LTI GT model, and thus does not need to be measured or known by a controller designed using the LTI GT model. The LTI GT model was converted to an equivalent continuous-time representation for closed-loop validation transient simulations, which require the use of a variable step solver.

4.6 Closed-Loop Validation of the LTI GT Model

The LTI GT model was validated using a closed-loop transient simulation implemented in Simulink, termed the *validation experiment* in this work. The performance of the LTI GT model was measured with respect to its ability to reproduce the output signals NGP, $T5$, $P2$, $P3$, and $T3$, in closed-loop with the Existing Controller block and the high-fidelity model of the Fuel Subsystem. Signals NGP and $T5$ were of particular importance due to their significance in potential GT controllers designed using the LTI GT model.

Two closed-loop systems were simultaneously simulated, one containing the LTI GT model (shown in Figure 4.20) and the other containing the HFGT model (depicted in Figure 4.5), which generated output signals used as reference data for comparison with the output signals produced by the LTI GT model.
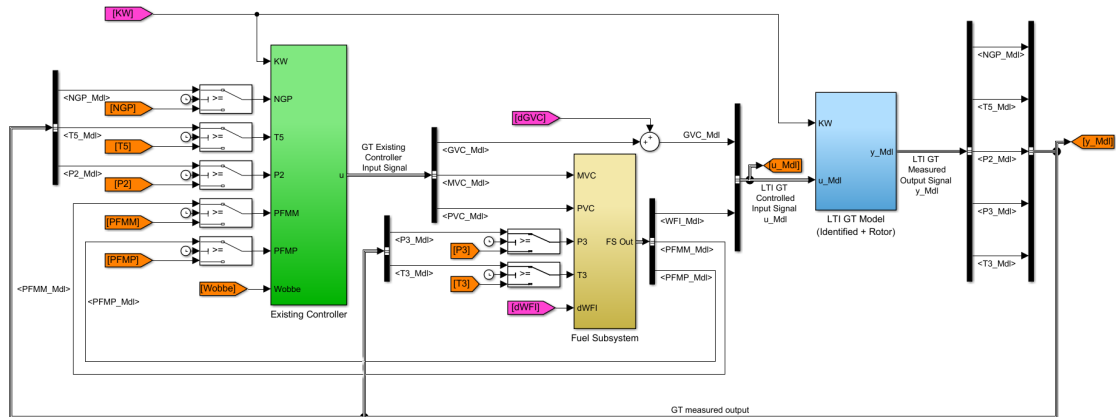
Figure 4.20: Closed-loop validation system with LTI GT model regulated by the Existing Controller block.

Both closed-loop systems were simulated with identical initial conditions, constant ambient conditions (ISO standard day), constant Wobbe index (SDNG fuel), and exogenous load signal KW, which is plotted in Figure 4.21. The nominal load $\overline{KW}$ was set to 75 % of the rated load value. In order to reduce the transient effects of initial conditions, dKW was set to a value of zero for the first 50 s of the validation experiment. For the remainder of the validation experiment ($t \geq 50$ s) the perturbation load dKW was implemented as zero-mean uniform white noise distributed on the load interval ± 10 %

of the rated load value and a sample time of 5 s. No control excitation was used, i.e. $dWFI$ and $dGVC$ were set identically to zero for the entire simulation.
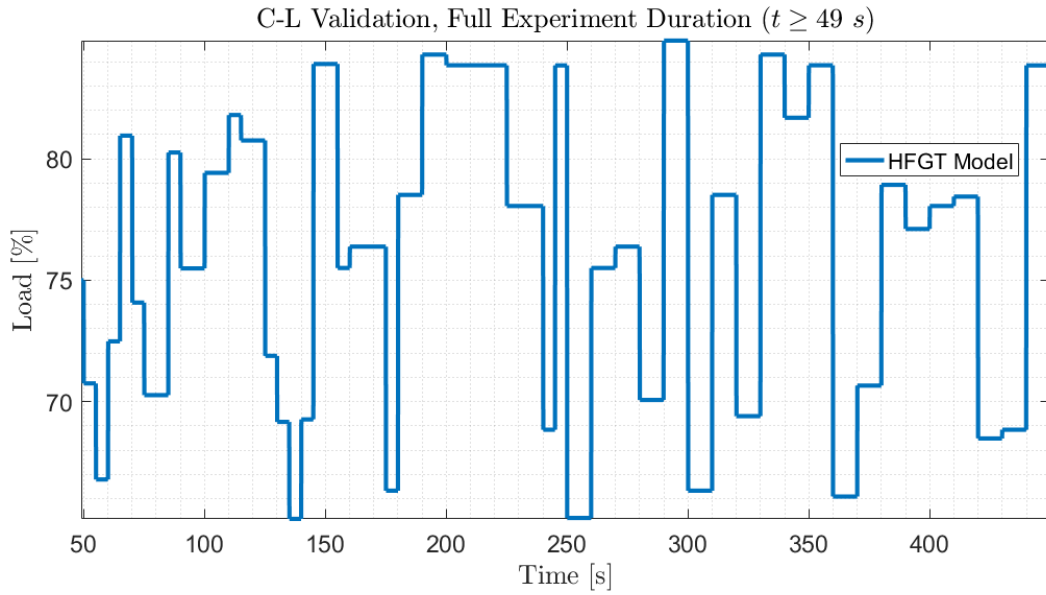

Figure 4.21: Closed-loop validation data for KW. On the time interval $0\ s \leq t < 50\ s$, the load had constant value $KW = 0.75 \times KW_{rated}$.

The total duration of the validation experiment was 449.91 s. Data was sampled at $t_s = 0.09$ s and a total of 5000 data points were recorded per signal. For the initial 10 s of the simulation, $(0\ s \leq t < 10\ s)$ the closed-loop system containing the LTI GT model was simulated in open-loop, using endogenous signals NGP, $T5$, $P2$, $P3$, $T3$, $PFMM$, and $PFMP$ taken from the closed-loop system containing the HFGT model, which mitigated the transient effects due to the initial conditions. For the remaining duration of the simulation ($t \geq 10\ s$), the system containing the LTI GT model was simulated in closed-loop and was operated independently of the closed-loop system containing the HFGT model.

Closed-Loop Validation Results: Measured Output Signal Comparison

Figures 4.22-4.31 contain plots comparing the measured output signals generated by the HFGT model and those generated by the LTI GT model. The plots are presented in pairs. The first plot of each pair contains data in the time interval $t \geq 49\ s$, i.e. the

time interval when both systems are operating as independent closed-loop systems and when the load excitation is active. The title of the first plot of each pair also contains the normalized root mean square error (NRMSE) between the signal generated by the LTI GT model and the corresponding signal generated by the HFGT model, which quantifies the goodness of fit of the output signals of the LTI GT model. The second plot of each pair contains the same signals as its preceding plot, but on a zoomed-in time interval for visual clarity. These time intervals were selected during particularly dynamic sections of the data. All plotted signals are centered and scaled with the same centering and scaling parameters associated with the LTI GT model.
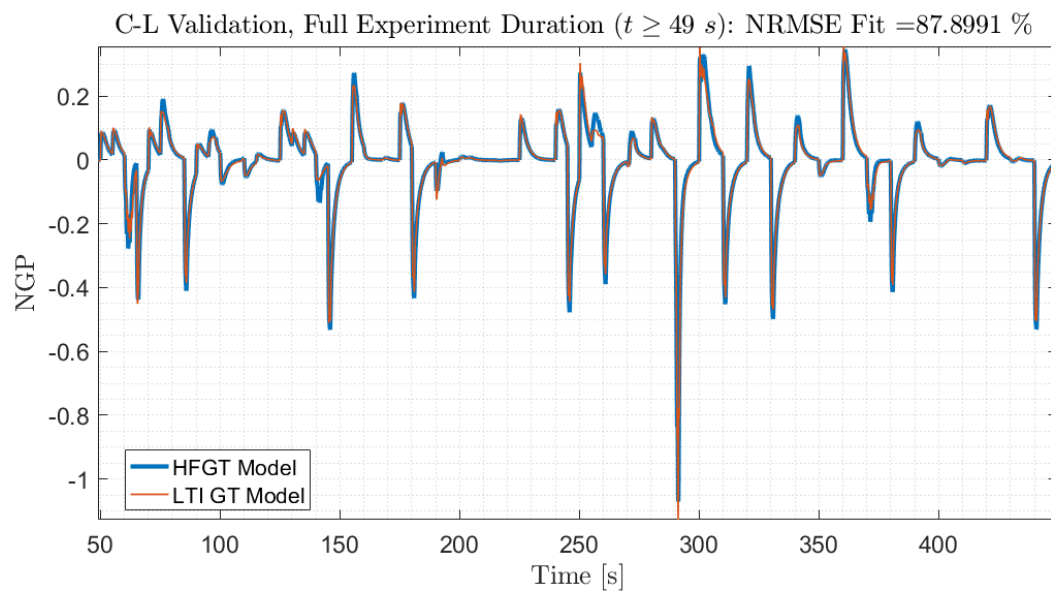
Figure 4.22: Closed-loop validation data for NGP.
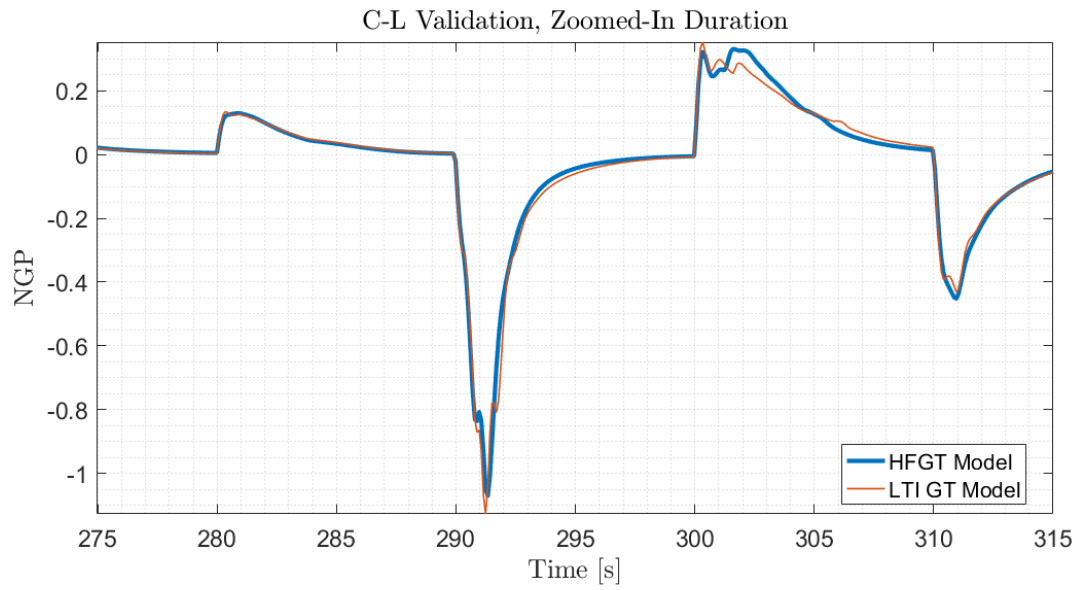
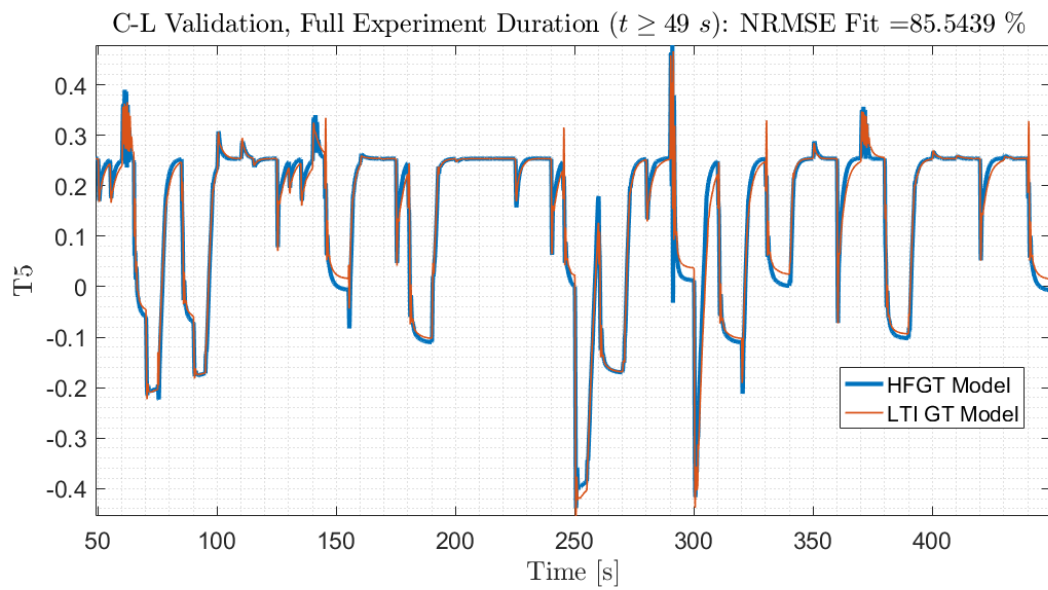Figure 4.23: Zoomed-In plot of closed-loop validation data for NGP in Figure 4.22.
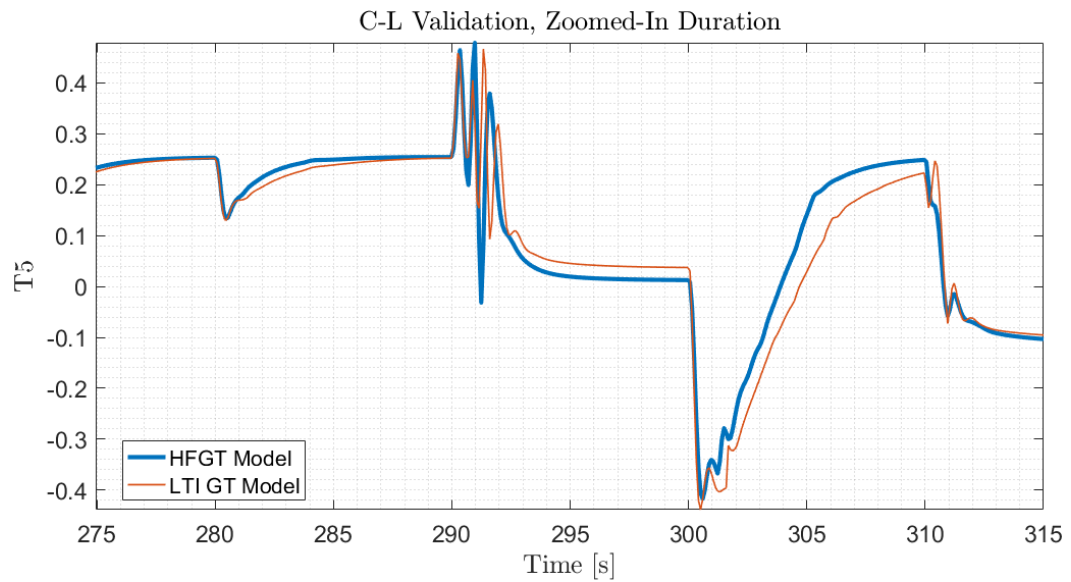

Figure 4.24: Closed-loop validation data for T5.

Figure 4.25: Zoomed-In plot of closed-loop validation data for T5 in Figure 4.24.

As previously stated, signals NGP and $T5$ were of particular interest for control design, and the LTI GT model shows good agreement with the closed-loop signal data from the HFGT model.
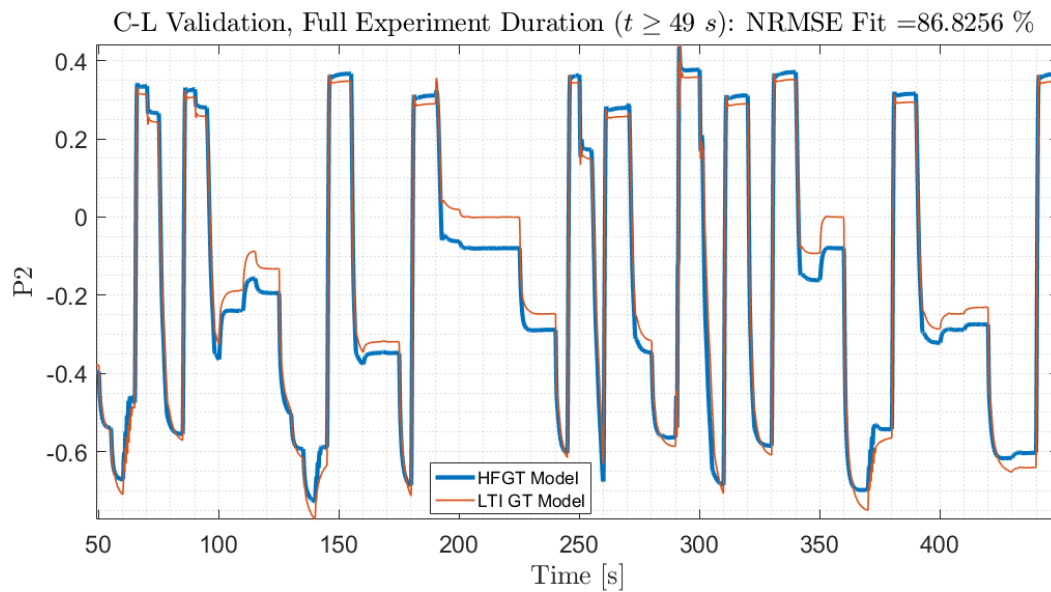

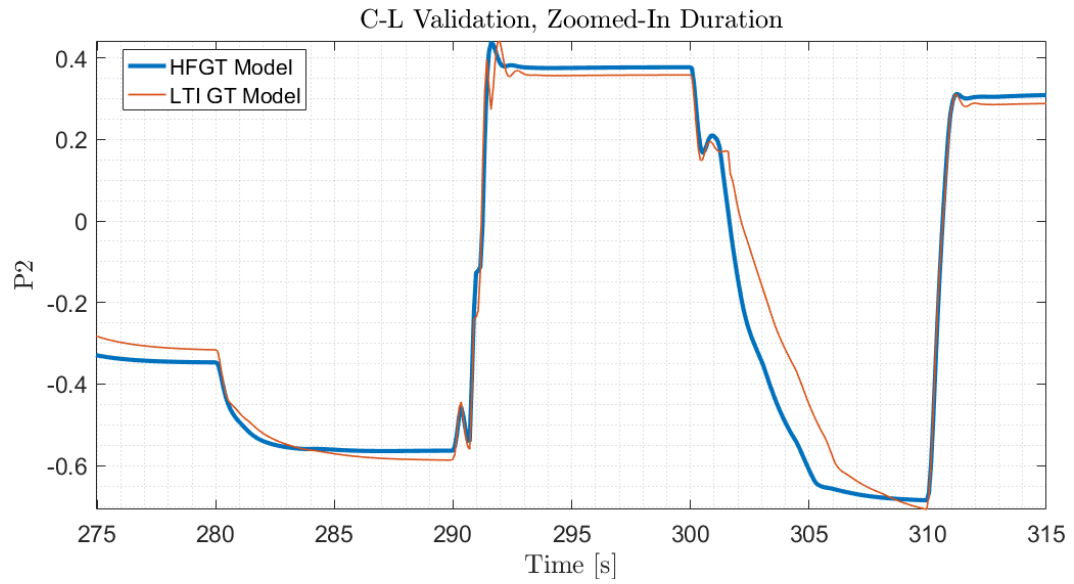Figure 4.26: Closed-loop validation data for P2.

Figure 4.27: Zoomed-In plot of closed-loop validation data for P2 in Figure 4.26.
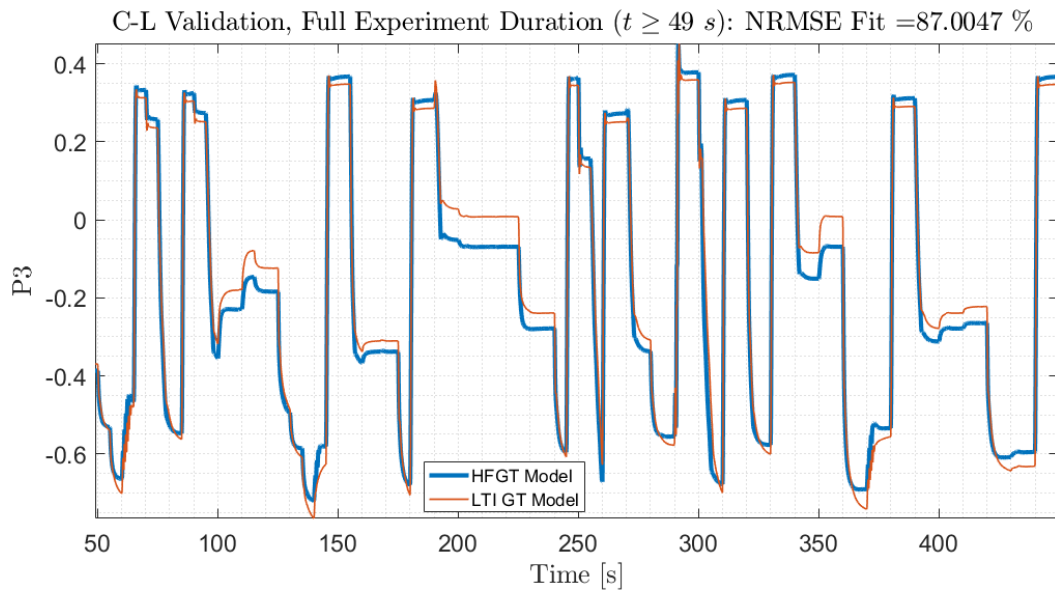

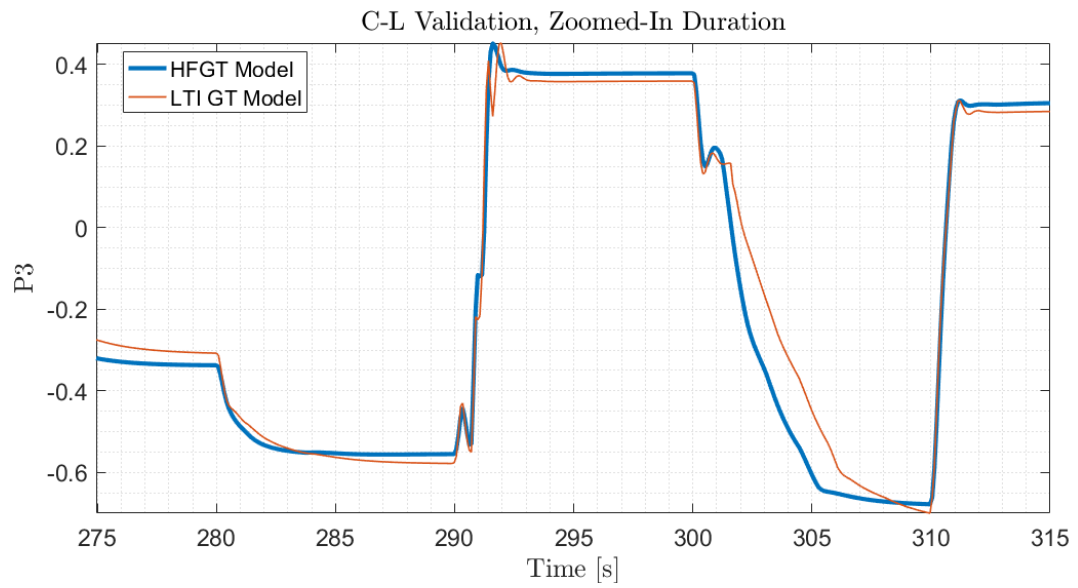Figure 4.28: Closed-loop validation data for P3.

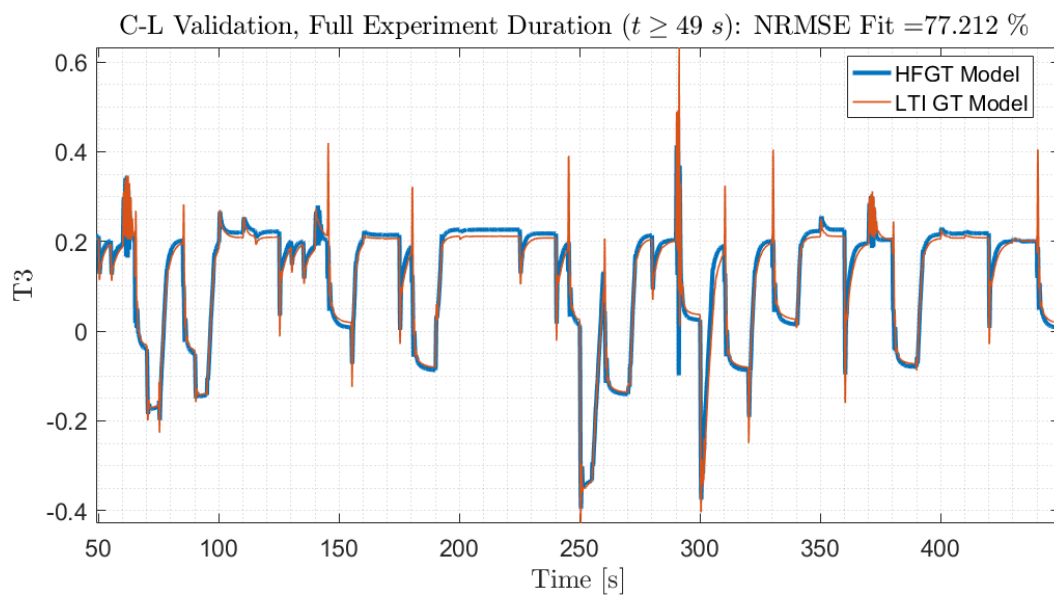Figure 4.29: Zoomed-In plot of closed-loop validation data for P3 in Figure 4.28.

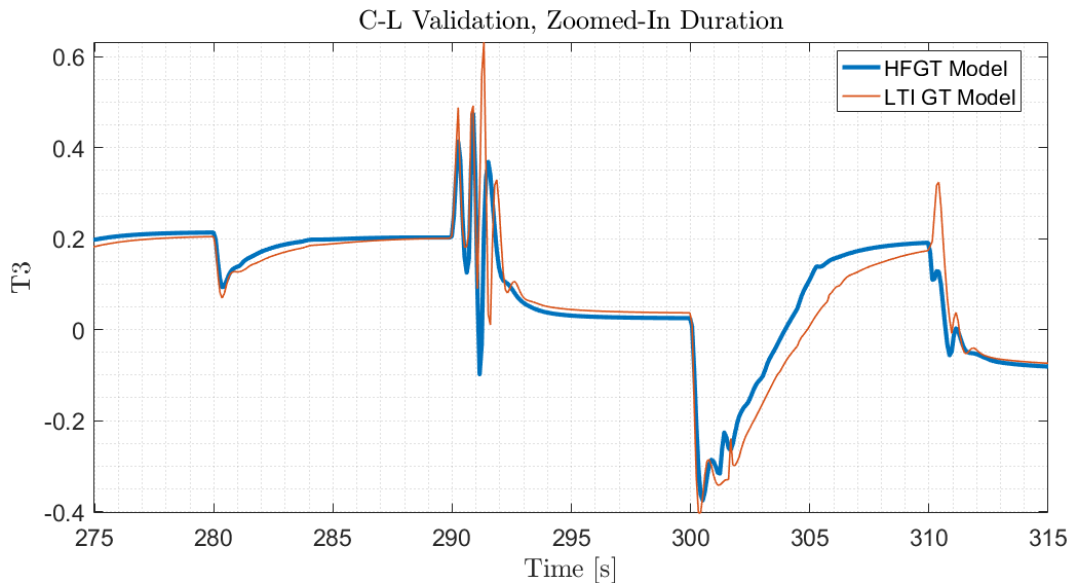Figure 4.30: Closed-loop validation data for T3.

Figure 4.31: Zoomed-In plot of closed-loop validation data for T3 in Figure 4.30.

The closed-loop validation data and NRMSE values, as plotted in Figures 4.22-4.31, indicate that the LTI GT model is acceptable for control design, and is capable of reproducing the output signals of the HFGT model with good agreement.

Closed-Loop Validation Results: Controlled Input Signal Comparison

Although the primary objective of the closed-loop validation experiment was to reproduce the measured engine output signals, the controlled input signals and their associated NRMSE values showed surprisingly close agreement. The controlled input signals are plotted in Figures 4.32-4.35.
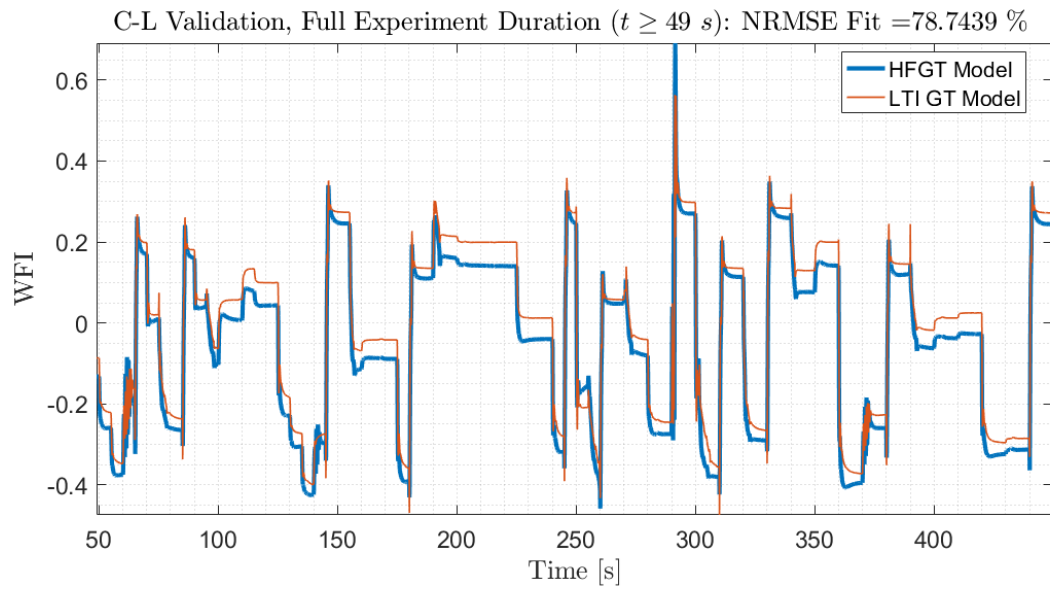
Figure 4.32: Closed-loop validation data for WFI.
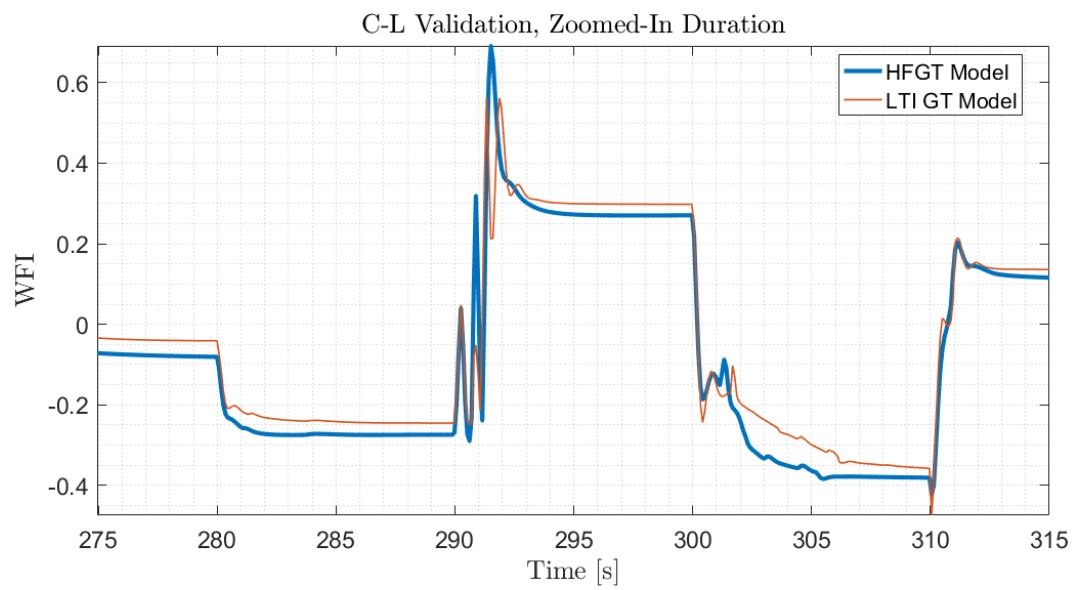

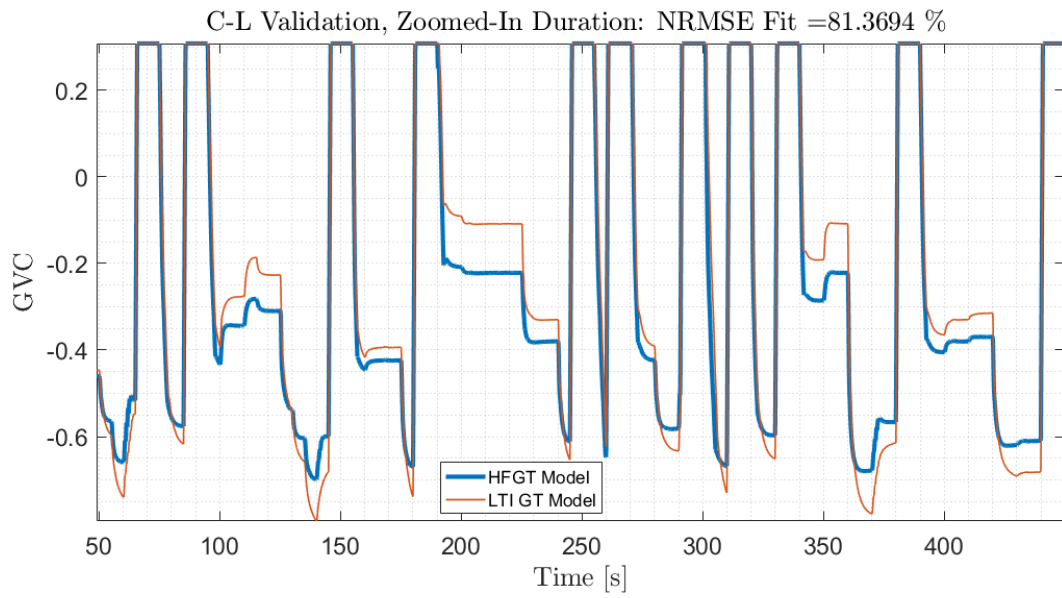Figure 4.33: Zoomed-In plot of closed-loop validation data for WFI in Figure 4.32.

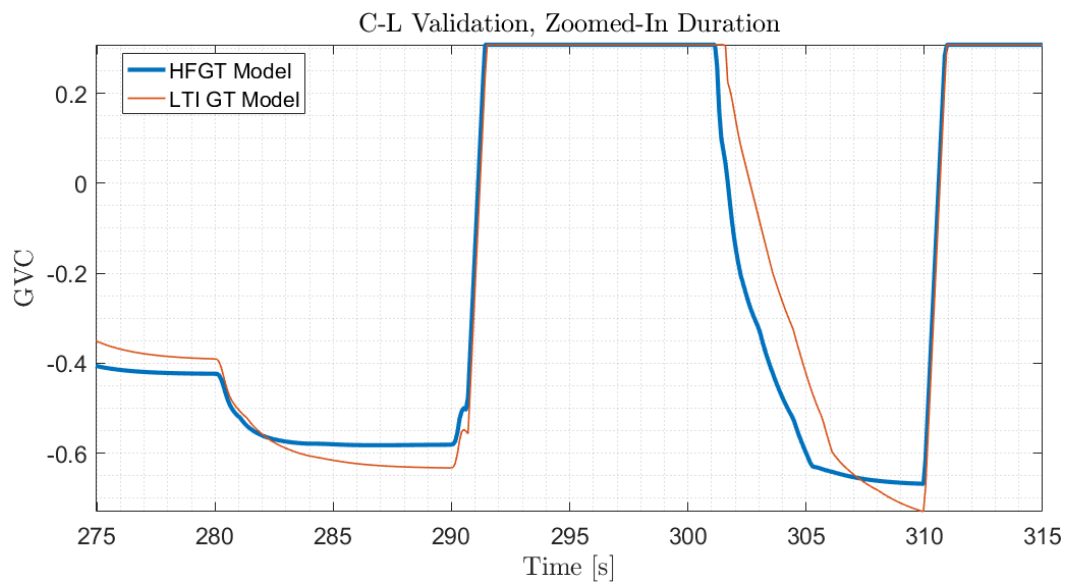Figure 4.34: Closed-loop validation data for GVC.

Figure 4.35: Zoomed-In plot of closed-loop validation data for GVC in Figure 4.34.

4.7   Summary

A linear time-invariant gas turbine model suitable for control design was constructed by leveraging a high-fidelity model of the gas turbine engine and associated prior knowledge of the structure and signals made available via the high-fidelity model. The structural knowledge of the high-fidelity model enabled a modular grouping of its internal subsystem blocks into three categories, the Fuel Subsystem, which was excluded from the modeling process and thereby rendered modularly generalizable in potential control designs; the Remainder Subsystem, which was obtained via system identification using closed-loop transient data generated by the high-fidelity model; and the Rotor Subsystem, for which a linear model was constructed which preserved the physical significance of its model parameters, enabling modular generalization of the subsystem in potential control design. The constructed linear rotor model was successfully validated in closed-loop transient simulation and the output signals of the linear rotor model displayed a high degree of agreement with those generated by the high-fidelity engine model under comparable experimental conditions.

Potential future directions of this work include are numerous. Validation of the open-loop LTI GT model with batch data from in situ testing of a physical engine is a natural next step. Likewise, LTI GT models obtained with the methods of this work can be applied to control design and estimator design problems with various Fuel Subsystem models, rotors, and nominal loads spanning the entire operational envelop. The resulting controllers and estimators can be validated via transient simulation experiments in Simulink or even with in situ experiments on a physical engine, if available, and the performance of new controller and estimator designs can be benchmarked against the existing controller. Another potential direction of inquiry is the exploration of the limits of a given LTI GT model in terms of how the quality of the model, or of controllers and estimators designed with the model, degrades as KW deviates from the $\overline{KW}$. Further development can also incorporate health parameter estimation, fault detection, and other augmented functionality similar to approaches in [50], [51], [52], and [53].

Bibliography

[1] Solar Turbines Incorporated, Taurus 60 gas turbine generator set, in: http://s7d2.scene7.com/is/content/Caterpillar/C10550197 [Accessed: 23.05.2017], 2009.

[2] D. S. Carrasco, G. C. Goodwin, Feedforward model predictive control, Annual Reviews in Control 35 (2) (2011) 199 – 206.

[3] N. Birla, A. Swarup, Optimal preview control: A review, Optimal Control Applications and Methods 36 (2) (2015) 241–268.

[4] E. Bender, Optimum linear preview control with application to vehicle suspension, Journal of Fluids Engineering 90 (2) (1968) 213–221.

[5] M. Tomizuka, "Optimum linear preview control with application to vehicle suspension"—revisited, Journal of Dynamic Systems, Measurement, and Control 98 (3) (1976) 309–315.

[6] H. Roh, Y. Park, Stochastic optimal preview control of an active vehicle suspension, J. Sound and Vibration 220 (1999) 313–330.

[7] J. Marzbanrad, G. Ahmadi, H. Zohoor, Y. Hojjat, Stochastic optimal preview control of a vehicle suspension, Journal of Sound and Vibration 275 (3–5) (2004) 973 – 990.

[8] I. Youn, R. Tchamna, S. H. Lee, N. Uddin, S. K. Lyu, M. Tomizuka, Preview suspension control for a full tracked vehicle, International Journal of Automotive Technology 15 (3) (2014) 399–410.

[9] J. Laks, L. Pao, A. Wright, N. Kelley, B. Jonkman, The use of preview wind measurements for blade pitch control, Mechatronics 21 (2011) 668–681.

[10] F. Dunne, L. Pao, Benefit of wind turbine preview control as a function of measurement coherence and preview time, in: American Control Conference (ACC), 2013, 2013, pp. 647–652.

[11] N. Wang, K. Johnson, A. Wright, C. Carcangiu, Lidar-assisted preview controllers design for a mw-scale commercial wind turbine model, in: 52nd IEEE Conference on Decision and Control (CDC), 2013, pp. 1678–1683.

[12] D. Schlipf, Flatness-based feedforward control of wind turbines using lidar, in: E. Boje (Ed.), Proceedings of the 19th IFAC World Congress, IFAC, Elsevier, 2014, pp. 5820 – 5825.

[13] A. Hazell, D. Limebeer, A framework for discrete-time $\mathscr{H}_2$ preview control, J. Dyn. Syst., Meas., Control 132 (3).

[14] M. Hovd, R. R. Bitmead, Feedforward for stabilization in the presence of constraints, J. Process Control 22 (2012) 659 – 665.

[15] K. Hashikura, A. Kojima, H2 preview control based on partial information, in: Control Conference (CCC), 2014 33rd Chinese, 2014, pp. 9008–9015.

[16] J. L. Guzmán, T. Hägglund, M. Veronesi, A. Visioli, Performance indices for feedforward control, Journal of Process Control 26 (2015) 26–34.

[17] D. L. Shrestha, D. E. Robertson, Q. J. Wang, T. C. Pagano, H. A. P. Hapuarachchi, Evaluation of numerical weather prediction model precipitation forecasts for short-term streamflow forecasting purpose, Hydrology and Earth System Sciences 17 (5) (2013) 1913–1931.

[18] A. Hazell, D. Limebeer, An efficient algorithm for discrete-time $\mathscr{H}_\infty$ preview control, Automatica 44 (2008) 2441–2448.

[19] R. Middleton, J. Chen, J. Freudenberg, Tracking sensitivity and achievable H_∞ performance in preview control, Automatica 40 (8) (2004) 1297 – 1306.

[20] M. Tomizuka, The optimal finite preview problem and its application to man-machine systems., Ph.D. thesis, Massachusetts Institute of Technology (1973).

[21] M. Tomizuka, D. Whitney, Optimal discrete finite preview problems (why and how is future information important?), J. Dyn. Syst., Meas., Control 97 (1975) 319–325.

[22] R. Moroto, R. Bitmead, B. Sleegers, The information structure of feedforward/preview control using forecast data, in: E. Boje (Ed.), Proceedings of the 19th IFAC World Congress, IFAC, Elsevier, 2014, pp. 176 – 181.

[23] B. Anderson, J. Moore, Optimal Filtering, Prentice-Hall, Englewood Cliffs, New Jersey, 1979.

[24] L. Ljung, System Identification: Theory for the User, Prentice-Hall, Inc, Upper Saddle River, New Jersey, 1999.

[25] A. Kwasinski, W. Weaver, R. S. Balog, Microgrids and other Local Area Power and Energy Systems, Cambridge University Press, Cambridge UK, 2016.

[26] D. J. Riggs, R. Bitmead, Rejection of aliased disturbances in a production pulsed light source, IEEE Transactions on Control Systems Technology 21 (2) (2013) 480–488.

[27] B. Anderson, J. Moore, Optimal Filtering, Dover Publications, Mineola NY, 2012.

[28] D. Simon, Optimal State Estimation: Kalman, H_∞, and Nonlinear Approaches, Wiley-Interscience, Hoboken NJ, 2006.

[29] C. Holcomb, R. A. de Callafon, Subspace identification for disturbance rejection control design in gas turbines, in: Proc. 19th ECC Control Conference, Linz, AT, 2015, pp. 842–847.

[30] G. G. Kulikov, H. A. Thompson, Dynamic Modelling of Gas Turbines, Advances in Industrial Control, Springer-Verlag London, 2004.

[31] R. Rajamani, Load rejection rapid acting fuel-air controller for gas turbine, uS Patent 5,896,736 (1999).

[32] O. L. V. Costa, M. D. Fragoso, R. P. Marques, Discrete-time Markov jump linear systems, Springer London, 2006.

[33] O. L. V. Costa, Linear minimum mean square error estimation for discrete-time markovian jump linear systems, IEEE Transactions on Automatic Control 39 (8) (1994) 1685–1689.

[34] C. B. Chang, M. Athans, State estimation for discrete systems with switching parameters, IEEE Transactions on Aerospace and Electronic Systems AES-14 (3) (1978) 418–425.

[35] A. Pandey, M. Oliveira, C. Holcomb, Multi-stage system identification of a gas turbine, in: Proc. ASME Turbo Expo 2017 Turbine Technical Conference & Exposition. Charlotte, NC, USA., 2017.

[36] V. Arkov, C. Evans, P. Fleming, D. Hill, J. Norton, I. Pratt, D. Rees, K. Rodrguez-Vzquez, System identification strategies applied to aircraft gas turbine engines, Annual Reviews in Control 24 (2000) 67 – 81.

[37] C. Evans, P. Fleming, D. Hill, J. Norton, I. Pratt, D. Rees, K. Rodrguez-Vzquez, Application of system identification techniques to aircraft gas turbine engines, Control Engineering Practice 9 (2) (2001) 135 – 148.

[38] C. M. Holcomb, R. A. de Callafon, R. R. Bitmead, Closed-loop identification of hammerstein systems with application to gas turbines, in: World Congress, Vol. 19, 2014, pp. 493–498.

[39] N. Sugiyama, System identification of jet engines, in: ASME 1998 International Gas Turbine and Aeroengine Congress and Exhibition, American Society of Mechanical Engineers, 1998, pp. V005T15A007–V005T15A007.

[40] G. G. Kulikov, H. A. Thompson, Dynamic Modelling of Gas Turbines: Identification, Simulation, Condition Monitoring and Optimal Control, Springer, 2004.

[41] H. Hjalmarsson, M. Gevers, F. de Bruyne, For model-based control design, closed-loop identification gives better performance, Automatica 32 (12) (1996) 1659 – 1673.

[42] U. Forssell, L. Ljung, Identification of unstable systems using output error and box-jenkins model structures, IEEE Transactions on Automatic Control 45 (1) (2000) 137–141.

[43] U. Forssell, L. Ljung, Closed-loop identification revisited, Automatica 35 (7) (1999) 1215 – 1241.

[44] P. M. V. D. Hof, R. J. Schrama, An indirect method for transfer function estimation from closed loop data, Automatica 29 (6) (1993) 1523 – 1527.

[45] U. Forssell, L. Ljung, A projection method for closed-loop identification, IEEE Transactions on Automatic Control 45 (11) (2000) 2101–2106.

[46] C. Soares, Gas turbines: a handbook of air, land and sea applications, Butterworth-Heinemann, 2011.

[47] H. I. H. Saravanamuttoo, G. F. C. Rogers, H. Cohen, Gas turbine theory, Pearson Education, 2001.

[48] P. V. Overschee, B. D. Moor, N4sid: Subspace algorithms for the identification of combined deterministic-stochastic systems, Automatica 30 (1) (1994) 75 – 93.

[49] M. Jansson, Subspace identification and arx modeling, in: Proc. 13th IFAC Symp. on System Identification. Rotterdam, The Netherlands, 2003.

[50] T. Kobayashi, D. L. Simon, Evaluation of an enhanced bank of kalman filters for in-flight aircraft engine sensor fault diagnostics, in: ASME Turbo Expo 2004: Power for Land, Sea, and Air, American Society of Mechanical Engineers, 2004, pp. 635–645.

[51] S. Borguet, O. Léonard, A sensor-fault-tolerant diagnosis tool based on a quadratic programming approach, Journal of Engineering for Gas Turbines and Power 130 (2) (2008) 021605.

[52] E. Larsson, J. Åslund, E. Frisk, L. Eriksson, Gas turbine modeling for diagnosis and control, Journal of Engineering for Gas Turbines and Power 136 (7) (2014) 071601.

[53] T. Kobayashi, D. L. Simon, J. S. Litt, Application of a constant gain extended kalman filter for in-flight estimation of aircraft engine performance parameters, in: ASME Turbo Expo 2005: Power for Land, Sea, and Air, American Society of Mechanical Engineers, 2005, pp. 617–628.